UNIVERSITY OF MICHIGAN
OCT 27 1953
ENGINEERING LIBRARY

# JOURNAL OF THE AERONAUTICAL SCIENCES

VOLUME 20 OCTOBER, 1953 NUMBER 10

## CONTENTS

**Turbulence in Supersonic Flow**.....LESLIE S. G. KOVÁSZNAY 657

**The Effect of Boundary Layer on Sonic Flow Through an Abrupt Cross-Sectional Area Change**.....ROBERT S. WICK 675

**Subsonic Compressibility Corrections for Propellers and Helicopter Rotors**.....E. V. LAITONE AND LAWRENCE TALBOT 683

**A Steady-Flow Aeroelastic Study by Electrical Analogy**.....ROBERT H. SCANLAN 691

**The Second-Order Lifting Pressure and Damping in Roll of Sweptback Rolling Airfoils at Supersonic Speeds**.....JOHN C. MARTIN AND NATHAN GERBER 699

**A Method of Estimating the Compressive Strength of Optimum Sheet-Stiffener Panels for Arbitrary Material Properties, Skin Thickness, and Stiffener Shapes**.....W. R. MICKS 705

**Readers' Forum**: "On Similarity of Thermal Stresses in Elastic Bodies," by Martin Lessen; "Discrete Vortex Systems in the Transition Range of Fully Developed Flow in a Pipe," by J. R. Weske and A. H. Plantholt; "Variation of Transition Reynolds Number with Mach Number," by A. H. Lange, L. P. Gieseler, and R. E. Lee; "Boundary Layers with Variable Heat Capacity on Non-isothermal Surfaces," by Martin Bloom; "Concluding Discussion on the Hydraulic Analogy," by E. V. Laitone; "Open-Nose Body of Revolution of Minimum Drag at Small Supersonic Speeds," by Elliot T. Benedikt; "An Expression for the Gust Alleviation Factor," by M. L. Williams; "On an Integral Equation in the Supersonic Oscillating Wing Theory," by T. Y. Li and H. J. Stewart; "Application of the Compensation Theorem to the Modification of Redundant Structures," by R. H. MacNeal; "Generalization of the Energy Equation Solution for Some Rotationally Symmetrical Laminar Flows," by Dragutin Stojanović; "A Method for Stabilizing the Longer Period Oscillation of a Model Flying in a Closed Wind Tunnel with Freedoms in Pitch and Heave," by Eugene Larrabee.....716–728

*Published by the*
INSTITUTE OF THE AERONAUTICAL SCIENCES, INC.

# JOURNAL OF THE AERONAUTICAL SCIENCES

*Editor:* HUGH L. DRYDEN, *Director, NACA*

*Associate Editor:* ROBERT R. DEXTER *Managing Editor:* BERNEICE H. JARCK

## Editorial Committee

**Aerodynamics**

Francis Clauser
Howard Emmons
Antonio Ferri
Alexander Flax
R. Paul Harrington
R. T. Jones
Carl Kaplan
H. W. Liepmann
C. C. Lin
H. F. Ludloff
Harold Luskin
John R. Markham
Clark B. Millikan
Shatswell Ober
W. Bailey Oswald
Allen E. Puckett
Elliott G. Reid
H. J. E. Reid
Russell Robinson
G. B. Schubauer
W. R. Sears
John Stack
Theodore von Kármán

**Air Transport**

Charles Froesch
J. A. Herlihy
R. D. Kelly
Otto B. Kirchner
Jerome Lederer
John C. Leslie
R. Dixon Speas

**Flight Testing**

W. K. Ebel
R. R. Gilruth
Melvin N. Gough
E. G. Stout

**Structures and Materials**

W. B. Bleakney
E. W. Conlon
L. H. Donnell
E. C. Hartmann
N. J. Hoff
Samuel Levy
E. E. Lundquist
Alfred S. Niles
W. Ramberg
F. R. Shanley
H. W. Sibert
C. R. Strang
S. Timoshenko
H. S. Tsien
Chi-Teh Wang

**Rotating Wing Aircraft**

F. B. Gustafson
K. H. Hohenemser
Bartram Kelley
R. B. Maloy
Ralph McClarren
R. H. Miller
R. H. Prewitt
Igor I. Sikorsky

**Vibration and Flutter**

Lee Arnold
M. A. Biot
R. L. Bisplinghoff
William Bollay
Chieh-Chien Chang
I. E. Garrick
Martin Goland
J. P. Den Hartog

**Aircraft Design**

W. E. Beall
W. K. Ebel
Hall L. Hibbard
Richard Hutton
C. L. Johnson
A. A. Kartveli
C. J. McCarthy
Fred E. Weick
Robert J. Woods

**Electronics in Aviation**

K. C. Black
E. F. Herzog
David S. Little
D. K. Martin
George Rappaport
Paul Rosenberg
L. M. Sherer

**Physiologic Problems**

H. G. Armstrong
Louis H. Bauer
Robert J. Benford
Eugene Du Bois
W. Randolph Lovelace, II
Ross A. MacFarland

**Fuels and Oils**

D. P. Barnard
J. H. Doolittle
Graham Edgar
R. T. Goodwin
S. D. Heron
A. M. Rothrock

**Flight Propulsion**

George W. Brady
Frank W. Caldwell
L. S. Hobbs
E. E. Johnson
Joseph Keenan
R. P. Kroon
Hans Reissner
Abe Silverstein
C. Fayette Taylor
E. S. Taylor
P. Taylor
E. S. Thompson
H. S. Tsien

**Instruments**

Allan G. Binnie
J. R. Bradburn
Charles H. Colvin
C. S. Draper
S. G. Eskin
O. E. Esval
H. W. Holzapfel
W. L. Howland
George H. Purcell
C. F. Savage
O. Hugo Schuck
C. L. Seward, Jr.
L. D. Statham
R. C. Sylvander
D. K. Warner

**Meteorology**

C. F. Brooks
D. M. Little
E. J. Minser
F. W. Reichelderfer
H. C. Willett

## SUBSCRIPTION RATES

JOURNAL OF THE AERONAUTICAL SCIENCES, Published Monthly.—United States and Possessions: 1 Year, $12.00; Single Copies, $1.50. Foreign Countries Including Canada (American Currency Rates): 1 Year, $13.00; Single Copies, $1.50.

AERONAUTICAL ENGINEERING REVIEW, Published Monthly.—United States and Possessions: 1 Year, $3.00; Single Copies, $0.50. Foreign Countries Including Canada (American Currency Rates): 1 Year, $3.50; Single Copies, $0.50.

Notices of change of address should be sent to the Institute at least 30 days prior to actual change of address.

Manuscripts for publication, proofs, and all correspondence should be addressed to the Editorial Office of the JOURNAL.

Correspondence regarding subscriptions may be addressed to Publication Office, 20th and Northampton Sts., Easton, Pa., or to the Editorial Office of the JOURNAL OF THE AERONAUTICAL SCIENCES, 2 East 64th Street, New York 21, New York.

*Copyright, 1953, by the Institute of the Aeronautical Sciences, Inc.*

Entered as Second Class Matter at the Post Office, Easton, Pa., May 1, 1937. Acceptance for mailing at a special rate of Postage provided for in the Act of August 24, 1912. Authorized April 29, 1937.

JOURNAL OF THE AERONAUTICAL SCIENCES

VOLUME 20 OCTOBER, 1953 NUMBER 10

# Turbulence in Supersonic Flow*

LESLIE S. G. KOVÁSZNAY†

*The Johns Hopkins University*

SUMMARY

First-order perturbation theory indicates that the Navier-Stokes equations for a compressible, viscous, and heat-conductive gas can have three distinctly different types of disturbance fields, obeying three independent differential equations. These three "modes" of disturbance fields are: vorticity mode, entropy mode, and sound-wave mode. The modes are independent when the intensities of the fluctuations are small, but they interact at larger intensities when linearization is not permissible.

The principal tool for measuring the fluctuating fields is the hot-wire anemometer adapted for supersonic flow. In a supersonic flow the hot-wire anemometer responds to two variables: mass flow fluctuations and stagnation temperature fluctuations. Each of the above three modes contributes to both of these variables. By taking fluctuation measurements at different wire temperatures, the relative sensitivity to the flow parameters varies and a "fluctuation diagram" can be obtained. The character of the fluctuation diagram differs for each mode, and even coexisting modes can be separately determined by analyzing the fluctuation diagram under certain restrictive conditions.

Hot-wire measurements were obtained in various supersonic flows. Pure temperature spottiness (entropy mode) and pure sound-wave fields were explored. Detailed measurements were taken in a turbulent supersonic boundary layer. With the aid of the fluctuation diagram, the intensity of temperature spottiness (entropy mode) and of turbulent velocity fluctuations (vorticity mode) was measured across the layer. Energy spectrum and probability density measurements gave clues concerning the character of the fluctuations.

## INTRODUCTION

THE PROBLEM OF TURBULENCE in a compressible medium brings up a number of specific questions. Will the turbulence be essentially similar to that in the incompressible case with only slight compressibility correction or will there be some entirely new phenomena? What kind of measurements of the fluctuations can be performed? What experimental methods can be used? How will the measurements be interpreted? What quantity will take the role of the "turbulence level" in the high-speed case?

One can venture an intuitive guess that random fluctuations of more than one kind will be present in the compressible case. Sound waves are likely to accompany the vorticity fluctuations, and we may expect that the fluid particles, having passed through different shear regions, may have suffered different amounts of entropy changes. When the pressure becomes uniform, they may exhibit entropy spottiness appearing as temperature spottiness to the fixed observer. In the first part of the paper it will be proved that the three "modes" are the solutions for the perturbation fields superimposed on a uniform steady flow of a compressible, viscous, and heat-conductive gas. Since all three modes represent fluctuations both in momentum and energy when superimposed on a uniform supersonic flow, the dynamic effects (e.g., the transition of a laminar boundary layer) are nonnegligible for the three modes.

The extension of the hot-wire technique to supersonic velocities has been reported earlier.[9] The principal objective of the present investigation is to find the proper method of disentangling the contributions to the hot-wire signal from the three different modes. If this effort is successful, the determination of the intensity and correlation of coexisting modes becomes possible.

One of the most intriguing practical questions of supersonic turbulence measurements is the determination of the fluctuation level in the free stream of a good supersonic wind tunnel and the exploration of the relation of this level to the flow conditions upstream of the

Presented at the Aerodynamics Session, Twenty-First Annual Meeting, IAS, New York, January 26–29, 1953.

* The author is much indebted to Drs. Francis H. Clauser and Mark V. Morkovin for their stimulation, vigorous interest, and helpful criticism; to Dr. F. R. Hama for the construction and operation of the high-frequency spectral analyzer; and to Miss Patricia C. Clarken for her active and efficient participation in all phases of the work.

† Professor of Aeronautics, Department of Aeronautics.

nozzle. However, we have not chosen to investigate this case first because extremely low-level signals are involved which bring us dangerously close to the noise level of the electronic equipment. Intense fluctuations can be measured much more conveniently, and the character of "compressible turbulence" can be more readily observed and understood.

Following this reasoning, the first detailed measurements were obtained in a reasonably thick supersonic turbulent boundary layer. The scale of turbulence in this case was not prohibitively small and the intensity of fluctuations was sufficiently large to permit analysis of the signals and separation of contributions from the different modes.

The present work is an integral part of our long-range program of turbulence investigation at supersonic velocities pursued for a number of years at Hopkins. During these years the financial support of two sponsors made the investigations possible: U.S. Navy under contract NOrd-8036 and Squid Project under contract N6ori-105-Task Order III. Some of the experiments were conducted outside of our laboratory. The facilities of the Ballistic Research Laboratories, Aberdeen Proving Ground, were made available. The author also conducted some experiments at Ames Aeronautical Laboratory, NACA, and some of the results are reported here. The hot-wire equipment used in most of the tests was developed as a cooperative project of the National Bureau of Standards and The Johns Hopkins University.

### Symbols

| | |
|---|---|
| $\boldsymbol{\xi}$ | = position vector in coordinate system $\xi_1, \xi_2, \xi_3$ |
| $\xi_1, \xi_2, \xi_3$ | = Cartesian coordinates moving with the average velocity of the fluid (components of $\boldsymbol{\xi}$) |
| $x, y, z$ | = Cartesian coordinates fixed with respect to the wind tunnel |
| $t$ | = time |
| $\rho$ | = density |
| $\boldsymbol{v}$ | = velocity vector in coordinate system $\xi_1, \xi_2, \xi_3$ |
| $v_1, v_2, v_3$ | = velocity components of $\boldsymbol{v}$ |
| $p$ | = pressure |
| $\mu$ | = dynamic viscosity |
| $T$ | = absolute temperature |
| $C_p$ | = specific heat at constant pressure |
| $\kappa$ | = heat conductivity |
| $\Phi$ | = rate of dissipation |
| $\gamma$ | = ratio of specific heats |
| $\nabla^2$ | = Laplace operator |
| $G$ | = space-time domain |
| $V$ | = volume |
| $t_A, t_B$ | = beginning and end of time interval |
| $\overline{\quad}$ | = bar indicating average value |
| $\Delta$ | = fluctuation |
| $P$ | = nondimensional pressure fluctuation |
| $s$ | = nondimensional entropy fluctuation |
| $\Delta E$ | = entropy change |
| $\nu = \mu/\bar{\rho}$ | = kinematic viscosity (average value) |
| $a = \sqrt{\gamma(\bar{p}/\rho)}$ | = speed of sound (average value) |
| $q = \operatorname{div} \boldsymbol{v}$ | = source strength of the velocity field |
| $\boldsymbol{\omega} = \operatorname{curl} \boldsymbol{v}$ | = vorticity |
| $\tau$ | = relaxation time of medium |
| $\varphi$ | = velocity potential |
| $l_0$ | = characteristic length of the viscous compressible medium |
| $t_0$ | = characteristic time of the medium |
| $\lambda$ | = wave length |
| $L$ | = characteristic length of domain $G$ |
| $k$ | = wave number |
| $\omega_0$ | = vorticity amplitude |
| $\boldsymbol{n}$ | = normal vector |
| $t_1$ | = decay time of vorticity mode |
| $d_1$ | = decay distance of vorticity mode |
| $P_0$ | = pressure disturbance amplitude |
| $C$ | = complex propagation velocity |
| $t_2$ | = decay time of sound waves |
| $d_2$ | = decay distance of sound waves |
| $s_0$ | = entropy disturbance amplitude |
| $t_3$ | = decay time for entropy waves |
| $d_3$ | = decay distance for entropy waves |
| $\Delta e(t)$ | = voltage fluctuation across hot wire (signal compensated for thermal lag) |
| $m(t)$ | = mass flow fluctuation |
| $\vartheta(t)$ | = stagnation temperature fluctuation |
| $T_0$ | = stagnation temperature |
| $\Delta U(t)$, $\Delta V(t)$, $\Delta W(t)$ | = velocity fluctuation observed by fixed probe in $x, y, z$ coordinate system |
| $M$ | = Mach Number |
| $\alpha(M), \beta(M)$ | = function of the Mach Number |
| $\Delta e_T$ | = hot-wire sensitivity to stagnation temperature fluctuation |
| $\Delta e_M$ | = hot-wire sensitivity to mass flow fluctuation |
| $r = \Delta e_M/\Delta e_T$ | = sensitivity ratio |
| $'$ | = (prime), root mean square (r.m.s.) value of a fluctuating quantity |
| $\vartheta_* = \Delta e'/\Delta e_T$ | = virtual r.m.s. stagnation temperature fluctuation |
| $R_e$ | = hot-wire resistance at equilibrium temperature $T_e$ |
| $R_W$ | = hot-wire resistance when operated at temperature $T_W$ |
| $a_W' = \dfrac{R_W - R_e}{R_e}$ | = overheating ratio |
| $R_{MT} = \dfrac{\overline{m\vartheta}}{m'\vartheta'}$ | = mass flow stagnation temperature correlation coefficient |
| $u = 100\left(\dfrac{\Delta U_t}{\bar{U}}\right)$ | = solenoidal velocity fluctuation (per cent) |
| $\Theta = 100\left(\dfrac{\Delta T_S}{T_0}\right)$ | = temperature spottiness (entropy mode) in per cent of total temperature |
| $\Delta U_t$ | = solenoidal velocity fluctuation |
| $\Delta T_S$ | $= \Delta T - \dfrac{\bar{T}}{\bar{p}} \dfrac{\gamma - 1}{\gamma} \Delta p$ = temperature spottiness |
| $P_0(\eta)$ | = plane wave pressure distribution |
| $f$ | = frequency |
| $\sigma$ | = mass flow fluctuation of sound waves that are almost Mach waves (per cent) |
| $L_x$ | = integral scale of turbulence (longitudinal) |
| $u_1, u_2$ $\sigma_1, \sigma_2, \sigma_3$ | = components of fluctuations |

## (I) Three Modes of Fluctuations

### *Governing Equations*

A simple analysis demonstrates that a viscous compressible heat-conducting medium can have three dif-

ferent kinds of small perturbation fields obeying three independent differential equations.

The following assumptions will be used: (A) The medium is a perfect gas with constant specific heats, viscosity, and heat conduction; and (B) the Prandtl Number of the gas is equal to $^3/_4$. The governing equations of such a fluid contain four independent variables $\xi_1$, $\xi_2$, $\xi_3$, $t$ and six dependent variables $p$, $\rho$, $T$, $v_1$, $v_2$, $v_3$. There are six equations: three equations (or a single vector equation) for the conservation of momentum, one equation for the conservation of energy, one for the conservation of mass, and one is the equation of state for the medium.

*Momentum:*

$$\rho \frac{\partial \boldsymbol{v}}{\partial t} = -\operatorname{grad} p - \frac{\rho}{2} \operatorname{grad} \boldsymbol{v}^2 + \rho\,(\boldsymbol{v} \times \operatorname{curl} \boldsymbol{v}) + \mu(\nabla^2 \boldsymbol{v} + {}^1/_3 \operatorname{grad} \operatorname{div} \boldsymbol{v}) \quad (1)$$

*Energy:*

$$\rho C_p \frac{\partial T}{\partial t} = \kappa \nabla^2 T + \frac{\partial p}{\partial t} + \boldsymbol{v} \cdot \operatorname{grad} p - \rho C_p \boldsymbol{v} \cdot \operatorname{grad} T + \Phi \quad (2)$$

*Mass:*

$$(\partial \rho / \partial t) + \operatorname{div} (\rho \boldsymbol{v}) = 0 \quad (3)$$

*State:*

$$p/\rho = [(\gamma - 1)/\gamma] C_p T \quad (4)$$

where $\nabla^2$ is the Laplace operator,

$$\nabla^2 = \frac{\partial^2}{\partial \xi_1^2} + \frac{\partial^2}{\partial \xi_2^2} + \frac{\partial^2}{\partial \xi_3^2}$$

and $\Phi$ is the viscous dissipation,

$$\Phi = \mu[(\operatorname{curl} \boldsymbol{v})^2 + \nabla^2(\boldsymbol{v}^2) - {}^2/_3(\operatorname{div} \boldsymbol{v})^2 - 2 \operatorname{div} (\boldsymbol{v} \times \operatorname{curl} \boldsymbol{v}) - 2\, \boldsymbol{v} \operatorname{grad} \operatorname{div} \boldsymbol{v}]$$

The above set of partial differential equations are nonlinear, and a simple inspection does not reveal any clues about different "modes" of the fluctuation fields.

### *Small Perturbation*

In the present analysis interest is focused on the small fluctuations in a flow field. Linearization of the above set of equations may yield an interesting limiting case. However, a similar analysis was carried out in reference 1 without heat-conduction effects.

The following new assumptions will be introduced, in addition to (A) and (B): (C) The flow is described within a space time domain $G$ consisting of a volume $V$ in space and a time interval $t_A - t_B$. (D) The coordinate system is chosen in such a way that the average velocity in $G$ is zero. (E) The fluctuations in pressure, density, and absolute temperature are small compared with their respective average values in $G$. (F) The velocities are small compared with the average speed of sound in $G$. (G) There are no solid boundaries within $G$ or at its boundaries.

The physical picture corresponding to the above assumptions is a compressible flow field in a finite domain of space observed for a finite time interval viewed by an observer moving with the average velocity. For the sake of small perturbation theory, it is assumed that the departures from free-stream conditions are small. A typical case to which such a treatment may apply is the fluctuation field in a supersonic wind tunnel. The flow is observed for a length of time that is less than the time of passage of a fluid particle through the test section.

A trivial solution of the set of equations [Eqs. (1), (2), (3), (4)] is

$$\boldsymbol{v} \equiv 0, \qquad p = \text{const.}, \qquad T = \text{const.}$$
$$\rho = \gamma p/(\gamma - 1) C_p T = \text{const.}$$

This "flow field" is a gas at rest in the above-defined coordinate system. From the conventional coordinate system $x$, $y$, $z$, $t$, it also can represent a uniform parallel flow in a supersonic wind tunnel.

We now assume small perturbations. Let us introduce mean values and fluctuations,

$$T = \bar{T} + \Delta T, \quad p = \bar{p} + \Delta p, \quad \rho = \bar{\rho} + \Delta \rho$$

where

$$\bar{T} = \frac{1}{|G|} \int\int_G \int\int T(\xi_1, \xi_2, \xi_3, t)\, d\xi_1\, d\xi_2\, d\xi_3\, dt \quad (5)$$

By definition

$$\overline{\Delta p} = \overline{\Delta \rho} = \overline{\Delta T} = 0$$

The velocity fluctuation is the velocity itself by virtue of the special choice of coordinate system.

Now it is convenient to define nondimensional temperature, pressure, and density fluctuations

$$P = \Delta p/\gamma \bar{p} = \Delta p/\rho a^2 \quad (6)$$

$$s = (\Delta T/\bar{T}) - (\gamma - 1)P \quad (7)$$

where $s$ represents the "nonisentropic temperature fluctuation" and is really the nondimensional entropy fluctuation.

Since the equation of state expressed with the entropy change $\Delta E$ is

$$T_2/T_1 = (p_2/p_1)^{(\gamma - 1)/\gamma} e^{\Delta E/C_p}$$

linearization gives

$$\Delta T/\bar{T} = (\gamma - 1)P + (\Delta E/C_p)$$

or

$$s = \Delta E/C_p \quad (8)$$

The nondimensional density fluctuations become

$$\frac{\Delta \rho}{\bar{\rho}} = \frac{\Delta p}{\bar{p}} - \frac{\Delta T}{\bar{T}} = P - s \quad (9)$$

Using the new variables the equations of motion can be

rewritten. Dropping the higher order terms we obtain a set of linear equations.

*Momentum:*

$$\frac{\partial \boldsymbol{v}}{\partial t} = -a^2 \operatorname{grad} P + \nu(\nabla^2 \boldsymbol{v} + {}^1/_3 \operatorname{grad} \operatorname{div} \boldsymbol{v}) \quad (10)$$

*Energy:*

$$\frac{\partial s}{\partial t} - \frac{4\nu}{3}\nabla^2 s = \frac{4(\gamma - 1)\nu}{3}\nabla^2 P \quad (11)$$

*Mass:*

$$\operatorname{div} \boldsymbol{v} = -(\partial P/\partial t) + (\partial s/\partial t) \quad (12)$$

The linearized equation of state has been used to eliminate the density fluctuations.

Having a set of linear equations, superposition holds; therefore, we are seeking different types of solutions to satisfy the above set of equations. We can obtain two different forms of the equation for the conservation of momentum involving the divergence and the curl of the velocity field,

$$\operatorname{div} \boldsymbol{v} = q \quad (13)$$
$$\operatorname{curl} \boldsymbol{v} = \boldsymbol{\omega} \quad (14)$$

Taking the curl and the divergence of Eq. (10), we find

$$(\partial \boldsymbol{\omega}/\partial t) - \nu\nabla^2 \boldsymbol{\omega} = 0 \quad (15)$$
$$(\partial q/\partial t) - (4\nu/3)\nabla^2 q = -a^2 \nabla^2 P \quad (16)$$

The vorticity field obeys a separate equation not involving the other dependent variables, indicating that the vorticity field has no first-order interaction with the pressure and entropy (temperature) fields.

Now we can show that the pressure also obeys a separate equation. From Eq. (12) we can express the divergence of the velocity field,

$$q = -(\partial P/\partial t) + (\partial s/\partial t) \quad (17)$$

Substituting $q$ in Eq. (16) and substituting the terms involving $s$ from Eq. (11), we find

$$\frac{1}{a^2}\frac{\partial^2 P}{\partial t^2} - \nabla^2 P - \frac{4\gamma\nu}{3a^2}\frac{\partial \nabla^2 P}{\partial t} = 0 \quad (18)$$

The pressure obeys this equation, which is almost the wave equation. The extra term accounts for sound absorption at high frequencies. A pressure field that obeys the above equation will be called, in general, a sound wave.

If we compare Eqs. (11) and (16), we find that both equations are of the heat equation type and that a quantity proportional to the Laplacean of the pressure acts as "heat source."

The general solution of both Eqs. (11) and (16) consists of two parts, one part depending on the pressure and another being the solution of the "homogeneous" equations,

$$(\partial q/\partial t) - (4\nu/3)\nabla^2 q = 0 \quad (19)$$
$$(\partial s/\partial t) - (4\nu/3)\nabla^2 s = 0 \quad (20)$$

The general solution of Eqs. (19) and (20) is not independent, since it must obey the conservation of mass, Eq. (12). The pressure-dependent solutions of Eqs. (11) and (16) can be found in the following way: We can express $\nabla^2 P$ from Eq. (18), which can be written as

$$\left(1 + \tau\frac{\partial}{\partial t}\right)\nabla^2 P = \frac{1}{a^2}\frac{\partial}{\partial t}\left(\frac{\partial}{\partial t} - \frac{4\nu}{3}\nabla^2\right)P \quad (21)$$

where

$$\tau = 4(\gamma - 1)\nu/3a^2$$

$\tau$ can be regarded as the relaxation time of the medium. Substituting Eq. (21) into Eqs. (11) and (16), we obtain the special pressure-dependent solutions

$$[1 + \tau(\partial/\partial t)]q = -\partial P/\partial t \quad (22)$$
$$[1 + \tau(\partial/\partial t)]s = \tau(\partial P/\partial t) \quad (23)$$

These equations indicate that the source field $q$ and entropy field $s$ follow the pressure waves not exactly in phase, but with a small time lag $\tau$. This time lag is quite analogous to the thermal time lag of a hot-wire anemometer. However, the time lag $\tau$ is extremely small for all practical cases. For atmospheric air it is of the order of $10^{-10}$ sec. For many concrete examples, the operator $\tau(\partial/\partial t)$ is negligible compared to unity.

Expressing the potential flow field with a velocity potential $\varphi$ instead of $q$, we find, from Eq. (16),

$$-\left(1 + \tau\frac{\partial}{\partial t}\right)\frac{\partial \varphi}{\partial t} = a^2\left(1 + \frac{\gamma\tau}{\gamma - 1}\frac{\partial}{\partial t}\right)P \quad (24)$$

If the flow field is steady, $\partial\varphi/\partial t = 0$, and we find from Eq. (10) that $P \equiv 0$. This is a steady harmonic flow field. We shall take out this special case from the "sound waves" and add it to the "vorticity mode," since it does not contradict Eq. (15).

Another special case occurs when $\nabla^2 P \equiv 0$. Then $\partial^2 P/\partial t^2 = 0$. From Eq. (16) we find $q \equiv 0$; therefore the field is harmonic. In this case, from Eq. (10), we find that

$$P = -(1/a^2)(\partial\varphi/\partial t) \quad (25)$$

We are now ready to define the three independent "modes."

(*1*) *Vorticity Mode.*—The principal variable is the vorticity $\boldsymbol{\omega}$. The governing equation is Eq. (15). The velocity field consists of two parts: One part is induced by the vorticity found within the volume, and the other part is a steady harmonic field that is completely defined by specifying the time-averaged velocity at the boundaries,

$$\boldsymbol{v}(\boldsymbol{\xi}) = \frac{1}{4\pi}\int\int_V\int \frac{(\boldsymbol{\xi} - \boldsymbol{\xi}') \times \boldsymbol{\omega}(\boldsymbol{\xi}')dV(\boldsymbol{\xi}')}{|\boldsymbol{\xi} - \boldsymbol{\xi}'|} + \operatorname{grad} \varphi_1 \quad (26)$$

with $\partial\varphi_1/\partial t = 0$ and $\nabla^2\varphi_1 = 0$, $P = 0$, $s = 0$. The steady harmonic field fits naturally into this particular mode, since the vorticity field outside of the volume $V$ induces exactly such a harmonic field within the volume as long as the diffusion does not progress so far that the vorticity outside of the volume will propagate into the volume.

(2) *Sound-Wave Mode.*—The principal variable is pressure, and it obeys Eq. (18). The other variables are $q$ and $s$ [see Eqs. (22) and (23)]. The special case is

$$\partial P/\partial t = 0, \quad \nabla^2 P = 0, \quad q = 0$$

The flow is then harmonic, but since the case $\partial\varphi/\partial t = 0$ is taken out, the only solution is

$$\varphi = \varphi_2' t, \quad \nabla^2\varphi_2' = 0, \quad \partial\varphi_2'/\partial t = 0$$

where $\varphi_2$, the potential, varies proportional to time and $\varphi_2'$ is a harmonic function independent of time.

The small entropy variation in the normally "isentropic" sound field is caused by heat-conductive sound absorption, but it is a negligible quantity for most practical cases.

(3) *Entropy Mode.*—The compatible solutions of Eqs. (19) and (20) yield this mode. The principal variable is the entropy fluctuation $s$ obeying Eq. (20). The decay of temperature (entropy) spots by heat conduction changes the density and causes a motion. The motion is a potential flow

$$\boldsymbol{v} = (4\nu/3)\ \text{grad}\ s \tag{27}$$

or $\boldsymbol{v} = \text{grad}\ \varphi_3$, where $\varphi_3 = 4\nu as/3$. The motion associated with the decay of entropy spottiness is rather small in all practical cases.

We see from the results that two of the modes obey the heat equation, although they have different diffusion coefficients (in the ratio of 3:4), and the third mode obeys the wave equation with an extra absorption term. Since this is a linearized theory, the modes do not interact within the domain $G$. Interaction may take place, however, outside of the domain either at solid boundaries or in regions where the fluctuations are not small and therefore nonlinear interaction is not negligible. If a point is outside of the domain $G$, it may mean one of two things: Either it is outside of the volume $V$ or prior to time $t_A$ or after time $t_B$. If in its past history the fluid went through a grid, the high-intensity turbulence produced strong sound waves and the viscous dissipation produced entropy spots. The former have propagated away according to the wave equation, but the latter have traveled with the fluid, diffusing slowly by heat conduction. When our observation starts (at $t_A$), the modes are already sufficiently low in intensity so that nonlinear interaction between any two modes is negligible, although nonlinearity may have had a deciding role in the creation of these modes.

On the other hand, if these noninteracting modes pass through a region of a strong gradient, such as a shock wave, they may interact with the strong field and conversion from one mode to another may take place.[2,3]

### *Second-Order Theory*

If the different modes are not sufficiently weak to warrant linearization and, on the other hand, are not strong enough to destroy completely the above picture of modes, a theory of weak interaction can be developed, keeping only the first- and second-order terms in the dependent variables.

If the second-order terms are small compared with the first-order terms, they may be considered as "sources" in the governing equations for the modes. Formally, we obtain the following equations:

$$(\partial\boldsymbol{\omega}/\partial t) - \nu\nabla^2\boldsymbol{\omega} = \boldsymbol{\Omega}(\boldsymbol{\omega}, P, s) \tag{28}$$

$$\frac{\partial s}{\partial t} - \frac{4\nu}{3}\nabla^2 s = S(\boldsymbol{\omega}, P, s) \tag{29}$$

$$\frac{1}{a^2}\frac{\partial^2 P}{\partial t^2} - \nabla^2 P - \frac{4\gamma\nu}{3a^2}\frac{\partial\nabla^2 P}{\partial t} = \Pi(\boldsymbol{\omega}, P, s) \tag{30}$$

where $\boldsymbol{\Omega}$ is the rate of vorticity creation by the action of all three modes, $S$ is the rate of entropy spot creation by the interaction of all three modes, and $\Pi$ is the rate of sound generation by the interaction of all three modes.

Since we assumed only second-order interaction, each term breaks down into six terms, each involving only one pair of modes. For example,

$$\Pi(\boldsymbol{\omega}, P, s) = \Pi_1(\boldsymbol{\omega}, \boldsymbol{\omega}) + \Pi_2(P, P) + \Pi_3(s, s) + \Pi_{12}(\boldsymbol{\omega}, P) + \Pi_{23}(P, s) + \Pi_{31}(s, \boldsymbol{\omega})$$

where $\Pi_1$ is the source strength of sound waves generated by the vorticity field, $\Pi_2$ is the nonlinear term in sound propagation (e.g., steepening of sound waves into shock waves), $\Pi_3$ is the source strength of sound waves generated by the decay of temperature spottiness, $\Pi_{12}$ is the scattering of sound waves by the moving medium (vorticity field), $\Pi_{23}$ is the scattering of sound waves on the entropy spots (variation in speed of sound), and $\Pi_{31}$ is the source strength of sound waves generated by the vorticity field hurling around temperature spots.

Similarly, $S$ and $\boldsymbol{\Omega}$ each can be broken down into six interaction terms. The term $\boldsymbol{\Omega}_1(\boldsymbol{\omega}, \boldsymbol{\omega})$ is exactly the nonlinear term in incompressible turbulence theory accounting for the "stretching of vortices" or the "energy transfer term" in the spectral representation. There are 18 interaction terms in the second-order theory, and, depending on the specific problems, some can be more significant than others.

Already a few attempts have been reported in the literature to estimate some of these interaction terms. Lighthill[4] and later Proudman[15] treated the sound generated by the vorticity ($\Pi_1$ term), and Chandrasek-

har estimated the scattering of sound on the turbulent (vorticity mode) field.[5] Other attempts were made with a more statistical approach such as Moyal's,[6] giving an explicit procedure to find the double correlation in coexisting isotropic turbulence (vorticity mode) and isotropic random sound waves.

***Further Simplification of the Modes***

Up to this point the size of the space-time domain $G$ was completely unspecified. There are three characteristic dimensions entering into the problem. The first is the characteristic length of the medium and a related characteristic time

$$l_0 = \nu/a \tag{31}$$
$$t_0 = \nu/a^2 \tag{32}$$

These two quantities are naturally related to the mean free path of the gas; however, they are defined here on a continuum basis.

The second important length parameter is the characteristic length of the disturbances. The simplest way to visualize this is to assume sinusoidal plane wave disturbances with wave length $\lambda$.

The third length is the dimension of the domain $G$. This can be denoted by $L$.

The characteristic time interval can be defined as the characteristic length divided by the speed of sound.

If the time interval of observation is short and, in the case of sound waves, the extent of the domain in space is correspondingly small and at the same time the characteristic length of the disturbance pattern $\lambda$ is large compared with the characteristic length of the medium $l_0$, we find that the diffusion terms become negligible and we obtain, for the three modes: vorticity mode,

$$\partial\omega/\partial t = 0 \tag{33}$$

sound-wave mode,

$$(1/a^2)(\partial^2 P/\partial t^2) - \nabla^2 P = 0 \tag{34}$$

entropy mode,

$$\partial s/\partial t = 0 \tag{35}$$

Eqs. (33), (34), and (35) simply state that the vorticity and entropy are "frozen patterns" and that the sound waves obey the pure wave equation.

Regarding the turbulence pattern as a "frozen pattern" is not a new concept. It is a standard assumption for evaluation of hot-wire turbulence measurements in a low-speed wind tunnel. It is usually referred to as "Taylor's hypothesis." For the low-speed (incompressible) case, it was treated by Lin.[7] If the turbulence level is low, it is simply assumed that the pattern does not change much during its passage in the neighborhood of the hot-wire probe; therefore, a hot-wire record in time at a fixed location $x$ can be regarded in first approximation as a space record (along the $\xi_1$ axis) of the turbulence pattern at an instant.

The present result also indicates that Taylor's hypothesis may be applicable for two modes (vorticity and entropy) and that unattenuated wave propagation must be considered for the sound waves.

A simple numerical example will indicate the orders of magnitude involved in this last simplification. Periodic patterns in space are possible solutions for all three modes: longitudinal waves for the sound-wave mode, transversal waves for the vorticity mode, and scalar waves for the entropy mode. Without the simplifications expressed by Eqs. (33), (34), and (35) the waves decay in time at different rates for the different modes according to Eqs. (15), (18), and (20).

For the numerical example we shall assume conditions prevailing in the supersonic wind tunnel that has been used for most of our experiments. Stagnation conditions were near atmospheric; $\bar{p}_0 = 80$ cm. Hg; $\bar{T}_0 = 300°$K.; Mach Number $= 1.75$. Speed of sound in working section $a = 28{,}500$ cm. per sec.; kinematic viscosity $\nu = 0.5$ cm.$^2$ per sec.; the mean velocity with respect to the wind tunnel $\bar{U} = 49{,}800$ cm. per sec.

We take a periodic plane wave pattern with a wave length $\lambda = 0.1$ cm. or wave number $k = 63$ cm.$^{-1}$.

(*1*) *Vorticity Mode.*—Transversal waves with exponential decay

$$\boldsymbol{\omega} = \boldsymbol{\omega}_0 e^{ik(\boldsymbol{n}\cdot\vec{\xi}) - (t/t_1)} \tag{36}$$
$$(\boldsymbol{\omega}_0 \cdot \boldsymbol{n}) = 0 \quad \text{since div } \boldsymbol{\omega} = 0$$
$$\boldsymbol{n}^2 = 1$$

Substituting into Eq. (15), we obtain the decay time

$$t_1 = 1/\nu k^2 \tag{37}$$

For our example, $t_1 = 5.0 \times 10^{-4}$ sec. The vorticity pattern will travel in the wind tunnel during the decay time a distance $d_1 = \bar{U}t_1 = 25.2$ cm.

(*2*) *Sound Waves.*—Longitudinal waves propagating with a velocity and exponentially decaying in time

$$P = P_0 e^{ik(\boldsymbol{n}\cdot\vec{\xi} - Ct)} \tag{38}$$

The real part of $C$ is $C_1$ and gives the actual propagating velocity. The imaginary part gives the decay time. Substituting into Eq. (18) we obtain

$$C = a\sqrt{1 - \left(\frac{2k\gamma\nu}{3a}\right)^2} - i\left(\frac{2k\gamma\nu}{3}\right) = C_1 - \frac{i}{t_2 k} \tag{39}$$

Since in all practical cases the quantity $2k\gamma\nu/3a$ is small compared with unity, the propagation velocity differs little from the nominal speed of sound $a$. The exponential decay is characterized by the decay time

$$t_2 = 3/\gamma k^2 \nu \tag{40}$$

For our example, $t_2 = 5.3 \times 10^{-4}$ sec. The wave travels with the speed of sound during this time a distance $d_2 = at_2$. For our example, $d_2 = 15$ cm. This

distance is about 150 wave lengths. The relaxation time $\tau$ is

$$\tau = 4(\gamma - 1)\nu/3a^2$$

For our example, $\tau = 3.3 \times 10^{-10}$ sec. The phase lag of the velocity field behind the pressure field is less than $^1/_{30}$ of 1 deg. The smallness of $\tau$ also indicates that the entropy fluctuations caused by the decay of sound waves [Eq. (23)] are negligible compared to the isentropic fluctuation of temperature.

*(3) Entropy Mode.*—A periodic pattern with exponential decay in time is a possible solution

$$s = s_0 e^{ik(\mathbf{n}\cdot\vec{\xi}) - (t/t_3)} \tag{41}$$

Substituting into Eq. (20) gives the decay time

$$t_3 = 3/4\nu k^2 \tag{42}$$

For our example, $t_3 = 3.8 \times 10^{-4}$ sec. The flow pattern would travel a distance $d_3$ in the wind tunnel, $d_3 = \bar{U}t_3$. For our example, $d_3 \cong 18.8$ cm. The velocity field induced by the decay of the entropy pattern is periodic (longitudinal waves). The maximum velocity from Eq. (27) is

$$|\boldsymbol{v}|_{max.} = (4\nu k/3)s_0 \tag{43}$$

For our example,

$$|\boldsymbol{v}|_{max.}/a = 1.48 \times 10^{-3} s_0$$

This estimate indicates that the potential flow, induced by the entropy mode, is rather small.

The numerical examples indicate that the viscous decay of the vorticity fields and the entropy field and the viscous attenuation of the sound field may be legitimately neglected if the wave lengths involved are not smaller than 0.1 cm. and if the extent of the domain considered is not larger than a few centimeters. Naturally there is no logical obstacle to reduce the size of the domain to the scale of the minimum size disturbance involved, and in this manner the argument for extreme simplification is strengthened.

The analysis was carried out in a coordinate system moving with the mean flow. Our measuring instruments, however, are fixed with respect to the wind tunnel. We must later reinterpret these findings from the coordinate system of the measuring probe.

## (II) Detection of the Fluctuation Modes by the Hot-Wire Anemometer

### *The Response of the Hot-Wire Anemometer*

The random fluctuations occurring in a supersonic wind tunnel can be conveniently detected and measured by the hot-wire anemometer. The principal advantage of the hot wire is not its inherently fast response but much more the fact that its response can be greatly improved by electronic methods.[9,11,12]

Naturally the hot-wire probe is fixed with respect to the tunnel walls and gives a signal proportional to fluctuations of flow variables at a point fixed in the wind-tunnel coordinate system $(x, y, z)$. On the other hand, the fluctuation modes introduced in the previous section were defined in a coordinate system moving with the average velocity $(\xi_1, \xi_2, \xi_3)$; therefore interpretation of measurements must take into account this difference.

The response of a hot wire placed normal to a supersonic air stream has been treated in some detail in references 8–12. The principal findings are the following:

(A) The unheated wire assumes an equilibrium temperature $T_e$ that is rather close to the stagnation or total temperature $T_0$.

(B) For moderate amounts of heating the heat loss of the wire is proportional to the temperature difference $T_W - T_e$. It is also a linear function of the square root of the mass flow and is independent of the Mach Number as long as the flow is supersonic.

(C) The hot wire heated by a constant electric current responds to a linear combination of mass flow fluctuations and stagnation temperature fluctuations.

(D) The thermal lag of the hot wire placed in a supersonic air stream does not essentially differ from the thermal lag observed at low speed, and the same type of electronic compensation can be used for both.

The voltage fluctuations $\Delta e(t)$ developed across the hot-wire probe (assuming proper thermal lag compensation in the amplifier) can be expressed as a function of the two flow parameters: mass flow fluctuations $m(t)$ and stagnation temperature fluctuations $\vartheta(t)$.

$$m = 100\,\frac{\Delta(\rho U)}{\bar{\rho}\bar{U}} = 100\,\frac{\Delta\rho}{\bar{\rho}} + 100\,\frac{\Delta U}{\bar{U}} \tag{44}$$

$$\vartheta = \Delta T_0/\bar{T}_0 \tag{45}$$

Since

$$T_0 = T + (\bar{U}^2/2C_p) \tag{46}$$

$$\vartheta = \alpha(\Delta T/\bar{T}) + \beta(\Delta U/\bar{U}) \tag{47}$$

where

$$\alpha = 1/\{1 + [(\gamma - 1)/2]M^2\} \tag{48}$$

$$\beta = \alpha(\gamma - 1)M^2 \tag{49}$$

The hot wire unfortunately does not respond directly to any one of the fluctuation modes derived in the first section but to two quantities that have no direct interpretation. From Eqs. (44) and (47) we see that the response has contributions from density fluctuations, velocity fluctuations (component in the direction of the main flow), and temperature fluctuations. The sensitivity to pressure does not enter directly.

The output of the hot-wire anemometer is a function of time

$$\Delta e(t) = \Delta e_T \vartheta(t) - \Delta e_M m(t) \tag{50}$$

where the sensitivity constants $\Delta e_M$, $\Delta e_T$ characterize

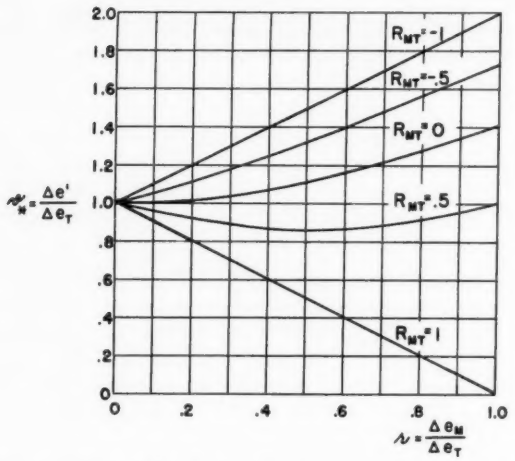


FIG. 1. Fluctuation diagram for 1 per cent mass flow fluctuations and 1 per cent stagnation temperature fluctuations with varying degrees of correlation.

the operation of the wire. Their values vary with the operating conditions of the wire, especially with the wire temperature. When the wire is barely heated, $\Delta e_M \to 0$ and the wire responds mainly to stagnation temperature fluctuations. When the wire is well heated (a tungsten wire can be heated up to about 300°C. without danger of oxidation), the two sensitivity constants are about equal indicating that we cannot achieve mass flow fluctuation sensitivity alone.

With a single wire we are unable to separate the different fluctuations; however, if our interest is the measurement of the mean square fluctuations, we can obtain those by taking repeated readings with the same wire at different operating conditions (i.e., different wire temperatures).

The mean square fluctuation of the hot-wire output

$$\overline{\Delta e^2} = \Delta e_T{}^2\overline{\vartheta^2} + \Delta e_M{}^2\overline{m^2} - 2\Delta e_T \Delta e_M \overline{m\vartheta} \qquad (51)$$

has three contributions: mean square stagnation temperature fluctuations $\overline{\vartheta^2}$, mean square mass flow fluctuations $\overline{m^2}$, and the correlation $\overline{m\vartheta}$ (cross-correlation) between mass flow and stagnation temperature fluctuations. Taking three readings at three different wire temperatures, we obtain three different sets of corresponding values of $\overline{\Delta e^2}$, $\Delta e_M$, and $\Delta e_T$, and we can solve three linear equations for the three unknown quantities $\overline{\vartheta^2}$, $\overline{m^2}$, and $\overline{m\vartheta}$.

Naturally we often find that the mean square voltage has experimental error and that we desire a more "graphic" description of the situation. This desire has lead to the introduction of the "fluctuation diagram."

We define a "virtual stagnation temperature fluctuation" $\vartheta_*$

$$\vartheta_*{}^2 = \frac{\overline{\Delta e^2}}{\Delta e_T{}^2} = \overline{\vartheta^2} - 2r\overline{m\vartheta} + r^2\overline{m^2} \qquad (52)$$

where $r = \Delta e_M/\Delta e_T$ is the sensitivity ratio.

Plotting $\vartheta_*$ versus $r$, we obtain the "fluctuation diagram." The sensitivity ratio is almost synonymous with wire temperature, and for tungsten wires the sensitivity ratio is almost equal to $a_W'$, the overheating ratio of the wire.

$$a_W' = (R_W - R_e)/R_e \qquad (53)$$

where $R_e$ is the resistance of the wire at equilibrium (unheated) temperature and $R_W$ is the resistance at actual temperature $T_W$. For an unheated wire, $a_W' = 0$.

Fig. 1 shows a fluctuation diagram for 1 per cent mass flow fluctuation and 1 per cent r.m.s. stagnation temperature fluctuation with varying degrees of positive and negative correlation.

$$m' = \sqrt{\overline{m^2}}, \quad \vartheta' = \sqrt{\overline{\vartheta^2}}, \quad R_{MT} = \overline{m\vartheta}/m'\vartheta'$$

Although the fluctuation diagram enables us to determine $m'$, $\vartheta'$, and $R_{MT}$, it does not reveal how the mass flow fluctuations and stagnation temperature fluctuations should be attributed to the different fluctuation modes; however, a closer investigation reveals that all three fluctuation modes (vorticity, entropy, sound) have distinctly different fluctuation diagrams.

### *Fluctuation Diagrams of the Different Modes*

If only one of the three fluctuation modes occurs in the supersonic flow, we can work out explicitly its fluctuation diagram. For our present purpose we shall use only the simplified forms characterized by Eqs. (33), (34), and (35).

*Vorticity Mode (Turbulent Velocity Fluctuations).*—The flow field is solenoidal and there are no pressure, density, or temperature fluctuations. The hot wire will respond to only $\Delta U$, the $x$ component of the velocity fluctuation field. Introducing the nondimensional velocity fluctuations in the direction of the main flow

$$u(t) = 100[\Delta U(t)/\bar{U}] \qquad (54)$$

The mass flow and stagnation temperature fluctuations become [Eqs. (44) and (47)]

$$m = u \qquad (55)$$

$$\vartheta = \beta u \qquad (56)$$

The voltage output of the wire

$$\Delta e/\Delta e_T = (\beta - r)u \qquad (57)$$

or

$$\vartheta_* = |\beta - r|u' \qquad (58)$$

The fluctuation diagram consists of two straight lines intersecting at $r = \beta$ and having slopes of absolute magnitude $u'$. The response to velocity fluctuations becomes zero when $\beta = r$. This is an important operating point of the hot wire, since it is sensitive only to the two other modes (entropy mode and sound waves).

Fig. 2 gives the fluctuation diagram for different Mach Numbers for solenoidal velocity fluctuations

that have an r.m.s. value of 1 per cent of the mean velocity.

*Entropy Spottiness.*—In the simplified form the entropy mode is another "frozen pattern" just as is the solenoidal velocity pattern (vorticity mode). We also neglect the potential velocity pattern set up by the decay of the temperature spots. There are no pressure fluctuations, but there are density fluctuations. The mass flow fluctuations and stagnation temperature fluctuations both are nonzero. The temperature fluctuation is defined as

$$\Theta = 100(\Delta T_s/\bar{T}_0) = 100\alpha s \tag{59}$$

From Eqs. (44) and (47),

$$\vartheta = \Theta \tag{60}$$

$$m = \Theta/\alpha = 100s \tag{61}$$

The voltage output of the hot wire becomes

$$\Delta e/\Delta e_T = [1 + (r/\alpha)]\Theta \tag{62}$$

or

$$\vartheta_* = [1 + (r/\alpha)]\Theta' \tag{63}$$

The fluctuation diagram shown in Fig. 3 is a straight line intercepting the $r$ axis at $r = -\alpha$. Since $r$ cannot be made negative, no operating condition of the wire exists where the sensitivity for entropy spottiness vanishes. For wind-tunnel measurements it is more convenient to use, in place of $s$, the nondimensional temperature fluctuation $\Theta$ expressed in per cent of the total mean temperature than expressed relative to the free-stream temperature, especially because the total temperature changes relatively little in a wind tunnel even when the Mach Number varies through a wide range.

*Sound Waves.*—This mode of fluctuation is somewhat different from the previous two modes. Both the vorticity and entropy modes are "frozen patterns" altered only by slow diffusion, but the sound waves are propagating rapidly with respect to the fluid. The propagation velocity is the speed of sound with respect to the fluid, but the apparent propagation velocity with respect to the tunnel depends on the orientation of the waves. In a supersonic tunnel, sound waves can propagate both upstream and downstream and can even be stationary (Mach waves).

The governing differential equation in the simplified form is Eq. (34). Introducing the velocity potential $\varphi$,

$$\Delta\rho/\bar{\rho} = P, \qquad \boldsymbol{v} = \text{grad } \varphi$$

$$P = (1/a^2)(\partial\varphi/\partial t) \tag{64}$$

$$\Delta T/\bar{T} = (\gamma - 1)P \tag{65}$$

A plane wave solution propagating in the direction $\boldsymbol{n}$ is

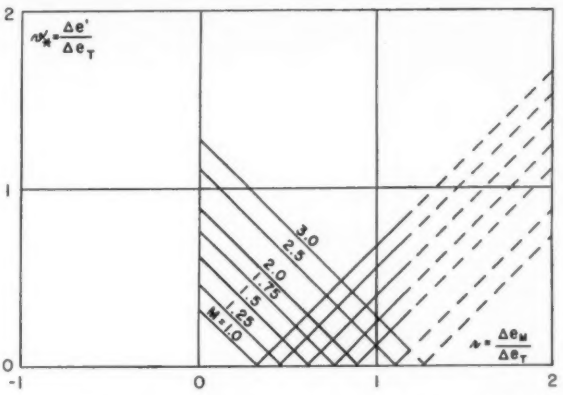


FIG. 2. Fluctuation diagram for 1 per cent turbulent velocity fluctuations (vorticity mode).

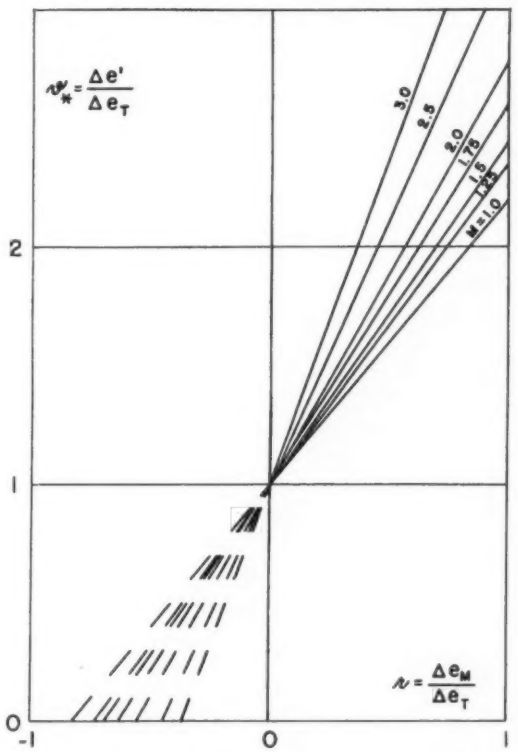


FIG. 3. Fluctuation diagram for 1 per cent temperature spottiness (entropy mode).

$$P = P_0(\boldsymbol{n}\cdot\xi - at) \tag{66}$$
$$\boldsymbol{n}^2 = 1$$

where $P_0(\eta)$ is an arbitrary function of $\eta$. The velocity field is

$$v_1 = an_1P_0(n_1\xi_1 + n_2\xi_2 + n_3\xi_3 - at) \tag{67a}$$
$$v_2 = an_2P_0(n_1\xi_1 + n_2\xi_2 + n_3\xi_3 - at) \tag{67b}$$
$$v_3 = an_3P_0(n_1\xi_1 + n_2\xi_2 + n_3\xi_3 - at) \tag{67c}$$

The mass flow and stagnation temperature fluctuations are functions of the orientation of the wave [Eqs. (44) and (47)]

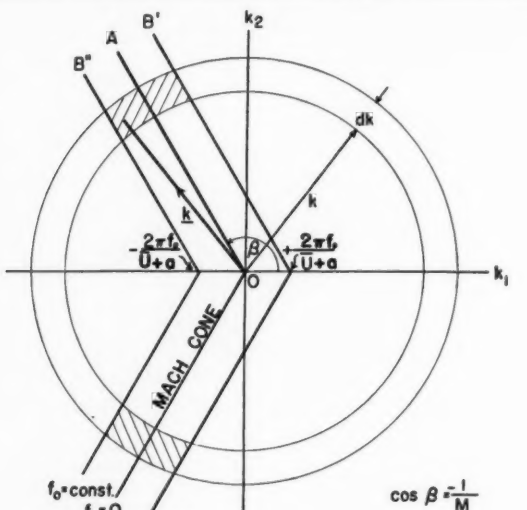


FIG. 4. Cones of constant observed frequency $f_0$ in wave number space for plane sound waves.

$$m = 100\left(\frac{n_1}{M} + 1\right) P_0(\boldsymbol{n}\cdot\boldsymbol{\xi} - at) \tag{68}$$

$$\vartheta = \alpha(\gamma - 1)(1 + n_1 M) P_0(\boldsymbol{n}\cdot\boldsymbol{\xi} - at) \tag{69}$$

When the sound wave becomes a Mach wave or

$$n_1 = -1/M \tag{70}$$

the stagnation temperature fluctuation vanishes. This is a well-known fact obtained as a limiting case from an oblique stationary shock wave through which the enthalpy is unchanged.

The voltage fluctuation across a hot wire is

$$\Delta e(t) = 100\left[\Delta e_T \alpha(\gamma - 1)(1 + n_1 M) - \Delta e_M\left(\frac{n_1}{M} + 1\right)\right] P_0(t) \tag{71}$$

As we see, there is no typical fluctuation diagram for sound waves of all orientations. However, taking the finite frequency resolution of the hot-wire anemometer into account restricts the problem.

The sound waves move with respect to the medium, and the medium is translated by the supersonic mean velocity. If we treat plane sinusoidal sound waves of wave length $\lambda$, the sound-wave field can be expressed by the vector wave number

$$\boldsymbol{k} = (2\pi/\lambda)\boldsymbol{n} \qquad (\boldsymbol{n}^2 = 1) \tag{72}$$

$$P = P_k \exp i[k_1\xi_1 + k_2\xi_2 + k_3\xi_3 - akt] \tag{73}$$

Introducing the coordinate system fixed with respect to the tunnel $(x, y, z)$, we find that the observed frequency $f$ of the sinusoidal plane waves depends on the vector wave number.

$$P = P_k \exp i[k_1 x + k_2 y + k_3 z - 2\pi f t] \tag{74}$$

where

$$f = (ka + k_1\bar{U})/2\pi \tag{75}$$

The observed frequency becomes zero when the wave becomes a Mach wave. The situation can be clearly seen in the wave number space given in Fig. 4. A vector $k$ represents a train of sinusoidal plane waves characterized by their wave length and orientation. Disturbances that appear as fluctuations of a given frequency $f_0$ to the fixed observer have wave number vectors forming two hyperboloids with asymptotic cones $B'$ and $B''$ parallel to the cone of zero observed frequency $A$ whose apex is at the origin. This particular cone is the Mach cone in wave number space formed by all wave number vectors representing a plane sinusoidal Mach wave train.

The sound waves that are detectable by the hot-wire anemometer, which has a flat frequency response up to $f_0$, must have wave number vectors between the cones of this constant observed frequency. If the sound-wave field is a homogeneous random field, it can be characterized by its three-dimensional power spectrum. If the field is approximately isotropic, the energy distribution is spherically symmetric in the wave number space. It is conceivable that the energy contribution from the small wave numbers (long wave length) is negligible compared with the contribution from the higher wave numbers. In such a case the most significant contribution to the hot-wire signal comes from the shaded area in Fig. 4. This annular volume in wave number space is close to the cone of Mach waves. We can state, therefore, that the principal contribution to the hot-wire signal in this case comes from waves that are almost Mach waves, provided that the contribution from long waves is negligible. Physically, this fact can be understood, since the waves that are close to being Mach waves move with a small velocity with respect to the hot wire; therefore, they can be easily resolved even when their wave length is short.

The fact that intense sound waves steepen up into shock waves can be visualized in wave number space as a strong energy transfer toward the higher wave numbers. The stronger contribution in the high wave numbers, on the other hand, strengthens our previous argument.

Shadow photographs from projectiles often show a sound-wave field emanating from the turbulent boundary layer on the surface of the projectile, and these waves, although not exactly Mach waves, usually have angles close to the Mach waves.

If the detectable sound waves can be assumed to be almost Mach waves, there are no stagnation temperature fluctuations and the mass flow fluctuations alone contribute to the value of $\Delta e(t)$. Hence, the fluctuation diagram is a straight line from the origin. The strength of these sound waves can be characterized most conveniently by the mass flow fluctuations

$$m = \sigma = [1 - (1/M^2)]P \tag{76}$$

or

$$P = [M^2/(M^2 - 1)]\sigma \tag{77}$$

$$\Delta e/\Delta e_T = -r\sigma \tag{78}$$

or

$$\vartheta_* = r\sigma' \tag{79}$$

The fluctuation diagram for sound waves that are the type described above is shown in Fig. 5.

Naturally there are situations in which the sound waves of longer wave length with orientation different from Mach waves contribute significantly to the measured r.m.s. fluctuation. In such a case the fluctuation diagram becomes different from the one shown in Fig. 5, but the present approximation seems to suffice for sound generated by boundary layers, especially by transition bursts.

Fig. 6 gives a summary of the fluctuation diagrams of all three modes at Mach Number = 1.75.

### *Separation of Coexisting Modes*

In an actual flow in the wind tunnel we may expect to find all three modes with different intensities. They may also be either statistically independent or somewhat correlated. Three fluctuating quantities at a point can be described statistically by the joint probability distribution of these three variables. Restricting our interest only to second moments of this joint probability distribution, we find that there are six quantities to specify: the r.m.s. value of the three fluctuations and the three cross-correlation coefficients.

Since we saw that the fluctuation diagram specifies only three quantities, in general, it is not possible to determine all six quantities without some additional information or assumptions.

There are, however, important cases when the determination of only three quantities is necessary. If the level of one of the three modes is negligible compared with the other two, there are only two r.m.s. values and one cross-correlation to be determined.

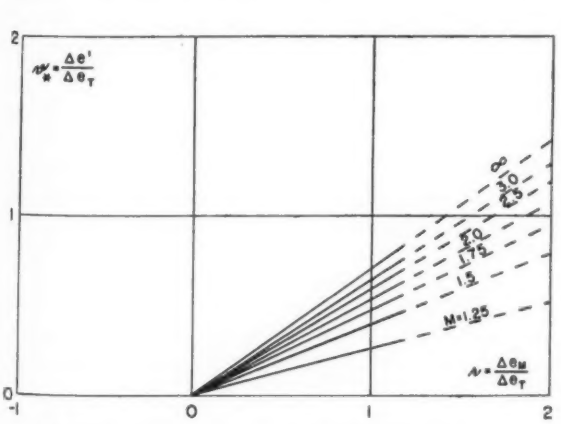


FIG. 5. Fluctuation diagram for sound waves that are almost Mach waves having 1 per cent pressure fluctuations ($\Delta p/\bar{p} = 0.01$).

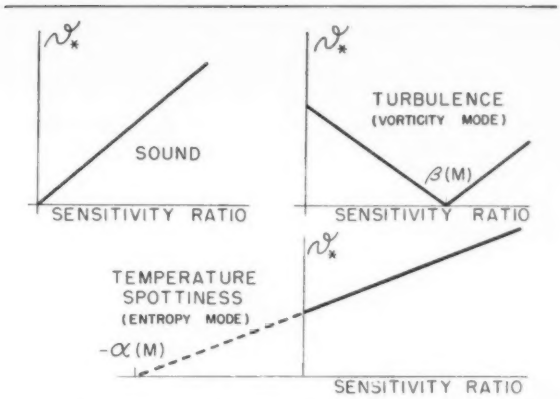


FIG. 6. Comparison of fluctuation diagram for three modes.

Such is usually the case when in a shear flow region both the vorticity mode and entropy mode are so intense compared with the sound waves that the latter can be neglected and the fluctuation diagram can be fully interpreted. Another important case occurs when all three modes can be assumed to be entirely uncorrelated. In this case only the three r.m.s. values need be determined. Both of these special cases can be explicitly solved.

The three fluctuating quantities that are observed at a point as a function of time are defined on a nondimensional basis, using characteristic mean quantities referring to the supersonic flow as contrasted to the quantities $\omega$, $P$, $s$ which were defined disregarding the mean flow.

*Entropy Mode.*—Temperature spottiness is expressed in per cent of the mean stagnation temperature.

$$\Theta(t) = 100[\Delta T_S(t)/\bar{T}_0] = 100\alpha s$$

*Vorticity Mode.*—Solenoidal velocity fluctuation component in the mean flow direction is expressed as per cent of the supersonic mean velocity.

$$u(t) = 100\,\frac{\Delta U_t(t)}{\bar{U}}$$

*Sound-Wave Mode.*—Detectable sound waves that are close to Mach waves. Mass flow fluctuation is expressed as per cent of mean mass flow.

$$\sigma(t) = \left(1 - \frac{1}{M^2}\right)\frac{\Delta p(t)}{\gamma \bar{p}}$$

The fluctuation diagram of all three fluctuations occurring together in the general case can be obtained by combining Eqs. (57), (62), and (78).

$$\vartheta_*{}^2 = \left[\frac{\alpha + r}{\alpha}\,\Theta + (\beta - r)u - r\sigma\right]^2 \tag{80a}$$

or

$$\vartheta_*{}^2 = \left(\frac{\alpha + r}{\alpha}\right)^2\overline{\Theta^2} + (\beta - r)^2\,\overline{u^2} + r^2\sigma^2 + 2\,\frac{\alpha + r}{\alpha} \times$$

$$(\beta - r)\overline{\Theta u} - 2\,\frac{\alpha + r}{\alpha}\,r\overline{\Theta\sigma} - 2\,(\beta - r)r\,\overline{u\sigma} \tag{80b}$$

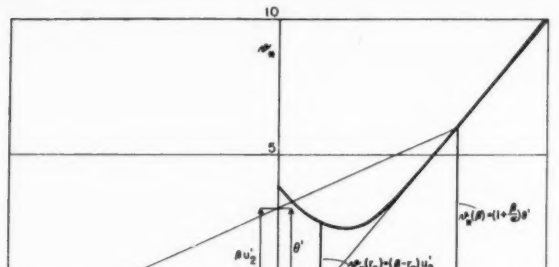

FIG. 7. Fluctuation diagram for 3 per cent temperature spottiness; 7.5 per cent anticorrelated and 5 per cent noncorrelated turbulent velocity fluctuations with sound field neglected; $M = 1.58$; $\alpha = 0.667$; $\beta = 0.667$; $\Theta' = 3$; $\mu' = 9$; $R_{u\Theta} = -0.83$.

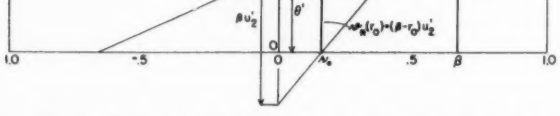


FIG. 8. Fluctuation diagram for uncorrelated modes at $M = 1.75$; temperature spottiness 0.1 per cent; turbulent velocity fluctuations 0.2 per cent; sound waves (detectable) 0.1 per cent of mass flow fluctuations. (Dotted lines show separate contributions.)

Fluctuating quantities can be decomposed into perfectly correlated and uncorrelated parts with respect to another fluctuation. If one fluctuation is chosen as the primary variable, the second fluctuation can be decomposed as the sum of two parts, one perfectly correlated to the first and the other uncorrelated to the first. A third fluctuation can be decomposed into three parts, one part perfectly correlated to the first fluctuation, the second part perfectly correlated to the second part of the second fluctuation, and a third part uncorrelated to both first and second fluctuations. Using these six fluctuation quantities we obtain description equivalent to the three r.m.s. values and three correlations. Using the temperature spottiness as first fluctuation $\Theta$, the velocity fluctuations can be decomposed into two parts:

$$u = u_1 + u_2$$

where $u_1$ = velocity fluctuation perfectly correlated to the temperature spottiness and $u_2$ = velocity fluctuation uncorrelated to the temperature spottiness; and

$$\sigma = \sigma_1 + \sigma_2 + \sigma_3$$

where $\sigma_1$ = sound waves correlated to $\Theta$, $\sigma_2$ = sound waves perfectly correlated to $u_2$, and $\sigma_3$ = sound waves uncorrelated to $\Theta$ and $u$.

The relations defining these fluctuations are

$$u_1(t) = \Theta(t)(\overline{\Theta u}/\overline{\Theta^2}) \tag{81a}$$
$$u_2(t) = u(t) - u_1(t) \tag{81b}$$
$$\sigma_1 = \Theta(t)(\overline{\Theta\sigma}/\overline{\Theta^2}) \tag{81c}$$
$$\sigma_2 = u_2(t)(\overline{u_2\sigma}/\overline{u_2^2}) \tag{81d}$$
$$\sigma_3 = \sigma(t) - \sigma_1(t) - \sigma_2(t) \tag{81e}$$
$$\overline{u_1^2} + \overline{u_2^2} = \overline{u^2} \tag{81f}$$
$$\overline{\sigma_1^2} + \overline{\sigma_2^2} + \overline{\sigma_3^2} = \overline{\sigma^2} \tag{81g}$$

The fluctuation diagram in terms of these six new variables is

$$\vartheta_*^2(r) = \left[\frac{\alpha + r}{\alpha}\,\Theta' + (\beta - r)u_1' - r\sigma_1'\right]^2 + [(\beta - r)u_2' - r\sigma_2']^2 + [r\sigma_3']^2 \tag{82}$$

***Special Case (I)—Sound Waves Are Negligible***

$$\sigma_1' = 0, \qquad \sigma_2' = 0, \qquad \sigma_3' = 0$$

$$\vartheta_*^2 = \left[\frac{\alpha + r}{\alpha}\,\Theta' + (\beta - r)u_1'\right]^2 + [(\beta - r)u_2']^2 \tag{83}$$

The fluctuation diagram for the following values:

$$M = 1.58, \qquad \Theta' = 3, \qquad u_1' = 7.5$$
$$u_2' = 5, \qquad u' = 9, \qquad R_{u\Theta} = -0.83$$

is shown in Fig. 7. These values are realistic and have been encountered in a turbulent supersonic boundary layer.

Three important quantities can be read from the diagram

| | | |
|---|---|---|
| $\vartheta_*(\beta)$ | = | the value $\vartheta_*$ at $r = \beta$ |
| $(d\vartheta_*/dr)_{r=\beta}$ | = | the slope at $r = \beta$ |
| $r = r_0$ | = | the intercept of the slope |
| $\vartheta_*(r_0)$ | = | the value of $\vartheta_*$ at $r = r_0$ |

The three quantities can be obtained as

$$\Theta' = \alpha\vartheta_*(\beta)/(\alpha + \beta) \tag{84}$$
$$u_1' = (d\vartheta_*/dr)_{r=\beta} - (\Theta'/\alpha) \tag{85}$$
$$u_2' = \vartheta_*(r_0)/(\beta - r_0) \tag{86}$$

The value of $\vartheta_*(r_0)$ is somewhat uncertain, since it is often only inferred from the curve when $r_0$ is negative.

***Special Case (II)—Uncorrelated Modes***

When the modes originate at different regions, it is possible that the three modes are uncorrelated. Such may be the case for the residual fluctuations encountered in a good wind tunnel. The fluctuation diagram is convex from below

$$\vartheta_*^2(r) = \left(\frac{\alpha + r}{\alpha}\right)^2 \overline{\Theta^2} + (\beta - r)^2\overline{u^2} + r^2\overline{\sigma^2} \tag{87}$$

By taking three different readings, the three unknowns can be found. Fig. 8 shows a fluctuation diagram of this type.

In actual hot-wire measurements these two special cases were utilized in the evaluation, since the situation found in the turbulent supersonic boundary layer is

close to Special Case (I) and the fluctuations found in the free stream are not unlike Special Case (II).

## (III) Experiments

### *Equipment*

The principal obstacles to the introduction of the hot-wire technique into the supersonic field were of a technical nature. Wires broke in the supersonic stream, and no electronic equipment was available which would give sufficient time resolution.

The first measurements in supersonic flow were taken by the author with two purposes in mind. One was the verification of the previously expounded general ideas about fluctuation modes; the other was to perform exploratory measurements in turbulent flows in order to estimate orders of magnitude of fluctuations and the relative importance of different phenomena encountered.

The wires used in the measurements at Johns Hopkins were tungsten wires of 0.00015 in. diameter. They were electroplated with copper leaving a bare portion 0.070 in. long and mounted by soft solder between needles set 0.110 in. apart. The copper-coated portion provided insensitive supports in the region behind the conical shock waves produced by the needle tips. It was found that many wires were lost because of fatigue failure of the copper sleeve, especially when the wires were operated in a highly turbulent shear region such as the turbulent boundary layer close to the wall. A drop of rubber cement at the soldered points provided satisfactory damping. Fig. 9 shows the arrangement. Such wires had long records of use, and one was operated for 14 hours in the supersonic tunnel, accomplishing a "mileage" of approximately 14,000 miles. We consider this record quite satisfactory.

The electronic equipment is described briefly in reference 9 and in detail in reference 11. The useful frequency range of the combined hot wire and compensating amplifier is 2–70,000 cycles per sec. The noise level is correspondingly high. With the time-lag compensation level of $0.3\text{–}0.5 \times 10^{-3}$ sec., the minimum detectable fluctuation is about $0.2mV$ root mean square.

The wire was overheated above equilibrium temperature $T_e$ by an amount varying from 15° to 300°C., and the sensitivity ratio $r$ varied between 0.05–1.00. At Mach Number 1.75, the fluctuation diagram should be extended up to about $r = 0.75$, but at lower Mach Numbers (within boundary layer) a lower limit was sufficient.

### *Measurement of Pure Temperature Spottiness*

One of the earlier experiments was performed in 1951 in the Bomb Tunnel of the Ballistic Research Laboratories, Aberdeen Proving Ground. The fluctuation level was determined in the working section of the tunnel at Mach Number 1.73. The above-described ideas about fluctuation "modes" were not yet crystallized, and the measured data were filed away. However, it was suspected that the fluctuations were principally temperature spots, and their cause was determined later. The arrangement of the tunnel was such that the working section was supplied from four independent compressors, each having separate aftercoolers discharging four air streams of different temperature into the supply section. It was conjectured then that, with the drifting of the relative temperature levels in the four units, the temperature differences could vary, and therefore the intensity of temperature spottiness would vary from run to run. At the conclusion of the measurements this condition was remedied, but later the entire tunnel was abandoned in favor of a newer design.

It was rather interesting, however, to replot the 1951 data in the light of present findings. Fig. 10 shows the fluctuation diagram with the straight line intercepting at $r = -\alpha$ corresponding to pure temperature spotti-

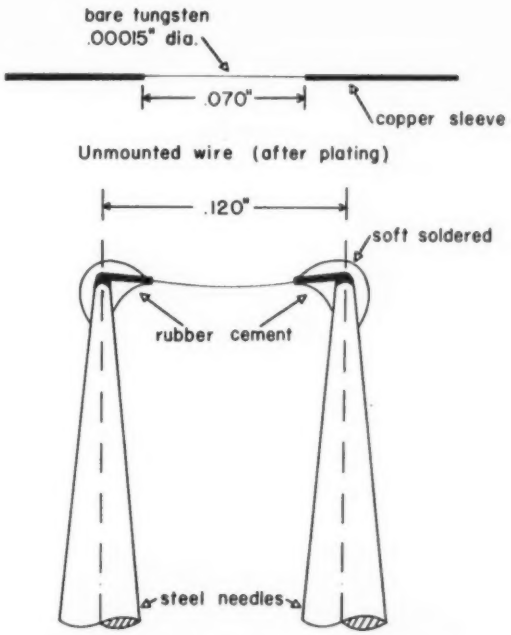


Fig. 9. Hot-wire mounting for supersonic flow.

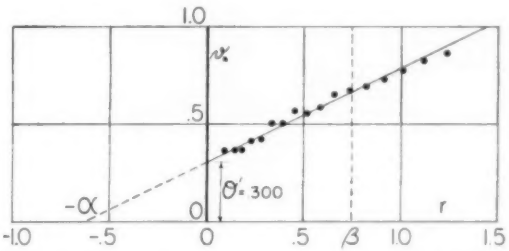


Fig. 10. Fluctuation diagram obtained in 1951 in the Aberdeen Bomb Tunnel; $M = 1.73$. Pure temperature spottiness, $\Theta' = 0.3$, explains results.

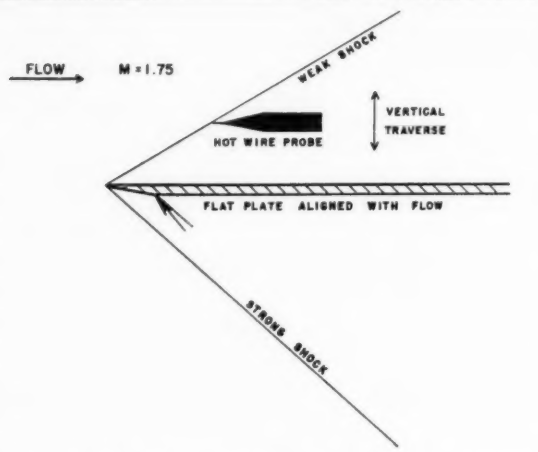


FIG. 11. Hot-wire detection of random shock-wave oscillations.



FIG. 12. Hot-wire signal obtained from oscillating weak shock wave; $M = 1.75$; $\Delta(\rho U)/\bar{\rho}\bar{U} = 0.04$; calibrating sine wave 200 cycles per sec.

ness (compare with Fig. 3). It is now believed that this one mode was so strong that it overcame the residual fluctuations due to other modes present in the working section.

### *Detection of Weak Waves*

Mach waves or weak shock waves that appear stationary in a wind tunnel actually do oscillate either in a regular or in a random manner. If a hot wire is placed at the average position of such a wave, we can regard the flow field in two ways. From a coordinate system fixed to the wind tunnel we have a slightly moving, almost stationary, wave, and the hot wire is upstream for a portion of the time and downstream otherwise. From a coordinate system moving with the mean flow, these waves are almost plane sound waves with orientation close to the Mach angle. The fluctuation diagram should correspond to Fig. 5.

A hot-wire probe was placed into a weak shock wave produced by the leading edge of a flat plate. Fig. 11 shows the disposition. The hot-wire signal is shown in Fig. 12. It appears as a random square wave, indicating that the hot wire oscillates in a random fashion between two distinct states. From mean flow (d.c.) hot-wire measurements taken before and after the shock wave, it was established that the mean mass flow change across the wave is about 4 per cent corresponding to a flow angle deflection of $^1/_2$ deg.

The fluctuation diagram is given in Fig. 13. The diagram indicates pure sound waves as in Fig. 6. The mass flow fluctuation indicated is 1.7 per cent r.m.s. If the mean mass flow change is 4 per cent across the wave, a pure square wave fluctuation would correspond to $\pm 2$ per cent variation or to a 2 per cent r.m.s. value. On the other hand, a sine wave type fluctuation with a 4 per cent peak-to-peak amplitude would give only a 1.41 per cent r.m.s. fluctuation. Since the oscillographic records indicated trapezoidal fluctuations, the 1.7 per cent found from the fluctuation diagram is well bracketed by the 1.41 and 2 per cent values. The fluctuation diagram indicates that there are other fluctuations present (nonzero intercept) besides the dominating sound waves.

### *Detection of Turbulent Regions by the Hot Wire*

Naturally the detection of transition in a supersonic boundary layer is of paramount interest. Generally speaking, it is not difficult to distinguish between the appearances of a hot-wire signal on the oscilloscope when the wire is in a true turbulent region or in a sound field emanating from a turbulent region.

The author carried out some preliminary experiments in the 6- by 6-in. heat-transfer tunnel at Ames Aero-

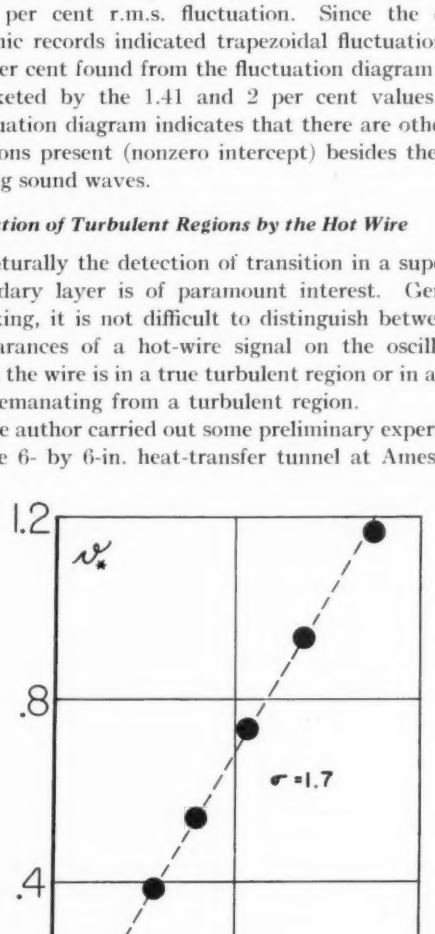


FIG. 13. Fluctuation diagram for random oscillating weak shock wave (arrangement in Fig. 11).

nautical Laboratory of the National Advisory Committee for Aeronautics during the summer of 1952. An instrumented flat plate was explored with a hot-wire anemometer (the wire was a 0.0003 in. diameter tungsten about 0.200 in. long welded to steel needles). The arrangement is shown in Fig. 14. The suction slot was intended to remove the entire turbulent boundary layer from the tunnel wall before the flat plate. It was found that at low Reynolds Numbers (low pressure) the hot-wire still indicated intermittently turbulent bursts, and a strong vibration of the leading edge shock wave was also observed by the hot-wire probe.

Detailed exploration showed the following state of affairs: The corrugated outer boundary of the turbulent boundary layer had crests that spilled above the leading edge, causing turbulent bursts in the otherwise laminar boundary layer. When the Reynolds Number was low, these bursts drifted downstream in the laminar boundary layer without much growth, making the boundary layer turbulent only a small fraction of the time. This picture also explained the generally laminar character of the boundary layer as detected from an averaging type of instrumentation (recovery factor measurement). However, at somewhat higher Reynolds Numbers, the boundary layer was found in a slow state of transition, with the turbulent bursts gradually overtaking the entire boundary layer. This explained some of the anomalous results obtained in the same boundary layer by other experimental means.

Even an experiment of such a preliminary nature proved that hot-wire measurements of a qualitative character can greatly increase the understanding of peculiar phenomena, since it gives a detailed and instantaneous picture rather than merely long time-averaged effects.

### *Turbulence Measurements in the Supersonic Boundary Layer*

After the above-described preliminary experiments, the exploration of the supersonic turbulent boundary layer was undertaken. The Department of Aeronautics at The Johns Hopkins University has a closed circuit continuously operating supersonic wind tunnel with a 7- by 11-in. working section. The tunnel is operated at a Mach Number of 1.75 and at atmospheric stagnation conditions ($p_0$ = 80 cm. Hg; $\bar{T}_0$ = 300°K.). The most conveniently available boundary layer located on the ceiling of the working section was chosen for the experiment. Its thickness was approximately 0.500 in. Since no previous measurements were performed on turbulent fluctuations in a supersonic boundary layer, it was felt that the thickness was more at a premium than the controlled history of the layer.

The probe mechanism permitted definition of a distance about ±0.002 in., which we considered satisfactory since only the exploration of the supersonic portion of the layer was planned.

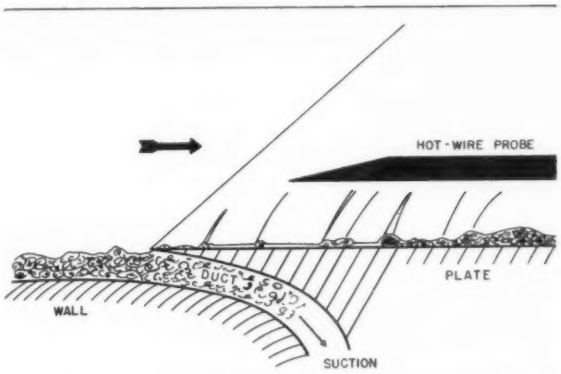


FIG. 14. The turbulent boundary layer on the tunnel wall is not removed completely. Intermittent bursts are caused by peaks of turbulent boundary layer contaminating laminar boundary layer on flat plate (Ames, NACA, 1952).

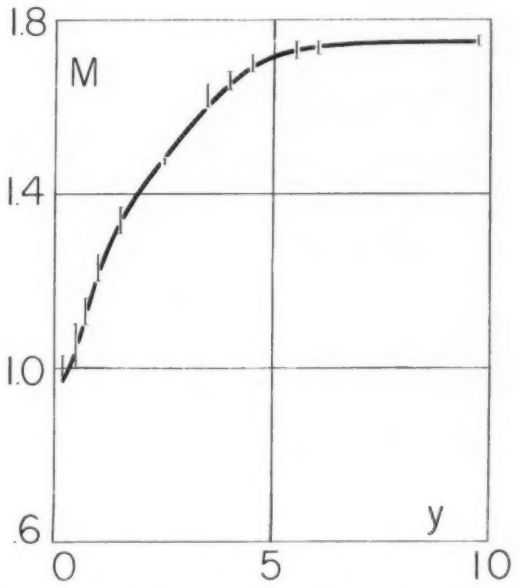


FIG. 15. Mach Number distribution across turbulent boundary layer.

Preliminary traverses indicated the following facts: The hot-wire signal is extremely characteristic when the outer edge of the layer is reached. The intermittent outer edge causes a strongly one-sided asymmetrical signal that gives the appearance of "growing grass" as the probe plunges into the layer. The signal is rather high just as in low-speed turbulent boundary layers, but the fluctuations are rapid and the frequencies observed reach well into the 30–40 kc. range.

The mean total temperature does not seem to vary across the layer within the accuracy of detection (about 2°C.). Mean mass flow measurements, on the other hand, can easily be performed. With the assumption of constant total temperature (enthalpy) and constant pressure across the layer, the mean velocity and Mach

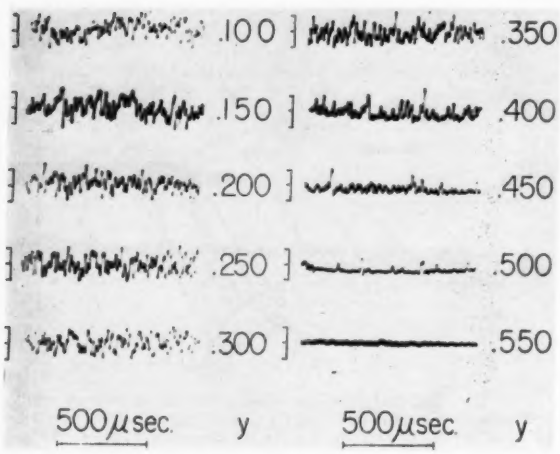


FIG. 16. Hot-wire signal in turbulent boundary layer; $M$ = 1.75. Vertical scale indicates approximately ±10 per cent mass flow fluctuations.

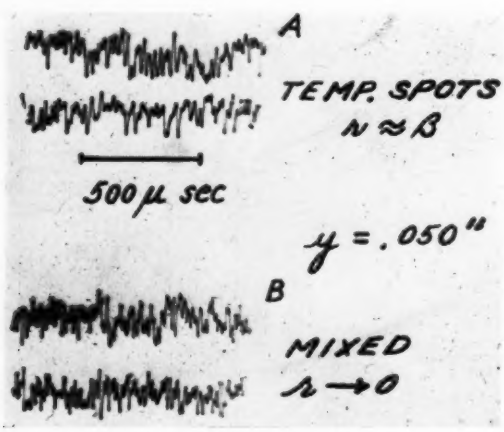


FIG. 17. Hot-wire signal shows different character with different overheating when close to wall; (A) temperature spottiness alone, $\Theta$; (B) equal sensitivity for $\Theta$ and $u$.

Number distribution can easily be determined. Fig. 15 shows the mean Mach Number distribution across the layer.

The experimental scatter of different sets of measurements is also indicated. The hot wire naturally is not the best instrument for mean flow measurements, since its advantage lies primarily in its ability to resolve rapid fluctuations, but it is still available for measuring mean properties with the degree of accuracy shown in Fig. 15.

The character of the hot-wire signal at different distances from the wall is shown in Fig. 16. The amplification is approximately the same in all records, and the marks on the amplitude scale indicate ±10 per cent mass flow departure from the mean mass flow. The strong "single-sided" character of the signal close to the outer edge is visible. After the rough exploration the real question was to establish what modes of fluctuations were present.

Fluctuation diagrams were taken at different locations within the boundary layer and just outside of it. As a result of these measurements it was decided that the sound waves may be neglected within the turbulent boundary layer compared with the larger turbulent velocity fluctuations and temperature spottiness. Since the mean flow has no discontinuity at the outer edge of the boundary layer, it is believed that the sound generated within the boundary layer propagates freely through the outer boundary and may only suffer some scattering, but essentially no appreciable reflection back into the layer. If this contention is true, the intensity of sound waves just outside of the boundary layer cannot be substantially different from its intensity just inside the layer unless there is some mechanism that would "trap" the sound waves within the boundary layer. The sound-wave level, expressed as $\sigma'$ (r.m.s. mass flow fluctuation), certainly did not exceed 0.2 per cent just outside of the boundary layer and most likely was only 0.1 per cent. On the other hand, the turbulent velocity fluctuation in the boundary layer was of the order of 2–3 per cent. Such being the case, the author believes that the effect of sound waves may be neglected in evaluating the fluctuation diagram from the signals within the boundary layer. This statement does not imply that the sound waves are negligible as a physical phenomenon. It only neglects their contribution to the overall mass flow fluctuation level. Sound level is usually given in a decibel scale. Fluctuations in turbulence are given as per cent of mean flow properties. The sound levels that are negligible for our purposes may still be enormous in the ordinary sound intensity scales. This simplification, however, seems to be legitimate only in highly turbulent sheer regions where turbulence and temperature spottiness are so predominant.

Using this assumption the fluctuation diagram could be interpreted unequivocally. It was found that both turbulent velocity fluctuations and temperature spottiness are rather intense. It was also found that there is a high negative correlation ($R_{\Theta u} \approx -0.7$) between the velocity fluctuation and temperature spottiness. This fact can be interpreted to mean that, whenever a lump of fluid is encountered which is warmer than the average, it comes from a layer closer to the wall and has also a momentum defect giving a negative velocity fluctuation compared with the mean value. Because of this high negative correlation between velocity and temperature, the character of the oscillograph traces did not vary much with changes in the overheating of the wire (or changing $r$), at least in the outer layers of the boundary layer. However, close to the wall, especially at $y = 0.050$ in., the signal exhibited a different character by changing the wire's sensitivity to different fluctuation modes.

Fig. 17 shows the difference in traces at $y = 0.050$ in. with sensitivity ratios $r = 0.7$ (marked "TEMP.

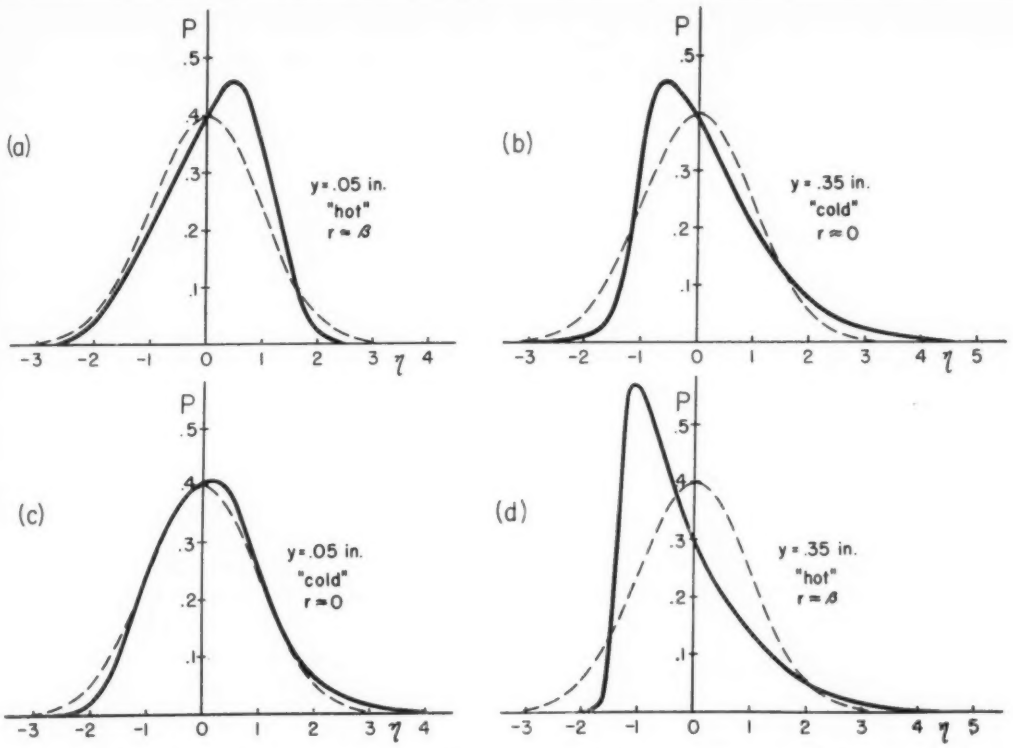


FIG. 18. Probability density of hot-wire signals at two locations in boundary layers with two different sensitivity ratios.

SPOTS") and $r = 0.05$ (marked "MIXED"). The first case gives sensitivity to temperature spottiness alone; in the latter case there is about equal sensitivity to temperature spottiness ($\Theta$) and to turbulent fluctuations ($u$). There is a noticeable "spikiness" downward indicating cold intermittent spots. This spikiness, however, disappears when the sensitivity is not predominantly for $\Theta$. Since the oscillographic records give short samples from which to make statistical inferences, it was felt that obtaining the probability density function of the signals would be more instructive. Probability densities were determined by taking long (1 min.) exposures on rather insensitive plates from the face of the cathode-ray scope. Reference signals gave the standard deviation, and the photographic process was standardized and calibrated.

Photodensity measurements gave the probability density curves that are shown in Fig. 18. All of the curves have the same standard deviation, and a Gaussian distribution is shown for comparison. The signal is positive (wire hotter) toward the right.

Two locations in the boundary layer ($y = 0.050$ in. and $y = 0.350$ in.) are compared; one is in the outside region where the intermittency of the outer boundary gives single-sided pulses toward the positive direction (the wire becomes hotter whenever the probe is within the hotter and slower fluid of the boundary layer as compared with the free stream). The other location is at $y = 0.050$ in., where the situation is different. With the wire sensitive to temperature spottiness, the single-sided character is reversed, indicating that cool spots may cause a pulse structure. However, when the wire is sensitive to both modes, the probability density returns closer to Gaussian.

The author must confess that this peculiar phenomenon occurring close to the wall ($y = 0.050$ in.) and also suggestively close to the sonic region of the layer ($M = 1$) is not satisfactorily explained as yet, and it is not even clear whether it is a real phenomenon of the turbulent supersonic boundary layer or merely an instrumentation phenomenon connected with operating a probe in the shear layer close to the Mach number unity.

The distribution of fluctuation intensities is given in Fig. 19. The r.m.s. temperature spottiness $\Theta$ is given in per cent of the total temperature. If the temperature spottiness were given as per cent of the temperature difference across the layer (about 40 per cent of the mean total temperature), the two curves ($u'$ and $\Theta'$) would be almost identical, suggesting the not too surprising fact that the momentum and heat transfer across the shear layer are similar; therefore the fluctuation levels are also of the same order of magnitude.

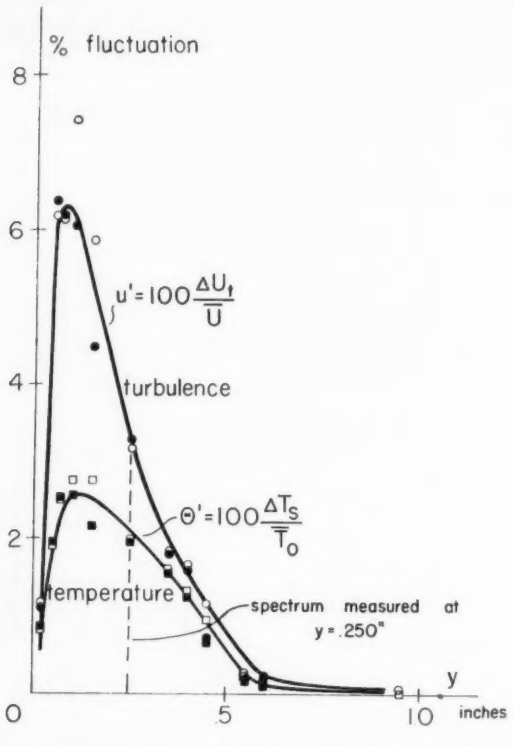


FIG. 19. Temperature spottiness and turbulent velocity fluctuations in turbulent boundary layer.

Naturally the hot wire resolves only the large eddies in the layer. A measurement of the energy spectrum was performed in the range 500–70,000 cycles per sec. The results were plotted in Fig. 20 in the nondimensional representation used by Klebanoff and Diehl in reference 14. The intercept of the spectrum at zero wave number (frequency) determines the integral scale $L_x$. When the nondimensional plot was compared with the data obtained for low-speed boundary layer, essentially one parameter is free and can be adjusted. We found that the data from the supersonic layer at $y = 0.250$ in. matched surprisingly well with the choice $L_x = 0.110$ in. This value is about a quarter of the boundary-layer thickness (0.500 in.) as contrasted to the findings in low-speed boundary layers[14] where $L_x$ was found to be about 40 per cent of the boundary-layer thickness. This disagreement of a factor of 2 is not too surprising, since a low-speed boundary layer at moderate Reynolds Number has been compared with a supersonic boundary layer of much higher Reynolds Number.

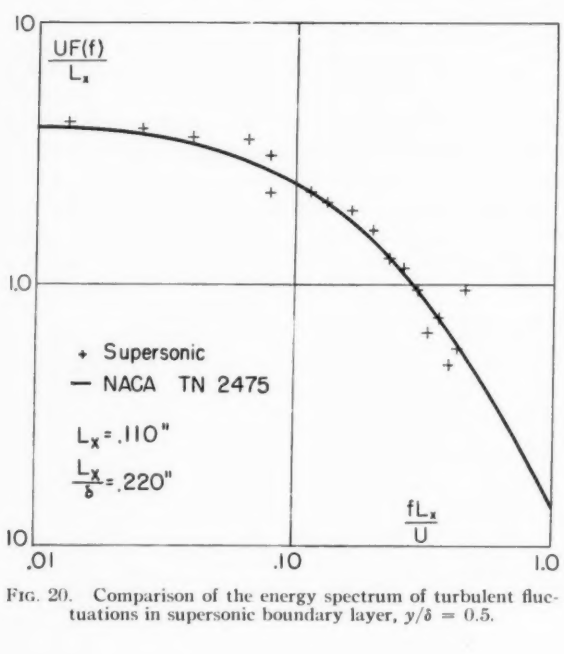


FIG. 20. Comparison of the energy spectrum of turbulent fluctuations in supersonic boundary layer, $y/\delta = 0.5$.

## CONCLUSIONS

(A) Random fluctuations in a supersonic flow can be decomposed into three distinct modes: vorticity, sound, entropy. The modes obey separate linear differential equations if the fields are weak and have moderate interaction if the fields are stronger.

(B) If the spatial scale of the disturbances is not too small, the effect of viscosity and heat transfer can be neglected for the short-time history of the disturbances, and the velocity, pressure, and temperature fields can be easily split into the three modes. The velocity field is split into a solenoidal and an irrotational field. The former constitutes the vorticity mode; the latter belongs to the sound waves. The pressure fluctuations belong to the sound-wave mode. The density and temperature fluctuations are split into isentropic fluctuations that belong to the sound-wave mode and into a nonisentropic part that constitutes the entropy mode. The vorticity mode has no pressure, density, or temperature fluctuations.

(C) The hot-wire anemometer can be operated successfully in a supersonic flow. The key to separation of the modes is the "fluctuation diagram" representing the r.m.s. output of a hot wire at different operating wire temperatures.

(D) A variety of preliminary hot-wire measurements in supersonic wind tunnels indicate that all three modes are significant but that their relative importance may vary from one flow region to another. Sound waves may have more relative importance in the "free stream" and the other two in shear layers (boundary layers, wakes). The entropy mode (temperature spottiness) was always significant when the vorticity mode (turbulent velocity fluctuations) was intense.

(E) The fluctuation field in a supersonic turbulent boundary layer appears to be similar to a low-speed boundary layer. The only important difference is the intense temperature spottiness caused by the intense turbulent heat transfer across the layer.

(*Concluded on page 682*)

# The Effect of Boundary Layer on Sonic Flow Through an Abrupt Cross-Sectional Area Change*

ROBERT S. WICK†

*California Institute of Technology*

SUMMARY

It has long been known that the pressure at the base of high-speed projectiles is lower than the ambient pressure. Since experimental work on projectiles has indicated that the boundary layer definitely affects the base pressure, it was decided to investigate the effect of the boundary layer on the similar phenomena occurring in internal sonic or supersonic flow through a sudden enlargement of cross section.

A two-dimensional flow channel consisting of a convergent section, a straight section, and an enlarged section connected in series was constructed. The flow reached sonic velocity at the end of the throat section and expanded suddenly into the enlarged section. The boundary layer in the throat was varied by changing the mass rate, pressure, and the length of the throat. The expansion ratio (throat area to expanded section area) was also varied.

The results of these experiments indicated definitely that the pressure in the corner of the expansion was related to the boundary-layer type and thickness upstream of the expansion. A dimensional analysis was used to correlate the results over a range of area expansion ratios and boundary-layer thicknesses, and a "jet-pump" concept was devised which explained qualitatively the effects observed. Means of comparing the results of internal flow over corners and through sudden expansions in area to external flow over corners were also considered.

NOMENCLATURE

$A_1, A_2$ = upstream and downstream internal cross-sectional areas
$B$ = angle between arc and expansion line (Fig. 2)
$H_1, H_2$ = height of upstream and downstream section of two-dimensional test apparatus (Fig. 4)
$L_1, L_2$ = length of upstream and downstream section in test apparatus (Fig. 4)
$M$ = Mach Number
$P$ = pressure
$R$ = radius from corner to expansion line (Fig. 2)
$Re_{L_1}$ = Reynolds Number at entrance to expansion based on $L_1$ as length
$W$ = width of two-dimensional test apparatus
$X, Y$ = rectangular coordinates (Fig. 2)
$\alpha$ = Mach angle
$\theta$ = angle isentropic flow turns through to reach Mach Number $M$
$\phi$ = direction of characteristics (Fig. 2)
$\gamma$ = ratio of specific heats

*Subscripts*

1 = conditions upstream of expansion
2 = conditions downstream of expansion
4 = conditions at exit of apparatus (atmospheric)
$b$ = conditions in corner between upstream and downstream
0 = stagnation conditions

Received May 25, 1953.

* The experimental work described in this paper was done at the University of Illinois as part of a thesis submitted in partial fulfillment of the requirements for the degree of Doctor of Philosophy.

† Senior Research Engineer, Jet Propulsion Laboratory.

## INTRODUCTION

WHEN THERE IS A SUDDEN INCREASE in flow cross-sectional area in either external or internal flow, a jet boundary will usually appear at the corner which separates the main flow from the wake in the corner. The pressure in the corner downstream of such an expansion, whether for internal flow or for flow over a projectile, is referred to as the *base pressure*. In 1776, Jean-Charles Borda[1] investigated the flow of water through a sudden increase of duct cross section, and the resultant Borda-Carnot formula is still considered to give a fair estimate of the head loss that occurs in sudden enlargements of cross section. Nusselt[2] appears to be one of the first to conduct experimental tests with high-velocity gas flow (subsonic flow of air and steam) through sudden increases in flow cross section. He later concluded from his more extensive experiments with sonic and supersonic flow[3] that the base pressure will be equal to the entrance pressure if the entrance velocity is subsonic; but, if the entrance flow is supersonic, the base pressure could be equal to, less than, or greater than the entrance pressure. The base pressure ratios (defined as the ratio of the pressure at the base to the pressure upstream of the corner) that Nusselt obtained for supersonic flow in the entrance to the expansion ranged from 1.138 to 0.992 for a 4 to 1 area increase and 1.294 to 0.695 for a 6.37 to 1 area increase. In his experiments, Nusselt used both a convergent nozzle ($M_1 = 0.970$ to 0.981) with no straight (constant area) section and a Laval nozzle for the supersonic ($M_1 \leq 2$) cases. No attempt was made by Nusselt to determine the factors governing the base pressure, although a one-dimensional analysis based on the continuity, energy, and momentum equations was made. This, as will be shown later, is not usually satisfactory.

Workers in the field of ballistics have long been concerned with the problem of sudden expansions of external compressible flow over the rear of projectiles

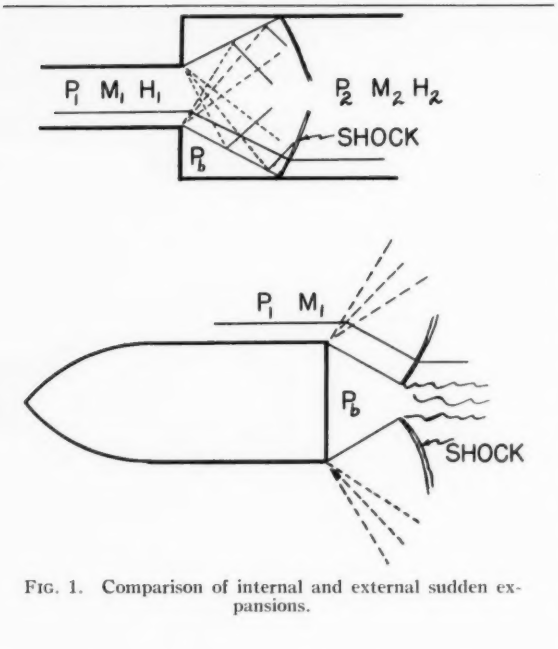


FIG. 1. Comparison of internal and external sudden expansions.

and its interrelationship with the base pressure because the base drag, which is a considerable portion of the total drag, depends directly on the base pressure. It has long been known that the pressure at the base of high-speed projectiles is lower than the ambient pressure, and the manner in which most ballistics test data have been presented would lead one to the conclusion that the base pressure ratio is only a function of the flight Mach Number. In a series of postwar tests, Chapman[4] and Kurzweg[5] definitely showed that viscosity (i.e., boundary layer) effects have a definite effect upon the base pressure. Chapman also suggested the use of a criterion based upon a modified boundary-layer thickness to correlate data from recent tests on projectiles and missiles. Since recent experimental work on projectiles has indicated that the boundary layer definitely affects the base pressure, it was decided to investigate the effects of the boundary layer on the similar phenomena occurring in internal sonic or supersonic flow through a sudden enlargement in cross section (cf. Fig. 1). The experimental study of this type of phenomena with an internal flow apparatus has a number of distinct advantages over usual ballistics test procedures. The size of the air supply needed is greatly reduced by eliminating the need for tunnels with large enough cross sections so that wall interference, etc., will not disturb flow over the model. "Stings" and other support mechanisms can also be eliminated. The most important advantage of an internal flow apparatus is that complete static pressure and surface temperature measurements can be made not only along the entrance section to the expansion (analogous to the body of the projectile) but also in the wake region. These measurements are particularly valuable if one wants to test theoretical predictions adequately.

## Comparison of Internal and External Flow

There are a number of factors that prevent the direct comparison of base pressure phenomena present in internal two-dimensional flow with similar phenomena present in external axially symmetrical or two-dimensional flow. The first factor is that there are wall shear stresses acting on the wake and the reattached boundary layer in the internal flow apparatus, and there are no equivalent shear stresses in the external flow case. The second, and possibly more important, factor is that internal flow upstream of the sudden expansion is invariably accompanied by severe pressure gradients if the approach section has parallel walls, while the pressure gradient along the cylindrical portion of a projectile is usually very small. The third factor is that the jet boundary will be intersected by "Mach lines" (expansion waves) originating at the opposite corner, which is not the case in external two-dimensional flow (cf. Fig. 1). The point of intersection of the first expansion wave with the jet boundary represents the maximum expansion ratio possible for a given initial Mach Number and base pressure ratio for which the jet is not intersected by Mach lines from the opposite corner. This point can be calculated.

Fig. 2 shows the expansion lines (characteristics of the first set) originating at one corner being intersected by the first expansion line (characteristic of

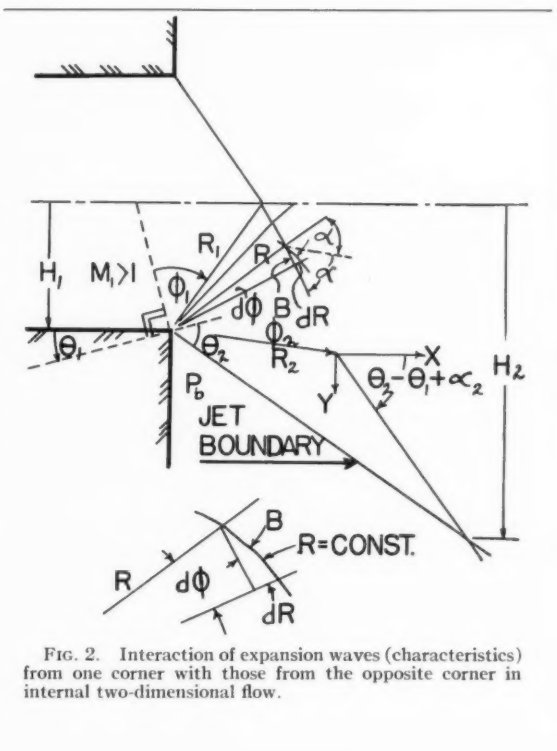


FIG. 2. Interaction of expansion waves (characteristics) from one corner with those from the opposite corner in internal two-dimensional flow.

the second set) from the opposite corner. The problem is to determine this intersecting characteristic. After this characteristic intersects the last expansion line from the corner, it is a straight line until it meets the jet boundary. The flow between the corner and this first intersecting characteristic can be described by the Prandtl-Meyer solution. The system of coordinates for the present solution is rotated through the same entrance angle $\theta_1$ sonic flow would turn through in order to reach the initial Mach Number $M_1$ under consideration. $\phi_1$ is the direction of the first expansion line, and its length is $R_1$. Now consider the conditions at the point $R$. The angle between the characteristic of the first set (and also of the second set) and the streamline is $\alpha$, the Mach angle, and is equal to arc sin $1/M$.

Calling the angle between an $r$ = constant line and the first characteristic of the second set $B$, the following relation is obtained:

$$\tan B = \frac{-dR}{Rd\phi} = \tan\left(2\alpha - \frac{\pi}{2}\right) = \frac{1 - \tan^2 \alpha}{2 \tan \alpha} \quad (1)$$

The relationship between $M$ and the angle $\phi$ is determined by the Prandtl-Meyer solution,

$$M^2 = (\gamma + 1 - 2\cos^2 \epsilon)/(\gamma - 1)\cos^2 \epsilon$$

where $\epsilon = \phi \sqrt{(\gamma - 1)/(\gamma + 1)}$.

With algebraic simplification Eq. (1) becomes

$$\frac{dR}{R} = \frac{1}{2}\tan \epsilon \, d\epsilon - \frac{\gamma - 1}{\gamma + 1}\operatorname{ctn} \epsilon \, d\epsilon \quad (2)$$

and, when integrated between $\epsilon_1$ to $\epsilon_2$ and $R_1$ to $R_2$, this becomes (for $\gamma = 1.4$)

$$R_1/R_2 = (\sin \epsilon_2/\sin \epsilon_1)^{1/3}(\cos \epsilon_2/\cos \epsilon_1)^{1/} \quad (3)$$

$R_1$ is related to $H_1$ in the following way:

$$H_1 = R_1 \cos(\phi_1 - \theta_1)$$

$\phi_2$ and thus $\epsilon_2$ depend on the base pressure ratio, and $H_2$ can be found from the intersection of the expansion line with the jet. The expansion line is straight after passing through the expansion lines from the opposite corner, and its slope in our system of coordinates will be $(\theta_2 - \theta_1 + \alpha_2)$. $\theta_2$ is the angle the flow would have turned through if it had started from sonic velocity, and $\alpha_2$ is the Mach angle corresponding to the state determined by the base pressure ratio.

If the entrance Mach Number is unity, no area of the jet will be unaffected by the expansion waves from the opposite corner. This feature alone makes the case of sonic flow through a sudden expansion unique. The factors listed indicate that the problem of internal flow is not strictly analogous to the corresponding problem in external flow, but there are enough overall similarities to make the study of internal flow valuable.

## Analytical Treatment

The behavior of compressible fluid flow depends greatly upon the type of flow—that is, whether it is subsonic, sonic, or supersonic. The corresponding flow equations will be elliptic, parabolic, or hyperbolic, respectively. The type of equation is important since it determines how the boundary conditions enter into the problem. In the case of the parabolic and hyperbolic type, the problem is an initial value type, and disturbances cannot travel upstream. In the case of the elliptic type, the problem is a boundary value type, and downstream conditions will affect the flow upstream.

In an internal flow problem such as the flow of a compressible fluid past a sudden increase in cross-sectional area, there could be more than one type of flow present. For instance, the flow in the smaller (entrance) section could be sonic or supersonic and the flow in the larger section subsonic or supersonic. In the case where the flow in the larger section is subsonic, the flow is determined upstream as far as the entrance if flow at the entrance is sonic or supersonic and past the entrance if the flow there is subsonic. A more interesting case arises when the flow in the larger section is supersonic and the flow in the entrance section is sonic or supersonic. In this case, the pressure in the corner is not determined by the downstream conditions but rather by the upstream conditions. The purpose of this investigation is to consider how changes in the upstream conditions affect the pressure in the corner.

In any case, whether the flow in the entrance section is sonic or supersonic, there will be a region, because of viscous effects, in the neighborhood of the upstream surface where the flow is subsonic, and, therefore, the flow conditions (such as boundary-layer type, momentum thickness) in this region will then be interrelated with the conditions in the corner. These facts cannot be considered in a one-dimensional analysis, since the one-dimensional analysis (which requires that the momentum theorem be evaluated at the boundaries) does not go into the details of the internal mechanism of the flow. A two-dimensional theoretical treatment would make it possible to elaborate further on the details of the flow, but it still would not supply adequate means of solving the problem of sudden expansions even when the flow is completely hyperbolic in nature, since it is necessary to know the base pressure *before* the two-dimensional flow pattern can be constructed.

A one-dimensional analysis will however be useful in establishing generally the range of physically possible solutions. If the one-dimensional energy, continuity, and momentum relations are applied between the entrance to the expansion and some distance downstream where one-dimensional conditions might be approximately fulfilled, the following relations can be derived.

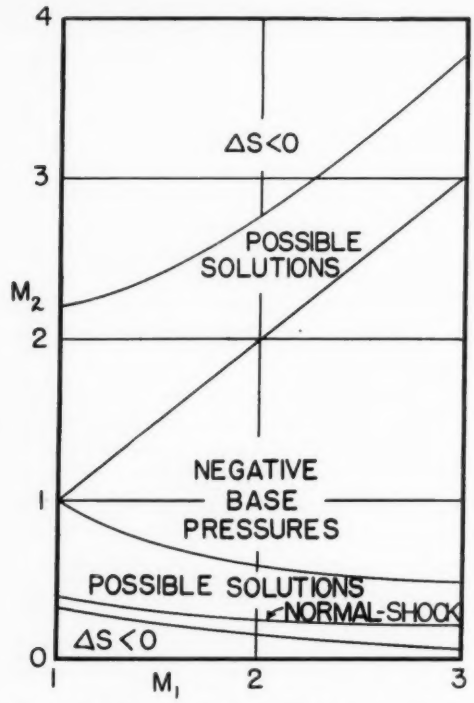


FIG. 3. Possible solution for internal expansion—2 to 1 area ratio (result of one-dimensional analysis).

*Momentum:*

$$\frac{P_b}{P_1} = \frac{(1 + \gamma M_2^2)P_2/P_1 - (1 + \gamma M_1^2)A_2/A_1}{1 - A_1/A_2} \tag{4}$$

*Energy and continuity:*

$$\frac{P_1 A_1}{P_2 A_2} = \frac{M_2}{M_1}\left\{\frac{1 + [(\gamma - 1)/2]M_2^2}{1 + [(\gamma - 1)/2]M_1^2}\right\}^{1/2} \tag{5}$$

*Energy and continuity:*

$$\frac{P_{02}}{P_{01}} = \frac{A_1 M_1}{A_2 M_2}\left(\frac{1 + [(\gamma - 1)/2]M_2^2}{1 + [(\gamma - 1)/2]M_1^2}\right)^{(\gamma + 1)/2(\gamma - 1)} \tag{6}$$

Combining Eqs. (4) and (5), $P_2/P_1$ may be eliminated, and values of $M_1$ and $M_2$ which allow positive base pressure ratios can be determined for the particular expansion ratio $A_2/A_1$ in question. A further physical limitation is that the stagnation pressure ratio given by Eq. (6) should be less than 1. The two foregoing physical limitations give both an upper and lower limit for the Mach Number $M_2$ in the expanded section when the entrance Mach Number $M_1$ is specified. A further limitation results from the specification that a normal shock is the strongest that can occur at the entrance to the enlargement. The latter restriction gives a lower limit for $M_2$ which lies within the limits defined by entropy limitations and thus defines the least value for $M_2$ for a given value of $M_1$. The limitations are a function of the area ratio, and Fig. 3 is a representation of the possible solutions for a 2 to 1 expansion ratio.

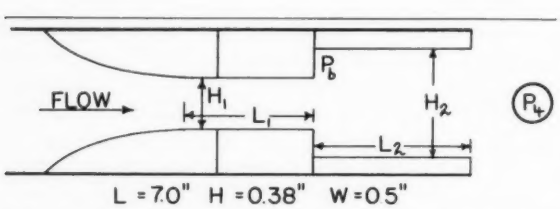


FIG. 4. Schematic diagram of the two-dimensional test section.

## Experimental Procedure

A two-dimensional flow channel consisting of a convergent section, a straight section, and an enlarged section connected in series (cf. Fig. 4) was constructed. The width of the flow channel was $^1/_2$ in., and the height ($H_1$) at the throat was 0.381 in. These two values remained constant throughout the tests. The maximum amount of airflow available was $^1/_2$ lb. per sec. at 110 lbs. per sq.in. gage stagnation pressure. The expansion ratio $H_2/H_1$ (throat area to expanded section area) was varied from 1.76 to 3.54 by varying the height $H_2$ of the expanded section. The flow reached *sonic* velocity at the end of the variable-length throat section ($L_1$) and expanded suddenly into the enlarged section. The boundary layer in the throat was varied by changing the mass rate, total pressure, and the length of the throat, allowing Reynolds Numbers at the throat based on the approach length to be varied from 1 to 15 times $10^6$.

The behavior of the flow in the throat section was determined by wall pressure measurements, as well as by measured temperature recovery factors, and the base pressure ratio by measuring the pressure in the corner and at the entrance to the expansion. The test procedure was to vary the stagnation pressure over the available range for the various combinations of throat section lengths and enlarged section heights.

## Experimental Results

As shown in Fig. 4, the apparatus actually consists of two sudden enlargements in series. The conditions at the first (the sonic throat) are explicitly controlled, while those at the second (the flow from the expanded section into the surrounding atmosphere) are only implicitly controlled. The expansion ratio for the second expansion is essentially infinite, and its base pressure must be nearly atmospheric—i.e., $P_4$. If the pressure in the expanded section were lower than the atmospheric pressure $P_4$, the boundary layer in this section would be expected to thicken considerably and reverse flow might be expected. These conditions are approached as the overall pressure ratio $P_4/P_0$ is increased (i.e., the reservoir pressure $P_0$ is reduced). Fig. 4, a

plot of base pressure ratio $P_b/P_1$† vs. the overall pressure ratio $P_4/P_0$ for constant approach section length ($L_1/H_1 = 11.81$) with the expansion ratio as a parameter, shows the effect of raising the overall pressure ratio $P_4/P_0$. The base pressure ratio $P_b/P_1$ remains constant until a definite value of $P_4/P_0$ (dependent on the expansion ratio) is reached and the base pressure ratio in one corner starts to rise. It was noted that, as the reservoir pressure was lowered still further, the pitch of the sound emitted by the jet stream suddenly changed, and it was apparent that the jet in the expanded section was completely separated from one wall of the expanded section. This would indicate that the flow was symmetrical about the axis until an upper limit of $P_4/P_0$ was reached; and then, as $P_0$ was further decreased, the base pressures in the two corners deviated as the jet in the expanded section became more unsymmetrical and finally separated completely from one wall. Because the mechanical design of the apparatus permitted measurement of the pressure in only one corner, the same type of phenomena was investigated by means of the hydraulic analogy, and these results verified the existence of the unsymmetrical jet above definite values of $P_4/P_0$. The upper limit of $P_4/P_0$ for the existence of a symmetrical jet was a function of the area ratio; the larger the expansion ratio, the lower the critical value of $P_4/P_0$ (i.e., the higher the critical value of $P_0$ below which the jet would become unsymmetrical). The remainder of the discussion will be restricted to the case where the jet was symmetrical or, in other words, cases where the base pressure was not affected by conditions in the expanded section. Thus, only the flat portion of the curves in Fig. 5 is considered. This restriction limits the range of variation of the flow variables such as Reynolds Number, etc.

Fig. 5 shows that at a given area ratio and approach length ($L_1$) the base pressure ratio remained constant even as the Reynolds Number in the approach section was varied by changing the reservoir pressure $P_0$. Plots obtained similar to Fig. 5 were shifted in the direction of higher base pressure ratios for smaller values of throat length. In Fig. 6 the base pressure ratio (symmetrical case) is plotted against the reciprocal of the expansion ratio $H_2/H_1$ with the approach length ratio $L_1/H_1$ as a parameter.

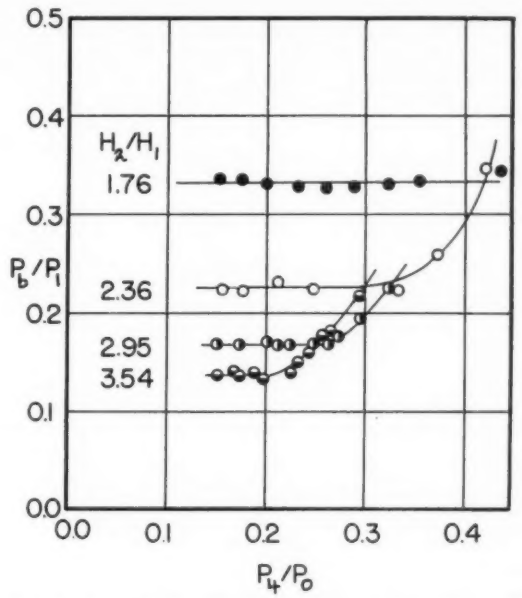


FIG. 5. Base pressure ratio $P_b/P_1$ vs. overall pressure ratio $P_4/P_0$ for $L_1/H_1 = 11.81$.

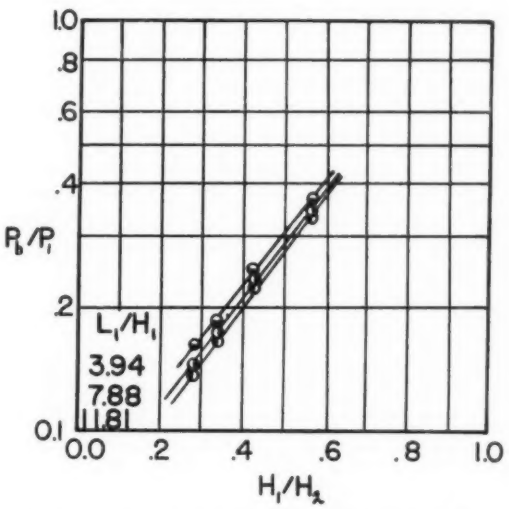


FIG. 6. Effect of area ratio on base pressure ratio.

## ANALYSIS OF RESULTS

Theoretical work by Crocco[6] and experimental work by others[4,5] indicate that projectile base pressures are definitely related to the upstream boundary-layer type, thickness, and the location of the transition point. It would seem reasonable that the data obtained for the base pressures in internal flow could be correlated in a similar manner. Referring to Fig. 5, it is obvious that the Reynolds Number varies considerably over the flat or constant base pressure ratio portion of the curves. In fact, the Reynolds Number varies from $4.6 \times 10^6$ at the right-hand end of the curve for the 1.76 expansion ratio to $10.6 \times 10^6$ at the left-hand end. The theories of Crocco and the available data on base pressures indicate that, if the boundary layer upstream of the expansion is not turbulent, the base pressure changes rapidly with Reynolds Number. The present data on base pressures for internal expansions would

† For the tests reported, the entrance Mach Number was equal to unity, and $P_1$ can be replaced by $P^*$, the critical pressure. Since isentropic flow is assumed in the core flow in the throat section, $P_4/P_0$ is equal to $P_4/P_1$ times a constant, the critical pressure ratio.

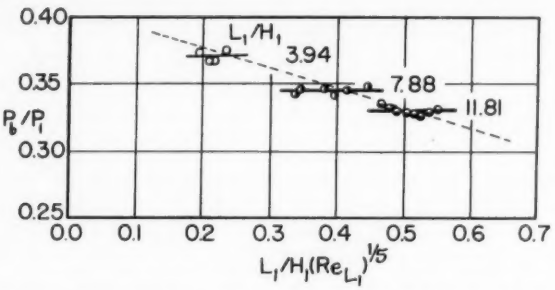


FIG. 7. Boundary-layer thickness correlation of data for $H_2/H_1 = 1.76$.

indicate that the transition of the boundary layer from laminar to turbulent has occurred far upstream of the expansion. In fact, temperature recovery factors measured in the parallel throat section ranged from 0.88 to 0.89.

Since all available evidence indicated that the boundary layer upstream of the expansion was turbulent, Chapman's modified boundary-layer thickness ratio seemed to be a reasonable parameter for correlating the data. Chapman reasoned that the thickness of the boundary layer just upstream of the corner determines the base pressure for projectiles and used a parameter that was the slenderness ratio (length to diameter of projectile) divided by the Reynolds Number (based on length) to the one-fifth power (for turbulent boundary layers) to correlate his test results. If the present test results are put in this form using $L_1/H_1$ as the slenderness ratio and $L_1$ as the length for evaluating the Reynolds Number at the sonic throat, a result similar to Fig. 7 is obtained for each expansion ratio ($H_2/H_1$). Chapman drew a curve similar to the dotted line in Fig. 7 through his data. This dotted line indicates that, as a first approximation, this method of correlation is applicable to internal flow results. However, it would seem that there is some justification for drawing separate curves through the data for each value of $L_1/H_1$ as shown by the solid lines in Fig. 7. Similar curves were obtained for three other expansion ratios, but these did not coincide with Fig. 7 unless a factor was included which took into account the expansion ratio, as well as the approach length ratio. The following expression was obtained which expresses all the results as a function of the expansion ratio ($H_2/H_1$) and the approach length ratio ($L_1/H_1$) within the accuracy of the data (cf. Fig. 6):

$$\frac{P_b}{P_1} = \left(0.734 + \frac{0.55}{L_1/H_1}\right) \exp 1.37 \left(\frac{H_1}{H_2}\right) \qquad (7)$$

The following restrictions apply to Eq. (7):

(1) $W/H_1 = 1.3$ (the effect of the side walls on the two-dimensional aspects of the problem is not yet known).

(2) $L_2/H_1 = 18.37$.

(3) $P_4/P_0 \leq 0.05 + 0.1(H_2/H_1)$†.

(4) Transition point far upstream of the sudden expansion.

Examination of Eq. (7) and Fig. 7 indicates that the boundary-layer thickness ratio $L_1/H_1\ (Re_{L_1})^{1/5}$ is not sufficient for correlating the data, since the ratios $L_1/H_1$ and $H_2/H_1$ are also necessary parameters. These results, however, do not mean that the base pressure ratio in internal flow is independent of boundary-layer thickness. The turbulent boundary-layer thickness is only directly proportional to the one-fifth power of the Reynolds Number in the case of incompressible flow with no pressure gradients. If there were no heat transfer, the fifth-power law might serve as an approximation even if the flow were high speed and compressible in the absence of pressure gradients. (These conditions are undoubtedly approximately satisfied along the cylinder of a projectile.) The essential difference between the internal and external flow is that in internal flow the growth of the boundary-layer thickness has a much more pronounced effect on the pressure gradient. In fact, the boundary-layer growth and the pressure gradient in the constant-area approach section are closely interrelated by continuity considerations. One must conclude that this interrelationship, together with the related shear stresses in the upstream section, acts in such a manner that the base pressure ratio is essentially constant in the range tested.

A simplified "jet-pump" type of theory can be devised to explain qualitatively how the base pressure ratio depends on expansion ratio for a particular upstream geometrical and flow condition. The concept presented differs considerably from that presented by Hoerner.[7] Hoerner considers the boundary layer as an insulating layer that reduces the effectiveness of the jet as a pump, while the writer considers it as a source of fluid for the corner. This is the essential difference between his concept and the proposed concept. The base corner is thought of as a sump with two supplies of mass. The first is the boundary layer flowing around the corner and will be essentially constant if upstream conditions are constant. The second source is the backflow in the boundary layer along the wall of the expanded section. This backflow occurs because of the pressure difference across the shock wave originating where the jet strikes the wall. This is schematically shown in Fig. 8. The amount of this flow will depend on the strength of the shock. Mass is removed from the sump by the "ejector action" of the jet and will, among other factors, be proportional to the exposed area. Consider the sonic expansion pictured in Fig. 9, and let the line A–B represent the wall for the case of a finite expansion ratio. The expansion ratio is now increased to that represented by A′–B′. Since the slope of any sonic jet is greatest and is changing most rapidly

† This restriction limits the values to the flat portion of the base pressure ratio vs. $P_4/P_0$ curves (cf. Fig. 5).

just past the entrance to the expansion, the resulting shock at B′ will be considerably weaker than that at B and less backflow will occur. The jet surface will increase simultaneously, and the net result will be that more fluid will be pumped out in comparison to the influx. Thus, the pressure in the sump will decrease until a point of equilibrium is reached. If the original area ratio were that depicted by C–D, an increase in area ratio to C′–D′ would also have caused a weaker shock at D′ to occur, but, since the jet slope is smaller in this region, the change in backflow would have been less than for the expansion change to A′–B′ from A–B. This indicates that, for the change of expansion from C–D to C′–D′, the decrease in base pressure would be less than for the change from A–B to A′–B′. The two results of this explanation are: (a) As area ratio increases for given upstream conditions, the base pressure will decrease; and (b) the change in base pressure for a given change in area ratio is much greater at small area ratios than at large area ratios. The first of these conclusions is confirmed by the experimental results presented in Eq. (7) and Fig. 6. If Eq. (7) is differentiated with respect to $H_2/H_1$, the following result is obtained:

$$\frac{d(P_b/P_1)}{d(H_2/H_1)} = -\left(0.73 + \frac{0.55}{L_1/H_1}\right)\frac{1.37}{(H_2/H_1)^2}\exp 1.37\left(\frac{H_1}{H_2}\right) \tag{8}$$

which confirms the second result. Thus, a simplified "jet-pump" concept can qualitatively predict the effect of the expansion ratio on the base pressure ratio for internal sonic flow.

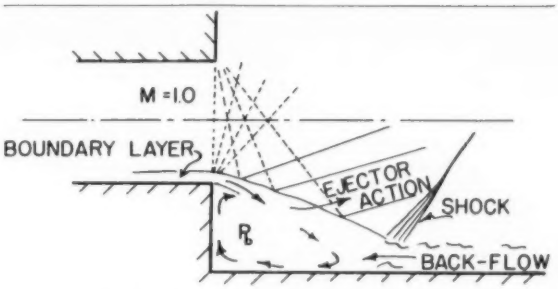


FIG. 8. "Jet-pump" action in two-dimensional sudden enlargements.

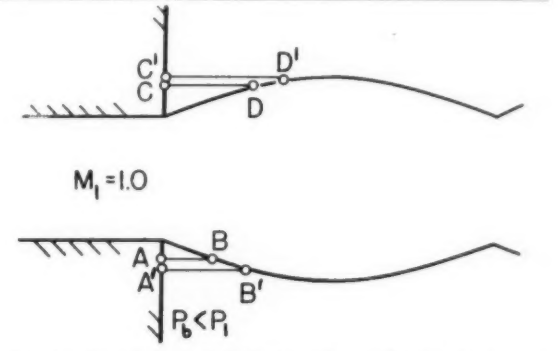


FIG. 9. Interaction of sonic jet with walls for finite two-dimensional sudden enlargements.

## CONCLUSIONS

The study of sonic flow past a sudden increase in cross-sectional area reveals that:

(1) The mechanism of internal and external flow is principally the same, and base pressure phenomena in external flow can be studied relatively easily by experiments with internal flow.

(2) The essential problem is the determination of the base pressure when the flow in the enlarged section is supersonic.

(3) The boundary layer upstream of the sudden expansion influences the base pressure ratio for a given expansion ratio.

(4) An approximate correlation of data for any given expansion ratio can be established in the same manner as in external flow by plotting the dimensionless base pressure coefficient vs. a function of a modified boundary-layer thickness at the entrance.

(5) A more accurate analysis of data indicates such a correlation involving the modified boundary-layer thickness does not account for the systematic deviation from a single curve (cf. Fig. 7). These deviations are apparently due to changes in the boundary-layer configuration caused by the presence of pressure gradients in the entrance section.

(6) A modified "jet-pump" theory can be devised which explains qualitatively the effect of area ratio on the base pressure ratio.

As a result of this study it is thought that future work along the following lines would be profitable:

(1) Extend two-dimensional studies to include supersonic flow at entrance.

(2) Extend both sonic and supersonic two-dimensional studies to different width ratios ($W/H_1$) in order to study the effect of secondary flow in side wall boundary layer.

(3) Extend studies to include the effect of length ratio ($L_2/H_1$) of the downstream section on jet symmetry.

(4) Extend the concept of internal sudden expansions to internal axially symmetric flow. This should have profound effects upon the symmetry of the resultant jet at high $P_4/P_0$ ratios, since the two corners now separated will be interconnected in the axially symmetric case.

(5) Extend experimental work to cases where a laminar boundary layer is present upstream of the expansion.

(*Concluded on next page*)

REFERENCES

[1] Borda, J. G., Memoire Academy Royal Sciences, p. 592, Paris, 1766.

[2] Nusselt, W., *Der Stossverlust an Plötzlichen Erweiterungen in Rohen bein Durchfluss von Gäsen und Dampfen*, Zeitung für Vereininger Deutches Ingenieurs, Bd. 73, pp. 763–764, 1929.

[3] Nusselt, W., *Der Druck im Ringquerschnitt von Rohen mit Plötzlicher Erweiterung bein Durchfluss von Luft mit Hoher Geschwindigkeit*, Forschung auf dem Gebiete des Ingenieurwessens, Ausgabe B, Bd. II, Heft 5, pp. 250–255, September, 1940.

[4] Chapman, D. R., *An Analysis of Base Pressure at Supersonic Velocities and Comparison with Experiment*, NACA TN No. 2137, July, 1950.

[5] Kurzweg, H. H., *Interrelationship Between Boundary Layer and Base Pressure*, Journal of the Aeronautical Sciences, Vol. 18, No. 11, pp. 743–748, November, 1951.

[6] Crocco, L., and Lees, Lester, *A Mixing Theory for the Interaction Between Dissipative Flows and Nearly Isentropic Streams*, Journal of the Aeronautical Sciences, Vol. 19, No. 10, pp. 649–676, October, 1952.

[7] Hoerner, S. F., *Base Drag and Thick Trailing Edges*, Journal of the Aeronautical Sciences, Vol. 17, No. 10, pp. 622–628, October, 1950.


# Turbulence in Supersonic Flow

(*Concluded from page 674*)


REFERENCES

[1] Lagerstrom, P. A., Cole, J. D., and Trilling, L., *Problems in the Theory of the Viscous Compressible Fluids*, Cal. Tech. Contract Report ONR Contract N6onr Task Order VIII, 1949.

[2] Ribner, H. S., *Convection of a Pattern of Vorticity Through a Shock Wave*, NACA TN No. 2864, 1953.

[3] Moore, F. K., *Unsteady Interaction of a Shock Wave with a Plane Disturbance*, NACA TN No. 2879, 1953.

[4] Lighthill, M. J., *On Sound Generated Aerodynamically*, Proc. Roy. Soc. A, Vol. 211, p. 564, 1952.

[5] Chandrasekhar, S., *The Fluctuations of Density in Isotropic Turbulence*, Proc. Roy. Soc. A, Vol. 210, p. 18, 1951.

[6] Moyal, J. E., *The Spectra of Turbulence in a Compressible Fluid, Eddy Turbulence and Random Noise*, Proc. Camb. Phil. Soc., Vol. 48, p. 329, 1952.

[7] Lin, C. C., *On Taylor's Hypothesis and the Acceleration Terms in the Navier-Stokes Equations*, Quart. Appl. Math., Vol. 10, No. 4, p. 295, 1953.

[8] Kovásznay, L. S. G., and Tornmarck, S. I. A., *Heat Loss of Hot-Wires in Supersonic Flow*, Bumblebee Rep. No. 127, The Johns Hopkins University, 1950.

[9] Kovásznay, L. S. G., *The Hot-Wire Anemometer in Supersonic Flow*, Journal of the Aeronautical Sciences, Vol. 17, No. 9, p. 565, 1950.

[10] Lowell, H. H., *Design and Applications of Hot-Wire Anemometers for Steady State Measurements at Transonic and Supersonic Airspeeds*, NACA TN No. 2117, 1950.

[11] Kovásznay, L. S. G., *Development of Turbulence Measuring Equipment*, NACA TN No. 2839, 1953.

[12] Kovásznay, L. S. G., *Turbulence Measurements, Section F, Volume VII, High Speed Aerodynamics and Jet Propulsion Series*, Princeton University Press (in press).

[13] Kovásznay, L. S. G., Uberoi, M. S., and Corrsin, S. *The Transformation Between One and Three Dimensional Power Spectra for an Isotropic Scalar Fluctuation Field*, Phys. Rev., Vol. 76, No. 8, p. 1263, 1949.

[14] Klebanoff, P. S., and Diehl, Z. W., *Some Features of Artificially Thickened Fully Developed Turbulent Boundary Layer with Zero Pressure Gradient*, NACA TN No. 2475, 1951.

[15] Proudman, I., *The Generation of Noise by Isotropic Turbulence*, Proc. Roy. Soc. A., Vol. 214, p. 119, 1952.



**Suggestion for Binding**

**Issues of the Journal of the Aeronautical Sciences**

Arrangements have been made so that our readers may have their issues of the JOURNAL bound carefully and economically in our authorized binding. Simply write for details to:

**AIRE**

**P.O. Box 776**

**Highland Park, Illinois**

# Subsonic Compressibility Corrections for Propellers and Helicopter Rotors

E. V. LAITONE* AND LAWRENCE TALBOT†
*University of California at Berkeley*

SUMMARY

Through the application of linearized theory a compressibility correction is obtained which gives the thrust or torque coefficient in subsonic flow, for a propeller or a helicopter rotor, directly from the incompressible flow values.

The blade element theory is applied to subsonic flow by introducing the linearized compressibility correction, while the first-order compressibility effect on the axial inflow is obtained from the simple momentum theory. The subsonic compressibility correction for the lightly loaded propeller is found to be expressed in terms of the forward flight Mach Number and the Mach Number based on the rotational speed of the propeller tip. These relations are directly applicable to a helicopter rotor in vertical flight and reduce to a simpler form depending only upon the rotational Mach Number at the rotor tip. It is shown that for the helicopter rotor a satisfactory approximation, for tip Mach Numbers less than 0.8, may be obtained by using the simple Prandtl-Glauert correction with the Mach Number given by the rotational speed at the three-quarter radius.

The derived compressibility corrections are found to be in agreement with available experimental data. The limitations of the relations are analyzed by comparison with a numerical solution calculated from a more exact procedure.

A critical survey is made of other work on subsonic propeller theory. It is shown that in some cases fundamental mistakes have been made which result in considerable error in predicting the effect of compressibility.

## INTRODUCTION

AT PRESENT THERE IS no general compressibility correction for propellers or helicopter rotors. The problem seems to be too difficult even when considering the vortex theory for linearized subsonic flow. The previous investigations have been mainly on the basis of the momentum theory alone (see references 1 and 2), and practically nothing has been done on the blade element theory in subsonic flow. This is understandable since the propeller characteristics depend upon the blade shape and inflow distribution, resulting in a complicated problem having no simple solution even in the incompressible case.

However, the effect of compressibility may be closely approximated if we are only interested in the ratio of the propeller characteristics in subsonic flow as compared with those computed in detail for the same propeller by assuming incompressible flow. In this case we may easily obtain a general expression for this ratio, at least for lightly loaded propellers, since this ratio is not greatly affected by variations in the blade shape or inflow distribution. This is true because we actually compare the effect of compressibility on each section of the blade, element by element, and integrate the effect of the change in radius in order to get the principal effect of compressibility on the ratio itself. The influence of compressibility on the inflow distribution is only a higher order effect that may be neglected, since the axial inflow itself only produces a second-order effect that may be neglected for lightly loaded propellers.

The general compressibility correction, in the form of a ratio of the values in subsonic flow to the corresponding values from the incompressible solution, will be obtained by assuming the constant inflow given by the momentum theory for compressible flow. Then it will be shown that even the constant inflow produces only a second-order effect that may be neglected for lightly loaded propellers. This procedure is practically the same as introduced by Pistolesi (see pages 245 and 248 of reference 3), who assumed constant values of the inflow velocities in order to estimate the effect of small changes in the solidity of propellers in the ordinary incompressible flow solution. His results showed that the actual varying inflow velocity distribution had a negligible effect in predicting the change or ratio of the propeller characteristics, even with 50 per cent changes in the solidity.

In essentially the same way, assuming constant inflow, the ratio of the subsonic propeller thrust and torque, in relation to the incompressible value, will be evaluated by using the two-dimensional Prandtl-Glauert rule. The ratios found will be restricted by the limitations of linearized subsonic flow theory in not being able to predict the critical Mach Number where the lift of the blade element drops off from its linear relation. This effect can only be determined by experiment, although as a rule, for thin blades, it can be assumed to occur when the propeller tip helical Mach Number exceeds 0.8.

### LIST OF SYMBOLS

*Airflow Symbols*

| | |
|---|---|
| $a$ | $= \sqrt{\gamma p/\rho}$ = local velocity of sound, ft. per sec. |
| $p$ | = local static pressure, lbs. per sq.ft. |
| $\rho$ | = local density, lb. sec.$^2$/ft.$^4$ |
| $\gamma$ | = 1.4 = specific heat ratio of air |

Presented at the Aerodynamics Session, Twenty-First Annual Meeting, IAS, New York, January 26–29, 1953.

* Associate Professor of Mechanical Engineering.
† Assistant Professor of Mechanical Engineering.

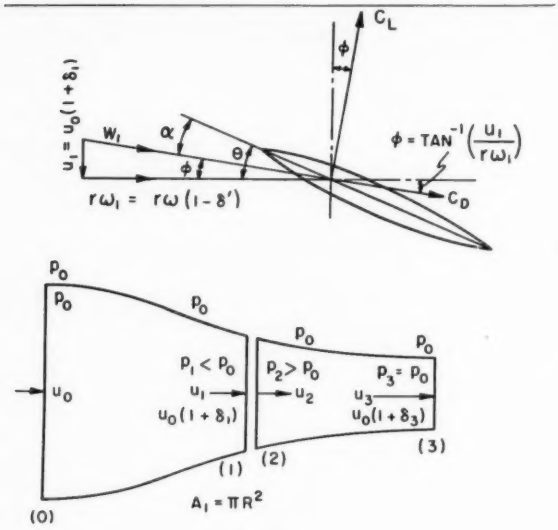


FIG. 1.

$q_0$ = $\rho_0 u_0^2/2$ = free-stream dynamic pressure, lbs. per sq.ft.
$u_0$ = axial advance velocity of propeller relative to free stream, ft. per sec.
$W_1$ = resultant local velocity relative to the propeller blade element, ft. per sec.
$\omega$ = propeller angular velocity, rad. per sec.
$M$ = $u/a$ = local axial-flow Mach Number
$M_R$ = $R\omega/a_0$ = rotational Mach Number of propeller tip
$\lambda$ = $u_0/R\omega = M_0/M_R$ = propeller tip speed ratio
$\lambda_1$ = $u_1/R\omega_1 = \lambda[(1+\delta_1)/(1-\delta')]$ = actual rate of propeller tip advance relative to air
$1+\delta$ = $u/u_0$ = axial interference velocity factor due to induced axial inflow
$1-\delta'$ = $\omega_1/\omega$ = rotational interference factor due to slipstream rotation

***Subscript Symbols (See Fig. 1)***

0 = free-stream conditions far ahead of the propeller
1 = local conditions induced at the propeller
2 = local conditions immediately behind propeller
3 = slipstream conditions an infinite distance downstream where static pressure is again free stream

***Propeller Symbols***

$A$ = $\pi R^2$ = circular disc area swept by the propeller blades, sq.ft.
$B$ = number of blades
$c$ = blade-section chord, ft.
$R$ = blade radius, ft.
$r$ = radial distance to blade section, ft.
$\theta$ = blade-section pitch angle, measured from plane of rotation to zero lift chord line, rad.
$\alpha$ = $(\theta - \phi)$ = angle of attack of blade section measured from zero lift chord line, rad.
$\phi$ = $\tan^{-1}(u_1/r\omega_1) = \tan^{-1}(R/r)\lambda_1$ = inflow angle induced at blade section, rad.
$\eta$ = $Tu_0/P = Tu_0/\omega Q$ = propulsive efficiency
$T$ = propeller thrust, lbs.
$Q$ = propeller-shaft torque, ft.lbs.
$P$ = $\omega Q$ = propeller-shaft power, ft.lbs. per sec.
$m_1$ = $\rho_1 \pi R^2 u_1$ = assumed mass rate of flow handled by propeller disc as shown in Fig. 1
$m$ = section lift-curve slope for two-dimensional incompressible flow
$C_{D_0}$ = drag (lbs.)/$q_0 c$ = section profile drag coefficient
$C_L$ = lift (lbs.)/$q_0 c$ = $(dC_L/d\alpha)\alpha$ = section lift coefficient
$C_T$, $C_Q$ = standard NACA thrust and torque coefficients

## ANALYSIS OF LIGHTLY LOADED PROPELLERS

From Fig. 1 the general expressions for the thrust and torque of the blade element are given by

$$dT = B(1/2)\rho_1 W_1^2(C_L \cos\phi - C_D \sin\phi)c\,dr \quad (1)$$

$$dQ = B(1/2)\rho_1 W_1^2(C_L \sin\phi + C_D \cos\phi)rc\,dr \quad (2)$$

where

$$W_1^2 = u_1^2 + (r\omega_1)^2 \quad (3)$$

$$C_L = \frac{dC_L}{d\alpha}\alpha \approx \frac{m}{\sqrt{1-(W_1/a_1)^2}}(\theta - \phi) \quad (4)$$

$$\phi = \tan^{-1}(u_1/r\omega_1) \quad (5)$$

In Eq. (4) the lift coefficient has been approximated by the linearized (Prandtl-Glauert) compressibility correction for two-dimensional subsonic flow, where $m$ is the incompressible flow lift-curve slope ($2\pi$ by linearized theory) and the angle of attack $\alpha$ must remain small.

Now since $C_D << C_L$ (for Mach Numbers less than critical) and $\phi$ is small (except near the hub where the compressibility effects fortunately are negligible), we are justified in neglecting the term $C_D \sin\phi$ in Eq. (1); therefore,

$$T = \frac{B}{2}\int_0^R \rho_1[u_1^2 + (r\omega_1)^2]\frac{m(\theta-\phi)\cos\phi}{\sqrt{1-(u_1/a_1)^2-(r\omega_1/a_1)^2}}c\,dr \quad (6)$$

Even for uniform inflow Eq. (6) results in logarithmic expressions that become infinite at the lower limit for all distributions of $\theta$ except for the particular case

$$c(\theta - \phi)\cos\phi = \text{constant} \quad (7)$$

Since we are interested in a general expression for the ratio of the compressible thrust to the incompressible thrust for the same propeller, any distribution of $c$ and $\theta$ will be satisfactory as long as it is a reasonable one, and we can show that small variations in $c$ and $\theta$ have only a higher order effect upon the resulting ratio. Now, Eq. (7) is an appropriate distribution of $c$ and $\theta$, since it corresponds to a constant chord propeller twisted so as to maintain a constant angle of attack as long as $\phi$ remains small—that is,

$$\left.\begin{aligned} c &= \text{constant} \\ (\theta - \phi) &= \alpha_R = \text{constant} \\ \cos\phi &= 1 - \phi^2/2! + \ldots \approx 1 \end{aligned}\right\} \quad (8)$$

If we define the propulsive efficiency following Glauert (see pages 204 and 232, reference 3) as

$$\frac{u_0\,dT}{\omega\,dQ} = \eta = \eta_1\eta_2\eta_3 = \left(\frac{1}{1+\delta_1}\right)(1-\delta')\left[\frac{\tan\phi}{\tan(\phi+\gamma_0)}\right] \tag{9}$$

that is

$$\eta_1 = 1/(1+\delta_1) \tag{10}$$

$$\eta_2 = 1-\delta' \tag{11}$$

$$\eta_3 = \tan\phi/\tan(\phi+\gamma_0) \tag{12}$$

where

$$\tan\gamma_0 = C_D/C_L \tag{13}$$

then the constant angle of attack defined in Eq. (8) corresponds to a maximum value of $\eta_3$ or the minimum loss of thrust due to frictional drag on the propeller blades. The only approximation involved is that $\phi$ remains small, an assumption not justified near the hub. However, in this hub region the compressibility effects are negligible at ordinary forward speeds; therefore, the ratio of the compressible to the incompressible thrust is actually determined by the outboard sections of the propeller where Eq. (8) is valid. This is also the best choice for assuring the validity of Eq. (4), since the angle of attack remains a small constant along the entire blade.

Substituting Eq. (8) into Eq. (6) and integrating for the case of uniform inflow, we obtain

$$T = \frac{1}{2}\rho_1(R\omega_1)^2Rc\;m\;\frac{\alpha_R}{2}\times \left[\frac{1+M_1^2}{M_{R_1}^3}\sin^{-1}\left(\frac{M_{R_1}}{\sqrt{1-M_{R_1}^2}}\right) - \frac{\sqrt{1-M_{R_1}^2-M_1^2}}{M_{R_1}^2}\right] \tag{14}$$

where

$$M_{R_1} = \frac{R\omega_1}{a_1} = \frac{R\omega(1-\delta')}{a_0(a_1/a_0)} = \frac{M_R(1-\delta')}{a_1/a_0} \tag{15}$$

$$M_1 = \frac{u_1}{a_1} = \frac{u_0}{a_0}\,\frac{(1+\delta_1)}{a_1/a_0} = \frac{M_0(1+\delta_1)}{a_1/a_0} \tag{16}$$

For the corresponding incompressible flow case we have $\rho_0 = \rho_1$ and $a \to \infty$, so Eqs. (6) and (8) reduce to

$$T_{\text{inc.}} = \frac{1}{2}\rho_0(R\omega_1)^2Rc\;m\;\frac{\alpha_R}{3}\left[1+3\left(\frac{u_1}{R\omega_1}\right)^2\right] \tag{17}$$

Taking the ratio of the compressible thrust to the incompressible value for the same propeller, we find that, when the induced inflow velocities are the same, then the thrust increases with either Mach Number by the ratio

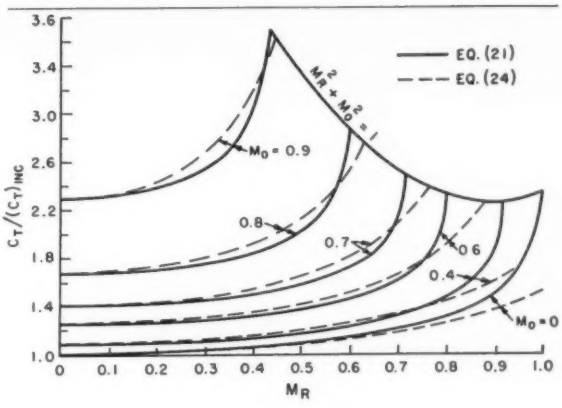


FIG. 2.

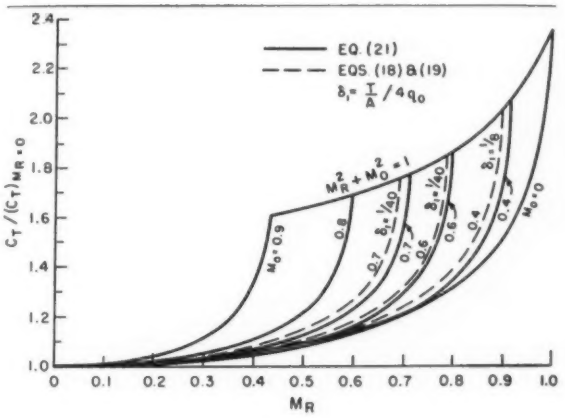


FIG. 3.

$$\frac{C_T}{C_{T_{\text{inc.}}}} = \frac{T}{T_{\text{inc.}}} = \frac{3}{2}\frac{\rho_1}{\rho_0}\times \frac{\left[\dfrac{1+M_1^2}{M_{R_1}^3}\sin^{-1}\left(\dfrac{M_{R_1}}{\sqrt{1-M_1^2}}\right) - \dfrac{\sqrt{1-M_{R_1}^2-M_1^2}}{M_{R_1}^2}\right]}{1+3(M_1^2/M_{R_1}^2)} \tag{18}$$

Later, by using the momentum theory, we shall prove that, to the first order for a lightly loaded propeller,

$$\left.\begin{aligned} \rho_1/\rho_0 &= 1 - M_0^2[(T/A)/4q_0] \\ \frac{M_1}{M_0} &= \left(1+\frac{\gamma-1}{2}M_0^2\right)\left(\frac{T/A}{4q_0}\right)+1 \\ \frac{M_{R_1}}{M_R} &= 1+\frac{\gamma-1}{2}M_0^2\left(\frac{T/A}{4q_0}\right) \end{aligned}\right\} \tag{19}$$

and

$$\delta_1 = (T/A)/4q_0; \qquad \delta' = 0 \tag{20}$$

Consequently, for lightly loaded propellers, it is seen that Eq. (18) may be written to the first order as

$$\frac{C_T}{C_{T_{\text{inc.}}}} = \frac{T}{T_{\text{inc.}}} = \frac{3}{2} \times \left[ \frac{\dfrac{1 + M_0^2}{M_R^3} \sin^{-1}\left(\dfrac{M_R}{\sqrt{1 - M_0^2}}\right) - \dfrac{\sqrt{1 - M_R^2 - M_0^2}}{M_R^2}}{1 + 3(M_0^2/M_R^2)} \right] \tag{21}$$

where

$$M_R = R\omega/a_0 \tag{22}$$

is the actual rotational Mach Number of the propeller tip, based on the free-stream speed of sound, and

$$M_0 = u_0/a_0 \tag{23}$$

is the usual forward flight or free-stream Mach Number.

Fig. 2 is a plot of Eq. (21) for constant values of $M_0$, while Fig. 3 shows the ratio, obtained for constant values of $M_0$, of the thrust at varying values of $M_R$ to that when $M_R = 0$. In Fig. 2 the dotted lines shown for comparison are those given by the ordinary Prandtl-Glauert rule using the helical Mach Number occurring at the three-quarter radius so that

$$C_T/C_{T_{\text{inc.}}} = 1/\sqrt{1 - M_{3/4}^2} \tag{24}$$

where

$$M_{3/4}^2 = M_0^2 + [(3/4)M_R]^2 \tag{25}$$

It is evident from Fig. 2 that the Prandtl-Glauert rule cannot be applied directly to a propeller by the simple procedure of using the helical Mach Number at some fixed per cent of the blade radius, especially for larger values of either Mach Number. However, when $M_R = 0$, Eq. (21) exactly reduces to the simple Prandtl-Glauert rule as would be expected,

$$\left(\frac{C_T}{C_{T_{\text{inc.}}}}\right)_{M_R=0} = \frac{(1 + M_0^2)(1 - M_0^2)^{-1/2} - (1 - M_0^2)^{1/2}}{2M_0^2} = \frac{1}{\sqrt{1 - M_0^2}} \tag{21a}$$

Also shown in Fig. 3 are the values obtained from combining Eqs. (18), (19), and (20) for various values of the disc loading. It is obvious that Eq. (21) is a satisfactory approximation, even for relatively large disc loadings as long as $M_0$ is small.

It is interesting to note that the thrust remains finite at the limiting value of unity for the helical Mach Number at the tip (shown in Figs. 2 and 3), because the infinite lift predicted by the Prandtl-Glauert rule used in Eq. (6) only occurs in the infinitesimal area at the tip itself. Actually Eqs. (4) and (6) become invalid when the so-called critical Mach Number is exceeded, since the lift decreases and the drag abruptly increases. Consequently, only Eqs. (1) and (2) are applicable when the critical helical Mach Number (approximately 0.8 for thin blades) is reached.

---

A similar analysis of the torque expressed by Eq. (2) leads to the equivalent of Eq. (6)—namely,

$$Q = \frac{B}{2} \int_0^R \rho_1[u_1^2 + (r\omega_1)^2] \left[ C_D \cos\phi + \frac{m(\theta - \phi)\sin\phi}{\sqrt{1 - \left(\dfrac{u_1}{a_1}\right)^2 - \left(\dfrac{r\omega_1}{a_1}\right)^2}} \right] cr\, dr \tag{26}$$

Then if we take $\phi$ small, as in Eq. (8), and write, in addition,

$$\sin\phi = \phi = \frac{u_1}{r\omega_1} = \lambda_1 = \lambda\left(\frac{1 + \delta_1}{1 - \delta'}\right) \tag{27}$$

we can integrate Eq. (26) for $\alpha_R = (\theta - \phi)$ a constant

$$\frac{Q}{(1/2)\rho_1(R\omega_1)^2 R\,(Rc)} = \bar{C}_{D_0}\left(\frac{1}{4} + \frac{1}{2}\lambda_1^2\right) + m\alpha_R \frac{\lambda_1}{2}\left[\frac{1 + M_1^2}{M_{R_1}^3}\sin^{-1}\frac{M_{R_1}}{\sqrt{1 - M_1^2}} - \frac{\sqrt{1 - M_{R_1}^2 - M_1^2}}{M_{R_1}^2}\right] \tag{28}$$

where

$$\bar{C}_{D_0} = \frac{\left(\dfrac{\lambda_1}{R}\right)^2 \displaystyle\int_0^R C_{D_0}\left[1 + \left(\frac{r}{R\lambda_1}\right)^2\right] r\, dr}{[(1/4) + (1/2)\lambda_1^2]} \tag{29}$$

Similarly, for the same propeller we have the incompressible flow solution,

$$\frac{Q_{\text{inc.}}}{(1/2)\rho_0(R\omega_1)^2 R^2 c} = \bar{C}_{D_0}\left(\frac{1}{4} + \frac{1}{2}\lambda_1^2\right) + m\alpha_R \frac{\lambda_1}{3}(1 + 3\lambda_1^2) \tag{30}$$

Consequently, the ratio of the compressible torque to the incompressible value, for the same conditions that govern Eq. (21)—that is, for a lightly loaded propeller—is

$$\frac{C_Q}{C_{Q_{\text{inc.}}}} = \frac{Q}{Q_{\text{inc.}}} = \frac{\bar{C}_{D_0}\left(\frac{1}{4} + \frac{1}{2}\lambda^2\right) + m\alpha_R \frac{\lambda}{2}\left[\frac{1 + M_0^2}{M_R^3}\sin^{-1}\frac{M_R}{\sqrt{1 - M_0^2}} - \frac{\sqrt{1 - M_R^2 - M_0^2}}{M_R^2}\right]}{\bar{C}_{D_0}\left(\frac{1}{4} + \frac{1}{2}\lambda^2\right) + m\alpha_R \frac{\lambda}{3}\left(1 + 3\frac{M_0^2}{M_R^2}\right)} \tag{31}$$

This ratio depends upon $\bar{C}_{D_0}$; however, if we remain below the critical Mach Number we may assume that $\bar{C}_{D_0}$ is practically constant. Therefore, we may subtract the torque due to blade friction (the $\bar{C}_{D_0}$ term) from the incompressible solution. Then we can compute the effect of compressibility on the remaining part (the induced drag torque or $C_L\phi$ term). Finally, we add the incompressible torque due to blade friction and obtain the total torque in subsonic flow. The compressibility correction for the induced drag torque is identical to Eq. (21) and is therefore also given by Figs. 2 and 3.

Since the thrust coefficient and the induced drag torque coefficient have the same ratio of increase with Mach Number, it is evident that the propulsive efficiency for a lightly loaded propeller, as defined by Eq. (9), will remain constant as the Mach Number increases to the critical value. This occurs because the part of the torque coefficient due to blade friction remains a small constant. However, when the critical Mach Number is reached, $\bar{C}_{D_0}$ abruptly increases and the propulsive efficiency decreases.

## Application to a Helicopter Rotor in Vertical Climb

The application of these results to a helicopter rotor in vertical climb is especially simple since the disc loading is so light that not only is the inflow small but $M_0$ and $u_1^2$ may be considered zero. Consequently, it is easy to analyze the effect of any arbitrary blade twist in this case.

Since $M_0 = 0$ for a helicopter rotor, Eqs. (21) and (31) for a constant angle of attack rotor become

$$\frac{C_T}{C_{T_{\text{inc.}}}} = \frac{3}{2}\left(\frac{\sin^{-1} M_R}{M_R^3} - \frac{\sqrt{1 - M_R^2}}{M_R^2}\right) \tag{32}$$

$$\frac{C_Q}{C_{Q_{\text{inc.}}}} = \frac{\frac{\bar{C}_{D_0}}{4} - m\alpha_R \frac{\lambda}{2}\left(\frac{\sin^{-1} M_R}{M_R^3} - \frac{\sqrt{1 - M_R^2}}{M_R^2}\right)}{(\bar{C}_{D_0}/4) - m\alpha_R(\lambda/3)} \tag{33}$$

These correspond to the curves $M_0 = 0$ in Figs. 2 and 3 and are replotted in Fig. 4. Of course, they may be obtained directly by integrating Eqs. (6) and (26) with $u_1^2 = 0$, $\rho_1 = \rho_0$, and $a_1 = a_0$. Now with these simplifications we can finally integrate Eqs. (6) and (26) for any arbitrary blade twist. For example, the so-called ideal blade twist defined by

$$\theta = \theta_R(R/r) \tag{34}$$

which is the only one actually giving a uniform inflow distribution (see page 68, reference 4), gives

$$(\theta - \phi) = (\theta_R - \lambda)(R/r) = \alpha_R(R/r) \tag{35}$$

Then, with $\cos\phi = 1$, Eq. (6) yields

$$C_T/C_{T_{\text{inc.}}} = 2\left[(1 - \sqrt{1 - M_R^2})/M_R^2\right] \tag{36}$$

Similarly, Eq. (26) gives

$$\frac{C_Q}{C_{Q_{\text{inc.}}}} = \frac{\frac{\bar{C}_{D_0}}{4} - m\alpha_R\lambda\left(\frac{1 - \sqrt{1 - M_R^2}}{M_R^2}\right)}{(\bar{C}_{D_0}/4) - m\alpha_R(\lambda/2)} \tag{37}$$

Fig. 4 shows that Eq. (36) agrees almost exactly with Eq. (24), the simple Prandtl-Glauert rule using the Mach Number occurring at three-quarters of the blade radius, at least for Mach Numbers less than 0.8. Eq. (36) also agrees fairly closely with Eq. (32) indicating that the effect of the blade angle distribution is slight. It is obvious that, if we substitute

$$(\theta - \phi) = [\theta - \lambda(R/r)]$$

into Eq. (6), then the compressibility correction for any blade angle distribution, even the flat blade with no twist, will fall between the two values defined by Eqs. (32) and (36). Since Eq. (36) is for the ideal blade twist, which is the only one that actually produces the uniform inflow distribution assumed in the

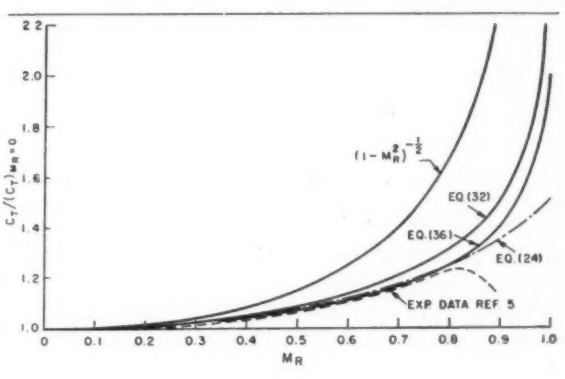


Fig. 4.

derivation, therefore it must be the most nearly correct. This indicates that Eq. (21) may slightly overestimate the effect of compressibility due to the impossibility of actually obtaining a uniform inflow distribution when the angle of attack is kept constant. However, this effect is slight, as may be shown by the fact that the Taylor series expansions of Eqs. (32) and (36) are nearly identical for the first three terms.

Since the compressibility correction is limited by the critical Mach Number of 0.8, or less, it is evident from Fig. 4 that a satisfactory approximation for any helicopter rotor in vertical climb is given by the simple Prandtl-Glauert rule using three-quarters of the tip Mach Number. A comparison with experimental data is also shown in Fig. 4. The dotted line is calculated from the tables given in reference 5 for a two-bladed tapered propeller having a 6 per cent profile thickness, a 2-ft. diameter, and a solidity of 0.038. The tests were made in a wind tunnel at forward speeds of 90 ft. per sec. or less, corresponding closely to $M_0 = 0$. The experimental data prove that the theoretical results are valid as long as the critical tip Mach Number of 0.8 is not exceeded.

### The Momentum Theory for Subsonic Flow

The subsonic inflow velocity distribution may be calculated by combining the blade-element theory with the general momentum theory. This is done by expressing the blade-element thrust increment as in Eq. (1) in terms of the unknown inflow velocity increments at the propeller, station (1). This is then equated to the thrust increment determined by the velocity increments far downstream at station (3). This solution is relatively straightforward for incompressible flow, since the velocity increments are easily related to one another. For example, for light loadings the velocity increments at the propeller are one-half the magnitude of those far downstream. However, in subsonic flow this simple relation is further complicated by the density variation and the increase in entropy due to any finite discontinuity or finite blade drag.

To simplify this complicated problem we can use the one-dimensional axial-momentum theory, which yields only the average inflow, considered constant across the stream tube, and essentially replaces the propeller by the so-called actuator disc. Then for the assumed stream-tube flow shown in Fig. 1 we have, with $p_0 = p_3$ (see pages 330–334 of reference 6),

$$T = m_1(u_3 - u_0) = m_1 u_0 \delta_3 \tag{38}$$

$$m_1 = A_0\rho_0 u_0 = A\rho_1 u_1 = A_2\rho_2 u_2 = A_3\rho_3 u_3 \tag{39}$$

where $A = \pi R^2$ is the propeller disc area. Since the flow is isentropic from station (0) to station (1),

$$\left(\frac{a_1}{a_0}\right)^{2/(\gamma-1)} = \frac{\rho_1}{\rho_0} = \left[1 + \frac{\gamma-1}{2} M_0^2\left(1 - \frac{u_1^2}{u_0^2}\right)\right]^{1/(\gamma-1)}$$

$$= \left[1 - \frac{\gamma-1}{2} M_0^2(2\delta_1 + \delta_1^2)\right]^{1/(\gamma-1)} \tag{40}$$

Now the only known area in the assumed stream tube shown in Fig. 1 is $A_1 = A = \pi R^2$; therefore we can evaluate the mass rate of flow from Eqs. (39) and (40) as

$$m_1 = \rho_1 u_1 A = \rho_0 u_0 A(1 + \delta_1) \times \left[1 - \frac{\gamma-1}{2} M_0^2(2\delta_1 + \delta_1^2)\right]^{1/(\gamma-1)} \tag{41}$$

In addition, the total work done by the propeller may be evaluated from the one-dimensional energy equation by assuming no heat transfer from the stream tube to the surrounding air so that

$$\frac{P}{m_1} + \frac{a_0^2}{\gamma-1} + \frac{u_0^2}{2} = \frac{a_3^2}{\gamma-1} + \frac{u_3^2}{2} \tag{42}$$

where $P$ is the total power actually supplied to the propeller so that

$$P = \omega Q = \frac{Tu_0}{\eta} = m_1\left[\frac{u_3^2 - u_0^2}{2} + \frac{a_3^2 - a_0^2}{\gamma-1}\right] = m_1\left[\frac{u_3^2 - u_0^2}{2} + \frac{\gamma p_0}{\gamma-1}\left(\frac{1}{\rho_3} - \frac{1}{\rho_0}\right)\right] \tag{43}$$

So far, all the relations derived are exact for the assumed conditions of an adiabatic process with uniform inflow as depicted in Fig. 1. Now a difficult problem arises in determining the relation between $\delta_1$ and $\delta_3$. In reference 1 Krzywoblocki based his numerical calculations on the assumption that $\rho_2 = \rho_1$, arguing that the pressure jump through the propeller disc happens too quickly for the density to change. However, this is an impossible assumption for a perfect gas, since any pressure discontinuity in an adiabatic flow must be accompanied by a corresponding density discontinuity. On the other hand, in reference 2 Vogeley based his calculations on the assumption that $\rho_3 = \rho_0$, the so-called isentropic propeller with no blade friction. That is, since the entropy change is given by

$$S_3 - S_1 = S_3 - S_0 = C_v \ln\left\{\left(\frac{p_3}{p_0}\right)\left(\frac{\rho_0}{\rho_3}\right)^{\gamma}\right\} = \gamma C_v \ln\left(\frac{\rho_0}{\rho_3}\right) > 0 \tag{44}$$

therefore, if $\rho_0 = \rho_3$, the process becomes isentropic and Eq. (43) reduces to exactly the same expressions obtained for incompressible flow,

$$P_I = \omega Q_I = \frac{Tu_0}{\eta_1} = \frac{1}{2} m_1\left(u_3^2 - u_0^2\right) = Tu_0\left(1 + \frac{\delta_3}{2}\right) \tag{45}$$

However, this is incompatible with the assumed thin discontinuity disc having $A_2 = A_1$, since the energy equation and the impulse-momentum equation can be combined to prove there must be an entropy increase with $\rho_3 < \rho_0$ if a finite discontinuity exists between $p_2$ and $p_1$. Consequently, if one assumes $\rho_3 = \rho_0$, as in the calculations of reference 2, then one cannot tacitly

assume $A_1 = A_2$ and the existence of a thin actuator disc. However, a valid first-order approximation can be obtained by using the exact incompressible flow relations as the first step of an iterative process. Since Eq. (45) is exact for incompressible flow, it is seen that, if we also use the exact incompressible flow relation

$$P_I = Tu_1 = Tu_0(1 + \delta_1) \tag{46}$$

then we immediately obtain explicit relation between $\delta_1$ and $\delta_3$ by combining Eqs. (45) and (46) so that

$$\delta_1 \approx \frac{1}{2}\delta_3 = \frac{T}{2m_1u_0} = \frac{1 - \eta_1}{\eta_1} \tag{47}$$

As shown in reference 3, Eqs. (45), (46), and (47) are rigorously valid for lightly loaded propellers in incompressible flow. Therefore, we are now in a position to justify the use of all these equations, at least as a rigorous first-order approximation for lightly loaded propellers at low subsonic Mach Numbers.

Since the relations are true only for lightly loaded propellers (for example, the rotation of the slipstream has been neglected, see page 194 of reference 3), we may further simplify the results by neglecting the higher powers of all the $\delta$ increments.

Then Eqs. (16), (38), (40), (41), (46), and (47) reduce to

$$\delta_1 = \left(\frac{T/A}{4q_0}\right)\left[1 - \left(\frac{T/A}{4q_0}\right)(1 - M_0^2)\right] = \frac{1 - \eta_1}{\eta_1} \tag{48}$$

$$T = 4q_0A\delta_1[1 + \delta_1(1 - M_0^2)] \tag{49}$$

$$P_I = Tu_0(1 + \delta_1) = Tu_0/\eta_1 \tag{50}$$

$$m_1 = \rho_0u_0A[1 + \delta_1(1 - M_0^2)] \tag{51}$$

$$\frac{\rho_1}{\rho_0} = (1 - M_0^2\delta_1); \quad \frac{a_1}{a_0} = \left(1 - \frac{\gamma - 1}{2}M_0^2\delta_1\right) \tag{52}$$

$$\frac{M_1}{M_0} = 1 + \delta_1\left(1 + \frac{\gamma - 1}{2}M_0^2\right) \tag{53}$$

These provide the expressions used in Eqs. (19) and (20) for lightly loaded propellers. It is seen that

$$\delta_1 \approx (T/A)/4q_0 \tag{49}$$

as for incompressible flow; consequently, the Mach Number effects on the inflow velocity are negligible when the disc loading is less than one-tenth the free-stream forward flight dynamic pressure ($q_0$), see Fig. 3.

Since the rotational velocity increment $\delta'$ is always much less than $\delta_1$, except near the hub where the assumption of uniform inflow is invalid (see Fig. 46, page 242, of reference 3), it is obvious that $\delta' = 0$ is an extremely satisfactory approximation for lightly loaded propellers. The effect of compressibility is found to be negligible; actually the main effect of $\delta'$ is found to be of the second order. Consideration of the rotational increment $\delta'$ in the general momentum theory shows that the main effect of slipstream rotation is in increasing $\delta_1$ relative to $\delta_3$ by the following relation (see reference 8):

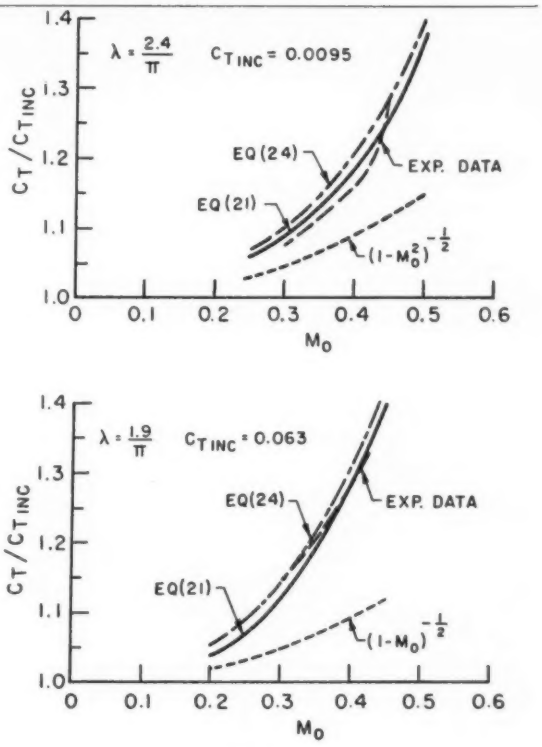


FIG. 5.

$$\delta_1 = (1/2)\delta_3[1 + \delta_1(M_0^2/M_R^2)] \tag{54}$$

This does indicate, however, that Eq. (46) and the subsequent approximations are all that are really justified from the uniform axial-flow momentum theory, since the neglected slipstream rotation produces a second-order effect that must be considered, especially at large $M_0$, if a higher order effect is sought for the larger values of the disc loading.

Fig. 5 compares Eqs. (21) and (24) with the values given in reference 7. Since $M_0$ is relatively small, the difference between Eqs. (21) and (24) is slight. However, Eq. (21) seems to be in better agreement.

A comparison of Eqs. (18) and (21) with all the experimental data in reference 7 shows that Eq. (21) is usually in better agreement with the experimental data. This is not surprising, since the data are for two-bladed propellers and the effect of a finite number of blades, which was entirely neglected in deriving Eq. (19), produces an influence that is opposite to that given by Eq. (19). This may be seen by using the linearized subsonic vortex theory to find the first-order effect of an infinite number of blades for lightly loaded propellers as a power series (see reference 8),

$$\delta_1 = \frac{1}{2}\delta_3 - \frac{1}{8}\frac{\delta_3^2}{\sqrt{1 - M_0^2}} + \ldots \approx \frac{1}{2}\delta_3\left(1 - \frac{\delta_1}{2\sqrt{1 - M_0^2}}\right) \quad (55)$$

Another factor that indicates that Eq. (21) is a better approximation, even for finite loads, is the fact that Eq. (18) already slightly overestimates the compressibility because both $\alpha$ and $\delta_1$ were assumed constant in its derivation. This may be seen by combining Eq. (1) with the differential form of Eq. (47),

$$dT = \rho_1 u_1 (2\delta_1 u_0) 2\pi r \, dr \quad (56)$$

The numerical integration shows that the simultaneous assumption of constant $\alpha$ and $\delta_1$ slightly overestimates the compressibility effect.

Since the influence of a finite load, as shown in Fig. 3, is to increase the compressibility correction and Eq. (18) already overestimates the effect, therefore Eq. (21) is recommended for general use. The actual range of disc loadings that can be analyzed by using Eqs. (18) and (19) can be determined only by comparison with more extensive experimental data, since Eqs. (19), (54), and (55) provide second-order corrections that tend to cancel. Fig. 2 shows that the simple Prandtl-Glauert correction using the helical Mach Number at the three-quarter radius, Eq. (24), provides a satisfactory approximation even for propellers as long as the forward Mach Number and the helical Mach Number remain less than 0.7.

## References


[1] von Krzywoblocki, M. Z., *Elementary Propeller Theories in Compressible Inviscid Fluids*, Applied Scientific Research, Series A, Vol. 2, No. 3, pp. 205–224, 1950.

[2] Vogeley, Arthur W., *Axial-Momentum Theory for Propellers in Compressible Flow*, NACA TN No. 2164, July, 1951.

[3] Durand, W. F., *Aerodynamic Theory*, Vol. IV, pp. 169–360; Julius Springer, Berlin, 1934–1936.

[4] Gessow, Alfred, and Myers, G. C., *Aerodynamics of the Helicopter*, The Macmillan Co., New York, 1952.

[5] Hartshorn, A. S., and Douglas, G. P., *Wind Tunnel Experiments on High Tip Speed Airscrews*, British R. & M. 1438, July, 1931.

[6] von Mises, Richard, *Theory of Flight;* McGraw-Hill Book Company, Inc., New York, 1945.

[7] Stack, John, Draley, E. C., Delano, James, and Feldman, L., *Investigation of the NACA 4-308-03 and NACA 4-308-045 Two Blade Propellers at Forward Mach Numbers to 0.725 to Determine the Effects of Compressibility and Solidity on Performance*, NACA TR No. 999, 1950.

[8] Laitone, E. V., *Actuator Disc Theory for Compressible Flow and a Subsonic Correction for Propellers*, Readers' Forum, Journal of the Aeronautical Sciences, Vol. 20, No. 5, pp. 365–366, May, 1953.



## Changes of Address

Since the Post Office Department does not as a rule forward magazines to forwarding addresses, it is important that the Institute be notified of changes in address 30 days in advance of publishing date to ensure receipt of every issue of the JOURNAL and REVIEW.

Notices should be printed legibly and sent directly to:

**Institute of the Aeronautical Sciences, Inc.**

**2 East 64th Street, New York 21, New York**

# A Steady-Flow Aeroelastic Study by Electrical Analogy

ROBERT H. SCANLAN*

*Centre National des Recherches Scientifiques, France*

SUMMARY

The present paper describes the use of the electrical tank "lifting surface calculator" of Malavard and Duquenne in France for an aeroelastic study. The new items brought out here are: (1) the applicability of this electrical analogy to the calculation of certain "elementary" aerodynamic effects, in incompressible flow, which are of considerable utility; and (2) the specialization of structural influence coefficient concepts, permitted by the availability of the new means of aerodynamic calculation, which allow the calculator to avoid oversimplified notions such as that of an elastic axis and of the rigidity of the lifting surface in the wind or flight direction.

With the analogy in mind, suggestions are also made for subsonic compressible flow aeroelastic lift distribution studies and for accounting for large dihedral effects on incompressible flow distributions.

## INTRODUCTION

MALAVARD AND DUQUENNE[1] HAVE DEVELOPED an effective electrical analogy for the determination of steady-state lift distributions on thin lifting surfaces of arbitrary plan form. In this analogy the electrical potential in a three-dimensional field is identified with the perturbation potential of the flow about the surface.

Pines[5,6] has used a matrix form of the lift distribution on more or less conventional wings to solve their steady-state aeroelastic problems.

In the present study, the analogy of Malavard and Duquenne is fitted to the needs of an aeroelastic study of the type considered by Pines. Structural influence coefficients are so chosen as to be applicable to a large class of lifting surfaces, to avoid questions of an elastic axis, and to account for curvatures in the lifting surface in the direction of the wind. The electrical analogy proves to be sufficiently flexible to permit the determination of new elementary aerodynamic effects directly suited to the structural coefficients chosen. The resulting combination of aerodynamic and structural effects takes on a simpler form than in the original work of Pines. An example is worked out for a delta wing of aspect ratio 2.

Received January 9, 1953.

* Visiting Scientist, Laboratoire Blaise Pascal, Centre National des Recherches Scientifiques, Chatillon-sous-Bagneux, Seine, France. The author is indebted to Prof. J. Pérès, Director, Laboratoire Blaise Pascal, and to Messrs. L. Malavard and R. Duquenne of the Office National d'Études et de Recherches Aéronautiques for encouragement and aid in the conduct of this work. Thanks are also due to the National Research Council of Washington, D.C., whose grant of a Fellowship made possible the contacts that led to the present study.

Other possibilities of the electrical analogy such as new uses of the elementary effects, study of the effect of dihedral, and aeroelastic effects at advanced Mach Numbers are mentioned.

## ELECTRIC TANK ANALOGY OF MALAVARD AND DUQUENNE

Malavard and Duquenne[1] have developed an electrical analogy for potential flow problems concerning thin lifting surfaces. They have exploited this analogy by means of their apparatus called the "lifting surface calculator." It is worth while here to give a brief résumé of this apparatus and the electrical analogy involved.

It is usual in electrical fluid-flow analogies to identify the hydrodynamic potential $\varphi$ with the electrical potential $V$. Here this is done in a three-dimensional ("deep") tank of electrolyte of dimensions approximately 5 by 3 by 4 ft. More precisely, the potential flow about a thin lifting surface as in Fig. 1 is prescribed by a potential

$$\varphi = Ux + \Phi(x, y, z) \qquad (1)$$

where $\Phi$ is the perturbation potential about the surface in a free stream of velocity $U$ far from the surface. It is found more practicable for the particular analogy at hand to consider only the perturbation potential $\Phi$, and

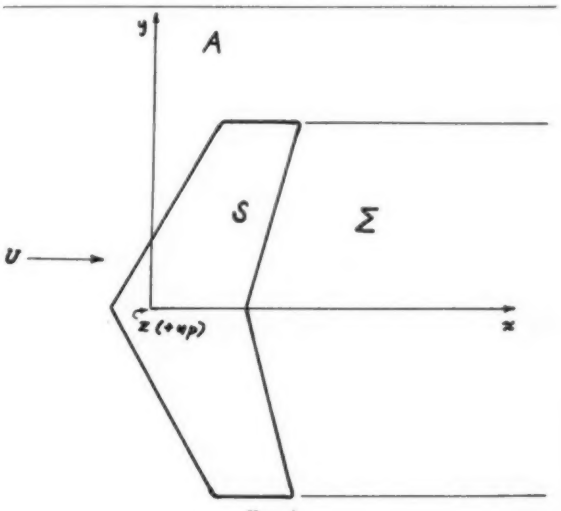


FIG. 1.

it is accordingly this $\Phi$ that is identified with the electrical potential $V$ of the field within the tank. The tank is made of slate or other insulating material. The electrolyte found by Malavard to be most practical from a variety of points of view is ordinary tap water. Also, in practice, alternating current of low voltage and of frequency 1,000 cycles per sec. or over is used.

The pressure difference $\pi$ over the thin lifting surface of Fig. 1 (which is confounded with its projection in the $xy$-plane) is

$$\pi = -\rho U(\partial\Phi/\partial x) \tag{2}$$

The condition that the airflow be tangent to the surface of Fig. 1 defined by $z = f(x, y)$ is

$$\left(U + \frac{\partial\Phi}{\partial x}\right)\frac{\partial f}{\partial x} + \frac{\partial\Phi}{\partial y}\frac{\partial f}{\partial y} = \frac{\partial\Phi}{\partial z} \tag{3}$$

which simplifies to

$$\partial\Phi/\partial z = U(\partial f/\partial x) \tag{4}$$

for small slopes $\partial f/\partial x$, $\partial f/\partial y$ and perturbation velocities $\partial\Phi/\partial x$, $\partial\Phi/\partial y$. The circulation $\Gamma(y)$ about a single section of the surface parallel to the $x$-axis is related to the potential $\Phi$ by

$$\Gamma(y) = 2\Phi(x_t, y) \tag{5}$$

where $x_t$ is the $x$-coordinate of the trailing edge at that section.

The application of Ohm's Law to a current $i$ passing into an electrolyte of potential distribution $V$ through an electrode of area $dS$ is

$$i = -\sigma(dV/dn)\,dS \tag{6}$$

where $\sigma$ is the conductivity of the liquid and $n$ is the outward normal to its surface.

The analogy of Malavard and Duquenne consists of the following arrangement. The tank is filled with water to the full depth possible. The free surface of the water represents the plane of the surfaces of discontinuity which are to represent the wing, its wake, and the surrounding area. The wing, $S$, is represented by a flat surface, in contact with the free surface of the electrolyte, and covered by a series of closely spaced flush electrodes separated by insulating spaces (Fig. 2). Each of these small electrode surfaces, of area $dS$, has a controlled current passed into the electrolyte through it. The amount of this current, if $dV/dn$ is identified in the analogy with $\partial\Phi/\partial z$, is given by Eq. (6) as

$$i = -\sigma U(\partial f/\partial x)\,dS \tag{7}$$

In the wake, the surface $\Sigma$ of Figs. 1 and 2 is in contact with the free surface of the water, and it consists of long thin electrode strips separated by narrow insulating bands. The surrounding area $A$ in the same plane is placed at zero potential by means of a large metallic surface plate, at zero potential, just in contact with the water surface, and covering the rest of the free surface of the water in the tank. As the correct currents, Eq. (7), are introduced and maintained, the trailing-edge Kutta-Joukowsky condition is satisfied by placing each of the wake electrode bands at the same potential as the wing trailing-edge electrode just ahead of it. (To aid in accomplishing this simply in practice, each trailing-edge electrode is sometimes made to lie half in the wing and half in the wake. See Fig. 5.)

The scale relation between $\Phi$ and $V$ is given by

$$\Phi = [U(\partial f/\partial x)/(i/\sigma\,dS)]V \tag{8}$$

or, if the "reduced circulation" $\gamma = 2\Phi/Ul$ is introduced (where $l$ is the semispan of the wing being studied),

$$\gamma = 2\frac{\sigma R[(\partial f/\partial x)dS]}{l}\frac{V}{\Delta V} \tag{9}$$

where $\Delta V$ is a means of measuring the current $i$ through use of a known resistance $R$: $Ri = \Delta V$.

The fact that the whole manipulation of this analogy is concerned with potential values (in particular, perturbation potential values) bears emphasis. For example, from Eq. (2) lift values per unit span

$$\int_{-\infty} \pi\,dx = -\rho U\Phi \tag{10}$$

are available directly from the potentials to be read at the lifting surface electrodes. The studies normally made require only a semispan wing situated with its $x$-axis horizontal along one flat vertical wall of the tank and the $y$-axis in the free-water surface. Conditions of symmetry or antisymmetry of loading are represented, respectively, by making this wall insulating or conducting.

A further exposé of this deep tank work of Malavard and Duquenne would be repetitious, but suffice it to point out that for wings of sweptback and other modern plan forms they have found excellent agreement with the lift distributions predicted by the analytical methods of Falkner,[2] Weissinger,[3] and others. The appara-

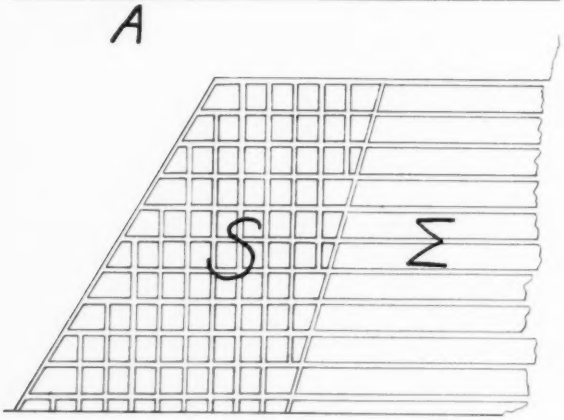


FIG. 2.

tus described is in current use and is not limited to wings of regular plan form; the possibility of studying the lift distribution over wings of decidedly bizarre plan form is not the least of the advantages of this analogy. With modifications in technique even the effects of tip tanks and end plates could be introduced into the studies.

In the case of an untwisted rigid wing at an angle of attack $\alpha$, the value $\alpha = -\partial f/\partial x$ is constant throughout the lifting surface, and, hence, by Eq. (7), the current $i$ at each electrode is proportional only to the respective area $dS$ served. Duquenne[4] has profited by this circumstance to replace, in this case, the surface $S$ (Fig. 2) by a simple hole in the plate $A$ cut to the plan form of the wing. The current to replace the uniformly distributed electrode currents $i$ is then furnished by a plate covering the entire bottom of the deep tank and raised to a potential above zero. The perturbation potential field of the wing is then read by means of a traveling probe dipped slightly into the water. The location of the probe in the horizontal plane is easily followed on an accompanying drafting board by a tracing point attached to an extension of the probe carriage.

Both the wing plan form represented by a great number of electrodes and that replaced by a cutout may be deformed geometrically as necessitated by potential flow studies at elevated Mach Numbers less than 1, so that the analogical system of Malavard and Duquenne may be said to be useful in the entire subsonic range of steady flow.

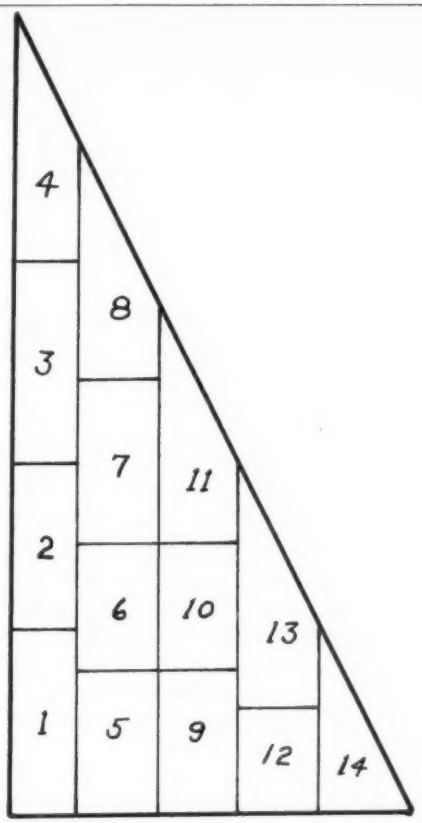


FIG. 3.

## ELEMENTARY EFFECTS

As is commonly the case in structural studies, so also in aerodynamic studies on a new design it is desirable first to concentrate attention upon "elementary" effects. For example, for a variety of loading conditions on a rigid aerodynamic surface it is convenient to have at hand a set of "unit" studies combinable at will. This is indispensable in aeroelastic studies, where elementary structural effects (often given by a matrix of influence coefficients) interact with corresponding aerodynamic effects. It was then natural to require for the present study a flexible means for finding elementary aerodynamic effects applicable to a wide variety of lifting surfaces. This requirement is admirably fulfilled, in the author's opinion, by the lifting surface calculator of Malavard and Duquenne.

One common structural assumption in wing studies (even of sweptback and delta wings) is that sections parallel to the wind are rigid. It was decided here to depart from this assumption, which is decidedly weak in certain cases, notably that of a flexible delta wing. The question of what type of structural influence coefficients to use is immediately posed. Here it was decided to demand certain "angles of attack per unit load." The actual wing under study (see "Example" and Fig. 3) was divided up into a number (here 14) of segments, assumed small enough so that only the forces (without residual moments) acting upon them needed to be taken into account at the centroids of the segments. The different segments in the chord direction being permitted to have different slopes, the following structural influence coefficients $\theta_{ij}$ were sought: "the increase in angle of attack $\theta_{ij}$ in the wind direction at the segment $i$ due to a unit normal load at segment $j$." The resulting square matrix of structural influence coefficients is here designated $\Theta$. It is to be noted that with these influence coefficients the subsequent analysis is rid of any "elastic axis."

The aerodynamic "influence coefficients" required to correspond to the general structural ones defined above are purely "mathematical" ones in the sense that, individually, they are isolated "unit effects" scarcely obtainable by an aerodynamic test on a physical model. However, the electrical analogy method provides them with ease, and here it has an advantage also over truly mathematical elementary effects, since these would be extremely difficult to calculate. Here the aerodynamic influence coefficient (with reference, for example, to Fig. 3, where $i, j = 1, \ldots, 14$) is "the lift on segment $i$ due to a unit change in the angle of attack of segment $j$." The resulting square matrix of aerodynamic influence coefficients is given by

$$[(1/2)\rho U^2 l^2]G = qlG \tag{11}$$

where the matrix $G$ is composed of nondimensional elements $(\Delta y_i/l)\gamma_{ij}$—"the reduced circulation on segment $i$ due to a unit change in the angle of attack of segment $j$ multiplied by the ratio of the width $\Delta y_i$ of the segment $i$ to the semispan $l$." (Above, $\rho$ is the density of the air.) The technique of obtaining these aerodynamic coefficients will be explained in some detail in connection with the example presented.

## Steady-Flow Aeroelastic Theory

Pines[5, 6] has used elementary effects in calculating wing loading distributions for aeroelastic studies on more or less conventional wings. The general form of the work of Pines is well adapted to the present study. In fact, the present study takes an even simpler form for the reasons that the elastic axis is dispensed with and the elementary aerodynamic effects are drawn from simple analogical tests rather than from theory.

Here the distribution of aerodynamic loading throughout a surface is considered. If the segments of the surface (as in Fig. 3) are numbered consecutively, the lifts $p_i$ at these segments may be represented by a column matrix $\{p\}$ having as many items $p_i$ as there are segments $i$. The aerodynamic lift forces are simply expressed by

$$\{p\} = qlG\{\alpha\} \tag{12}$$

where

$$\{\alpha\} = \{\alpha_R\} + \{\alpha_E\} \tag{13}$$

is the angle of attack distribution of the segments, separated into the parts $\alpha_R$ (due to rigid surface) and $\alpha_E$ (due to elasticity of the surface). The elastic part depends on both the inertia loads $p_I$ and aerodynamic loads $p$:

$$\{\alpha_R\} = \Theta[\{p_I\} + \{p\}] \tag{14}$$

where $\{p_I\} = \{nW\}$, $W$ being the weight of the section subjected to $n$ g's acceleration. Eqs. (12) to (14) combined yield

$$\begin{aligned}\{p\} &= qlG[\{\alpha_R\} + \Theta(\{p_I\} + \{p\})] \\ &= qlG\{\alpha_R\} + qlG\Theta\{p_I\} + qlG\Theta\{p\}\end{aligned} \tag{15}$$

or

$$\{p\} = \{p\}_1 + qA\{p\} \tag{16}$$

where $lG\Theta = A$.

The directly calculable column $\{p\}_1$ is usually a good approximation to $\{p\}$. To include the aeroelastic part of Eq. (16), an iteration method then is easily set up by replacing $\{p\}$ on the right by $\{p\}_1$, then by $\{p\}_1 + qA\{p\}_1$, etc. The result is the series

$$\begin{aligned}\{p\} = \{p\}_1 + qA\{p\}_1 + q^2A^2\{p\}_1 + \\ \ldots + q^rA^r\{p\}_1 + \ldots\end{aligned} \tag{17}$$

Because of the inherent nature of the matrix iteration process, for some integer $N$ large, $A^N\{p\}_1 = \{p\}_c$ where $\{p\}_c$ is a characteristic column associated with a characteristic value $\lambda$ such that, for any integer $r$, $A^r\{p\}_c = \lambda^r\{p\}_c$. Thus, at the first point $m$ such that $A^m\{p\}_1 = \{p\}_c$, the powers of the matrix $A$ in series (17) can be replaced by powers of $\lambda$,

$$\begin{aligned}\{p\} = \{p\}_1 + qA\{p\}_1 + q^2A^2\{p\}_1 + \ldots \\ + q^m\{p\}_c(1 + q\lambda + q^2\lambda^2 + \ldots)\end{aligned} \tag{18}$$

The series in parentheses sums to $1/(1 - q\lambda)$ for $q\lambda < 1$, so that the divergence speed of the surface is given by $q = 1/\lambda$.

Theory of this type is extendable to effectiveness of ailerons,[6] or other flaps and is, of course, simply applicable as it stands to the question of divergence. As presented it is suited only to the incompressible range. A word on the compressible range is given later in connection with a suggested iteration involving repeated applications of the electrical analogy.

## Example

A flat-plate delta wing of aspect ratio 2 is chosen for the present study (Fig. 3). Structural deflection influence coefficients were obtained (in a somewhat crude fashion) from a 5-mm. thick Plexiglas model of semispan 1.05 ft., and these were transformed by (also somewhat crude) calculation directly into the matrix $\Theta$ of slopes per unit loads. Greater care should be taken in obtaining these coefficients in the case where results, rather than method, are important. It may be mentioned in passing that another analogical method mentioned by Malavard[7] is useful in the approximate calculation of flat-plate deflection influence coefficients if it is desired to calculate rather than measure these coefficients. Williams[8] has suggested a semiempirical method for such calculation which requires the knowledge of the central flow line from a point of loading (source) to a symmetrically located point (sink) (on

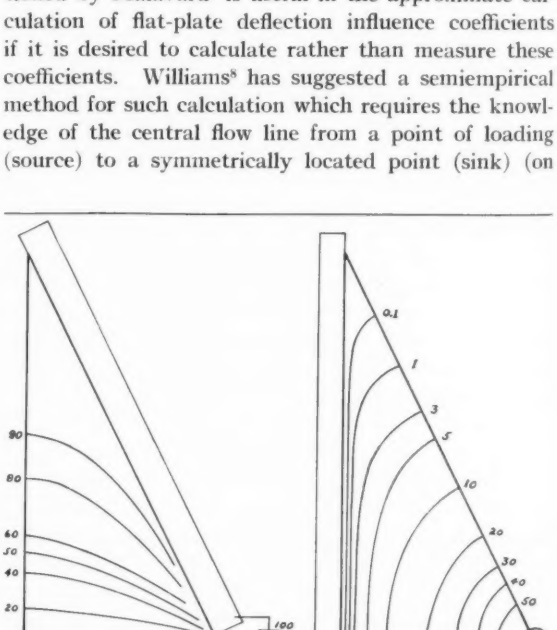


Fig. 4.

the opposite half-wing) within a channel having the plan form of the wing. The flow lines (and their orthogonal family of equipotential lines) are rapidly given by an application of the "Teledeltos" conducting paper technique of Malavard.[7] These flow lines were obtained for the present wing, for a single tip load only, by means sketched in Fig. 4, where thin copper electrodes are shown attached to the conducting paper and are placed at potentials of 100 and zero, respectively. A few representative lines are included in the sketch with their potentials marked. The conducting paper furnishes a plane field of uniform resistance, the electrical potential of which is measurable by a simple Wheatstone bridge. A pencil-like probe is pressed against the paper at various points to pick up the potential there and to measure it by balancing the bridge. The lines of equal potential are quickly plotted out. They are the analog of a fluid or stress-flow field. It is interesting that the Teledeltos technique rectifies directly a weakness pointed out by Williams of the flow-line method—namely, the difficulty of making calculations for a number of different load locations.

The deflection influence coefficients of the Plexiglas plate were first calculated. The approximate slope influence coefficients calculated from them were next obtained (matrix $\Theta$). Because of the extremely small deflections at segments 1 to 4, their values and their effects elsewhere were taken as zero in this study. (Note that several tables, such as the above-mentioned influence coefficients and other lengthy numerical items are intentionally omitted from this paper in the interests of conserving space.)

For the aerodynamics of the delta wing by the analogy method, the model shown in Fig. 5 was constructed, having 110 electrodes composed simply of a conducting paint. Upon the figure are designated the relative values of the areas served by electrodes of typical configuration. The electrodes were grouped in such a way as to confine a distinct group of six or more electrodes within each of the 14 segments into which the lifting surface was divided.

Fourteen separate "elementary" electrical analog tests were performed, in each of which currents proportional to the areas served by the electrodes of one single segment were made to flow, other segments not being fed electrically. Potentials were read at all the electrodes. Table 1 is a typical one (for segment 6) of the 14 elementary distributions of potential, expressed in the reduced form of $\gamma$ per unit angle of attack (of segment 6).

As a means of verification of the techniques used in the elementary studies, the entire wing was fed electrically by currents proportional at each point to the area served. The result for the entire wing (representing the potential distribution for a unit angle of attack) was compared with the sum of the elementary results. As a second means of verification, these two results were compared with those obtained by performing the experiment with a cutout wing and current sent from the tank bottom. The results of the three different methods are presented in Table 2. It is seen that the sum of the elementary effects is high with respect to the results of the two other methods. Unfortunately, these results do not represent the accuracy obtainable by the methods, for certain manipulative errors were later found to explain the trend of these discrepancies. There may possibly be occasions where elementary effects defined by too-small groups of electrodes will falsify the results because of inadequate representation at a finite set of points of an essentially continuous phenomenon. Such occasions can always be remedied by changes of scale so as to increase the number of electrodes, etc. To improve elementary results, which are uniformly too high by a small percentage, it is also permissible to reduce all of them by the same factor that brings their sum into agreement with the usually excellent results of the cutout wing technique. Here it will simply be assumed that the elementary effects of the example are not in error.

Eq. (2) shows that, to obtain the pressure difference distribution on the surface, each potential distribution must be differentiated with respect to $x$. On the other hand, Eq. (10) shows that lift per unit span is given directly by the potential; in fact the difference between potential values on either side of an elementary segment (in the $x$-direction) gives exactly the lift on that segment when multiplied by the segment's width. (The appropriate scale factor must be included when dealing with the values of *electrical* potential.)

Proceeding thus, again in a somewhat crude manner and without graphing the potential distributions, the elementary lift distributions were obtained for unit angles of attack of the various segments. These were set up in a table of aerodynamic influence coefficients which represented the matrix $G$ of reduced circulations $\gamma_{ij}$ scaled by the width ratios $\Delta y_i/l$ appropriate to their segments. The distribution of lifts per segment when the entire wing was studied as a unit is presented in the right-hand column of Table 3. The left-hand column represents $G\{1\}$. The disparity of the columns confirms the crudity of the segment lift calculation—for which refinements are obvious. It was further assumed that all these lifts act at the area centroid of their respective segments. This is again a source of error permitting obvious refinements, such as the choice of a more probable (aerodynamic) centroid of loading under a representative loading condition. Also, if an increase in complexity of the analysis were permitted, introduction of moment (as well as force) influence coefficients could account for more refinements. The subdivision of the wing into many small segments has the effect of cutting down the seriousness of the errors of geometry retained here. With automatic computing-machine aids many more than 14 segments could be employed.

TABLE 1 ↘: REDUCED CIRCULATION per unit angle of attack of SECTION 6 $\gamma/(\frac{\partial \Gamma}{\partial \alpha})_6$

| | | | TRAILING EDGE | | | | | | | |
|---|---|---|---|---|---|---|---|---|---|---|
| 0.008 | 0.012 | 0.019 | 0.025 | 0.032 | 0.038 | 0.043 | 0.048 | 0.052 | 0.054 | 0.056 |
| L | | | | | | | | | | |
| 0.10 | 0.010 | 0.019 | 0.027 | 0.035 | 0.044 | 0.050 | 0.057 | 0.060 | 0.063 | 0.063 |
| 0.21 | | | | | | | | | | |
| 0.20 | E | | | | | | | | | |
| 0.34 | 0.30 | 0.018 | 0.027 | 0.037 | 0.048 | 0.058 | 0 067 | 0.071 | 0.071 | 0.072 |
| 0.38 | 0.25 | | | | | | | | | |
| 0.40 | 0.27 | | | | | | | | | |
| 0.47 | 0.40 | 0.013 | 0.026 | 0.039 | 0.053 | 0.073 | 0.095 | 0.091 | 0.085 | 0.083 |
| 0.48 | 0.43 | | | | | | | | | |
| 0.51 | 0.44 | A | | | | | | | | |
| 0.57 | 0.51 | 0.31 | 0.025 | 0.040 | 0.061 | 0.098 | 0.235 | 0.254 | 0 104 | 0.097 |
| 0.60 | 0.55 | 0.34 | | | | | | | | |
| 0.63 | 0.57 | 0.36 | | | | | | | | |
| 0.67 | 0.63 | 0.50 | 0.019 | 0.040 | 0.064 | 0.111 | 0.256 | 0.266 | 0.115 | 0.108 |
| 0.69 | 0.64 | 0.53 | | | | | | | | |
| 0.71 | 0.66 | 0.56 | D | | | | | | | |
| 0.76 | 0.73 | 0.62 | 0.38 | 0.033 | 0.058 | 0.098 | 0.236 | 0.249 | 0.121 | 0.103 |
| 0.78 | 0.74 | 0.64 | 0.38 | | | | | | | |
| 0.82 | 0.75 | 0.64 | 0.42 | | | | | | | |
| 0.86 | 0.82 | 0.73 | 0.56 | 0.021 | 0.047 | 0.071 | 0.102 | 0.108 | 0.092 | 0.086 |
| 0.88 | 0.84 | 0.75 | 0.60 | | | | | | | |
| 0.93 | 0.90 | 0.77 | 0.64 | I | | | | | | |
| 0.94 | 0.91 | 0.84 | 0.70 | 0.40 | 0.033 | 0.048 | 0 061 | 0.067 | 0 067 | 0 067 |
| 0.96 | 0.94 | 0.85 | 0.72 | 0.43 | | | | | | |
| 1.01 | 1.01 | 0.89 | 0.75 | 0.47 | | | | | | |
| 1.02 | 0.99 | 0.93 | 0.81 | 0.60 | 0 017 | 0.033 | 0.043 | 0.047 | 0.051 | 0.052 |
| 1.08 | 1.02 | 0.95 | 0.83 | 0.65 | | | | | | |
| 1.15 | 1.07 | 0.97 | 0.87 | 0.69 | N | | | | | |
| 1.09 | 1.07 | 1.02 | 0.92 | 0.74 | 0.40 | 0.024 | 0.030 | 0.034 | 0.038 | 0.041 |
| 1.10 | 1.08 | 1.01 | 0.91 | 0.77 | 0.43 | | | | | |
| 1.14 | 1.14 | 1.04 | 0.95 | 0.81 | 0.49 | | | | | |
| 1.16 | 1.14 | 1.09 | 1.00 | 0.86 | 0.62 | 0.012 | 0.021 | 0.026 | 0.028 | 0.031 |
| 1.17 | 1.15 | 1.09 | 1.01 | 0.88 | 0.68 | | | | | |
| 1.20 | 1.17 | 1.12 | 1.04 | 0.91 | 0.72 | G | | | | |
| 1.23 | 1.21 | 1.14 | 1.08 | 0.96 | 0.77 | 0.40 | 0.015 | 0.019 | 0.021 | 0.024 |
| 1.23 | 1.21 | 1.17 | 1.09 | 0.97 | 0.81 | 0.45 | | | | |
| 1.27 | 1.24 | 1.21 | 1.12 | 1.00 | 0.85 | 0.47 | | | | |
| 1.28 | 1.27 | 1.22 | 1.15 | 1.04 | 0.88 | 0.43 | 0.008 | 0.013 | 0.015 | 0.018 |
| 1.28 | 1.26 | 1.22 | 1.15 | 1.05 | 0.90 | 0.69 | | | | |
| 1.32 | 1.30 | 1.25 | 1.18 | 1.07 | 0.93 | 0.72 | E | | | |
| 1.34 | 1.32 | 1.28 | 1.22 | 1.12 | 0.96 | 0.78 | 0.42 | 0.009 | 0.012 | 0.014 |
| 1.34 | 1.31 | 1.30 | 1.21 | 1.13 | 1.00 | 0.81 | 0.45 | | | |
| 1.38 | 1.35 | 1.30 | 1.24 | 1.18 | 1.03 | 0.85 | 0.50 | | | |
| 1.38 | 1.37 | 1.33 | 1.27 | 1.19 | 1.06 | 0.89 | 0.43 | 0.006 | 0.008 | 0.011 |
| 1.36 | 1.35 | 1.32 | 1.24 | 1.18 | 1.07 | 0.91 | 0.70 | | | |
| 1.41 | 1.40 | 1.37 | 1.30 | 1 22 | 1.10 | 0.94 | 0.73 | D | | |
| 1.43 | 1.42 | 1.38 | 1.33 | 1.25 | 1.14 | 0.98 | 0.77 | 0.40 | 0.006 | 0.007 |
| 1.41 | 1.42 | 1.37 | 1.33 | 1.30 | 1.15 | 1.01 | 0.82 | 0.46 | | |
| 1.48 | 1.48 | 1.42 | 1.37 | 1.30 | 1.18 | 1.03 | 0.85 | 0.47 | | |
| 1.43 | 1.42 | 1.43 | 1.37 | 1.29 | 1.19 | 1.06 | 0.88 | 0.62 | 0.003 | 0.006 |
| 1.45 | 1.46 | 1.42 | 1.38 | 1.30 | 1.21 | 1.08 | 0.91 | 0.68 | | |
| 1.53 | 1.52 | 1.46 | 1.41 | 1.34 | 1.25 | 1.11 | 0.94 | 0.72 | G | |
| 1.50 | 1.48 | 1.43 | 1.38 | 1.32 | 1.22 | 1.10 | 0.94 | 0.72 | 0.36 | 0.002 |
| 1.47 | 1.48 | 1.44 | 1.41 | 1.34 | 1.25 | 1.15 | 0.99 | 0.78 | 0.44 | |
| 1.53 | 1.55 | 1.51 | 1.43 | 1.36 | 1.27 | 1.15 | 1.00 | 0.81 | 0.47 | E |
| 1.50 | 1.48 | 1.45 | 1.40 | 1.33 | 1.23 | 1.12 | 0.96 | 0.75 | 0.48 | 0.19 |
| 1.47 | 1.48 | 1.46 | 1.41 | 1.34 | 1.26 | 1.17 | 1.03 | 0.85 | 0.59 | 0.30 |
| 1.53 | 1.56 | 1.52 | 1.45 | 1.37 | 1.28 | 1.18 | 1.04 | 0.87 | 0.60 | 0.33 |

SYMMETRY WALL

SYMMETRY WALL

TRAILING EDGE

TABLE 2 ↗: REDUCED CIRCULATION for UNIT ANGLE OF ATTACK OF THE ENTIRE WING
UPPER: CUT-OUT WING TEST MIDDLE: ENTIRE WING WITH ELECTRODES LOWER: SUM OF ELEMENTARY EFFECTS

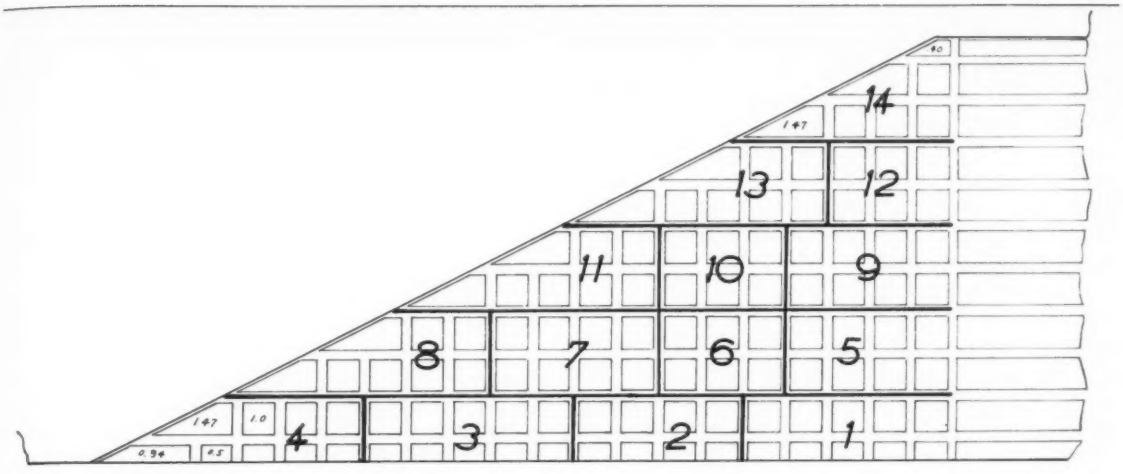


FIG. 5.

The matrix $G\Theta$ was next calculated.

For the calculation of this example the lift per unit angle of attack is given by

$$|p| = \bar{q}G\{1\} + \bar{q}^2AG\{1\} + \bar{q}^3A^2G\{1\} + \bar{q}^4A^3G\{1\} + \bar{q}^5A^4G\{1\}[1/(1 - \bar{q}\lambda)]$$

since the iteration process converged on the fourth multiplication. Above, and for the example only, the following notation is used:

$$\bar{q} = (1/2)\rho U^2 l^2$$
$$A = G\Theta$$

Items of interest in the iteration of $A$ are given in Table 4.

$\lambda = 393 \times 10^{-8}$ rad. per Gm. $= 1.79 \times 10^{-3}$ rad. per lb.

For the critical divergence velocity $U_c$ at sea level ($\rho = \rho_0$)

$$(1/2)\rho_0 U_c^2 l^2 \lambda = 1$$
$$U_c = 445 \text{ m.p.h.}$$

### The Effect of Lifting Surface Dihedral

It has been mentioned above that account can be taken of symmetry or antisymmetry of the wing system. It is, in the symmetric case, possible to take account of wing dihedral and the effect of spanwise flow on the overall results. This is a nonlinear effect as is seen from the form (3), where "small" terms are no longer neglected. As an example, consider one of the elementary effects mentioned above. From Eqs. (3) and (9) there is obtained

$$\gamma/\theta = \frac{2\sigma R\, dS\, V}{l\Delta V} \tag{19}$$

where $\theta$ is the "generalized angle of attack,"

$$\theta = \frac{\partial f}{\partial x} + \frac{l}{2}\left(\frac{\partial \gamma}{\partial x}\frac{\partial f}{\partial x} + \frac{\partial \gamma}{\partial y}\frac{\partial f}{\partial y}\right) \tag{20}$$

of the segment in question. It is the distribution $\gamma/\theta$ which is obtained directly from the electrical analogy. If Eq. (20) is written

$$\theta = \frac{\partial f}{\partial x} + \frac{l}{2}\left(\frac{\partial(\gamma/\theta)}{\partial x}\frac{\partial f}{\partial x}\theta + \frac{\partial(\gamma/\theta)}{\partial y}\frac{\partial f}{\partial y}\theta\right)$$

it follows immediately that

$$\theta = \frac{\partial f/\partial x}{1 - \frac{l}{2}\left(\frac{\partial(\gamma/\theta)}{\partial x}\frac{\partial f}{\partial x} + \frac{\partial(\gamma/\theta)}{\partial y}\frac{\partial f}{\partial y}\right)} \tag{21}$$

Thus $\theta$ is seen as a generalization of the angle of attack

| | Table 3 | | Table 4 | | Table 5 |
|---|---|---|---|---|---|
| | $10^2 \times G\{1\}$ | By Table 2 | $10^2 \times G\{1\}$ / 19.7 | Result of Iteration | Effective Per Cent Drop in the Actual Angle of Attack of 20° Caused by a Dihedral of 20° at the Elementary Segment (Symmetry of Segment with Opposite Half-Wing Is Assumed) |
| 1 | 2.4 | 2.1 | 0.124 | 0.0354 | 9.5 |
| 2 | 3.3 | 3.2 | 0.169 | 0.0850 | 5.4 |
| 3 | 6.4 | 6.2 | 0.326 | 0.1773 | 6.5 |
| 4 | 11.1 | 10.8 | 0.563 | 0.1785 | 8.5 |
| 5 | 2.4 | 2.4 | 0.122 | 0.0291 | 9.0 |
| 6 | 3.5 | 3.2 | 0.180 | 0.0405 | 2.5 |
| 7 | 6.4 | 6.4 | 0.325 | 0.1573 | 3.3 |
| 8 | 17.4 | 16.8 | 0.885 | 0.4948 | 6.1 |
| 9 | 2.5 | 2.4 | 0.129 | 0.0638 | 5.9 |
| 10 | 4.7 | 5.0 | 0.240 | 0.1381 | 3.0 |
| 11 | 19.3 | 18.6 | 0.981 | 0.7079 | 6.4 |
| 12 | 2.6 | 2.8 | 0.133 | 0.1523 | 8.2 |
| 13 | 19.7 | 19.2 | 1.000 | 1.0000 | 7.5 |
| 14 | 15.0 | 14.5 | 0.762 | 0.9137 | 17.9 |

$\partial f/\partial x$ for the case where the elementary segment is canted both in the wind direction ($\partial f/\partial x$) and in the spanwise (dihedral) direction ($\partial f/\partial y$). Table 5 presents some results for elementary effects showing the per cent reduction in effective angle of attack: $\{[(\partial f/\partial x) - \theta]/(\partial f/\partial x)\} \times 100$ per cent for an assumed angle of attack of 20° and a dihedral angle of 20° of the elementary segment. Such studies might be of interest in certain $V$-empennage or star-fin arrangements where dihedral is large.

If overall, instead of elementary, effects are dealt with, it is not possible to have $\gamma$ directly from a single experiment, for, by Eq. (20), $\gamma$ is given by a differential equation the coefficients of which vary over the wing area. An iteration for $\gamma$ can be envisaged simply as a preliminary distribution of $\gamma$ (unmodified), the slopes of which are to be used in Eq. (20) to reestimate $\theta$, followed by a second experiment using new currents

$$i = -\sigma U \theta \, dS \tag{22}$$

and yielding a new approximation to $\gamma$, etc.

## Conclusion

The centering of attention upon elementary effects, as in the present study, appears feasible from the analogy point of view and effective in a typical aeroelastic problem. In addition, it points to the possibility, aside from questions of aeroelasticity, of taking into account dihedral; of investigating the efficient location of ailerons, elevons, or flaps; of the orienting of the hinge lines of these elements so as to benefit from regions of decided spanwise flow; of the studying of various rigid wing twist distributions as sums of elementary distributions with the aim of achieving a given surface lift distribution (with or without elastic changes).

The possibility of compressible flow studies has been mentioned. For the case of aeroelastic effects, matrix iterations based on linear effects are no longer possible; but it remains possible to make such investigations on the "analog-iteration" basis, somewhat as indicated for the case of dihedral. The procedure is, for example, to study a given "rigid wing" loading at a given Mach Number. With the loading found, a new wing deformation is calculated from the structural data. With recourse again to the analogy, a new loading at the given Mach Number is found. The process may be repeated until convergence at the given Mach Number and likewise may be reproduced at several Mach Numbers. Actual speeds of reversal of control effectiveness are then obtained from extrapolation of the results, etc. It is generally more useful to have at hand a continuous plot of "effectiveness" data than to know simply the critical velocities of reversal or divergence. The iterative use of the electrical analogy in compressible flow cases, as suggested here, resembles some of the old incompressible flow methods in use prior to the advent of recent aeroelastic theory: such methods habitually calculated loading, then deflection, then new loading, etc. However, the analogy improves the situation by doing the difficult calculation—the aerodynamic load distribution—rapidly.

## References


[1] Malavard, L., and Duquenne, R., *Étude des surfaces portantes par analogies rhéoélectriques*, La Recherche Aéronautique, No. 23, September-October, 1951.

[2] Falkner, V. M., *The Calculation of the Aerodynamic Loading on Surfaces of Any Shape*, British R. & M. 1910, 1943.

[3] *Calculated Loadings Due to Incidence of a Number of Straight and Swept-back Wings*, British ARC, 11-542, 1948. Also Weissinger, J., *The Lift Distribution of Swept-back Wings*, NACA TN No. 1120, 1947.

[4] Duquenne, R., *Sur le calcul analogique des surfaces portantes*, Comptes Rendus des scéances de l'Académie des Sciences, May 26, 1952.

[5] Pines, S., *A Unit Solution for Load Distribution of a Non-rigid Wing by Matrix Methods*, Journal of the Aeronautical Sciences, Vol. 16, No. 8, p. 470, August, 1949.

[6] Scanlan, R. H., and Rosenbaum, R., *Aircraft Vibration and Flutter;* The Macmillan Company, New York, 1951.

[7] Malavard, L., *Sur une nouvelle technique dans le calcul expérimental par analogies électriques*, La Recherche Aéronautique, No. 20, March-April, 1951.

[8] Williams, M. L., *A Review of Certain Analysis Methods for Swept-Wing Structures*, Journal of the Aeronautical Sciences, Vol. 19, No. 9, p. 615, September, 1952.

# The Second-Order Lifting Pressure and Damping in Roll of Sweptback Rolling Airfoils at Supersonic Speeds

JOHN C. MARTIN* AND NATHAN GERBER†

*Ballistics Research Laboratories, Aberdeen Proving Ground*

SUMMARY

The lifting pressure distribution and the damping in roll are determined for rolling sweptback airfoils with arbitrary cross sections. The time variation in the partial differential equation is eliminated by utilizing a set of coordinate axes that are attached to and rolling with the airfoil. The second-order lifting pressure is determined by an iterative method, and the damping in roll is calculated from the pressure distribution. The results are shown to agree well with available experimental data.

## INTRODUCTION

THE LIFTING PRESSURE DISTRIBUTION and the damping in roll are calculated on the basis of a second-order theory similar to the one introduced by Busemann[1] and extended by Van Dyke.[2, 3] The airfoils considered here are infinite swept wings with arbitrary symmetrical cross sections. It is the authors' opinion that from the study of these relatively simple airfoils effects of thickness on other airfoils can be estimated.

Recent work by Milton D. Van Dyke[2, 3] indicates that second-order solutions of the partial differential equation of steady supersonic flow can be obtained by the use of iterative methods. The partial differential equation considered here is not the equation of steady supersonic flow, but it is similar, and we shall assume that the second-order solution can be obtained by iterative methods.

It will also be assumed that the characteristics are the same for the first- and second-order solutions (this assumption was made in references 2 and 3). For steady plane flow the second-order solution[2] found by an iterative method based on the preceding assumption yields the correct second-order pressure of the Busemann second-order theory.

Unfortunately, no such justification of the preceding assumption is known to the authors for three-dimensional flows.

## THE PARTIAL DIFFERENTIAL EQUATION

The partial differential equation to be used is a special case of the three-dimensional time-dependent equation for the potential function of a nonviscous compressible fluid. This equation can be written as [reference 4, Eq. (8)]

$$\left[c^2 - \frac{\gamma - 1}{2}\left(\Omega_{x'}{}^2 + \Omega_{y'}{}^2 + \Omega_{z'}{}^2 + 2\Omega_{t'} - V^2\right)\right]\nabla^2\Omega = \Omega_{t't'} + \frac{1}{2}\nabla\Omega\cdot\nabla(\nabla\Omega\cdot\nabla\Omega) + \frac{\partial}{\partial t'}(\nabla\Omega\cdot\nabla\Omega) \qquad (1)$$

where $c$ is the velocity of sound in the undisturbed stream ahead of the airfoil, $\gamma$ is the adiabatic exponent, and $V$ is the velocity of the free stream.

A perturbation will be used which is defined by

$$\Omega \equiv V(x' + \Phi) \qquad (2)$$

Note that the perturbation potential, $\Phi$, has been normalized through division by the free-stream velocity. Eq. (2) indicates that the coordinate axes have been chosen so that the free-stream velocity is parallel to the $x'$-axis.

The coordinate axes of Eq. (1) are fixed in space. It is more convenient, however, to choose a new set of axes fixed to and rolling with the airfoil, the $x$-axis coinciding with the axis of roll. The relations between the components of the two sets of axes are

$$\left.\begin{aligned} x &= x' \\ y &= y'\cos pt' + z'\sin pt' \\ z &= -y'\sin pt' + z'\cos pt' \\ t &= t' \end{aligned}\right\} \qquad (3)$$

where the primes denote the fixed axes and $p$ is the rate of roll of the airfoil.

The flow over bodies rolling with constant velocities is independent of time; thus derivatives with respect to time in the new coordinate system are zero for the cases we shall study. It follows that the differential equation (correct to the second order) for the flow over bodies with constant $p$ is given by

$$-\beta^2\Phi_{xx} + \Phi_{yy} + \Phi_{zz} = -\frac{2pM^2}{V}(y\Phi_{xz} - z\Phi_{xy}) + M^2\left[(\gamma - 1)\Phi_x(\Phi_{xx} + \Phi_{yy} + \Phi_{zz}) + 2\Phi_x\Phi_{xx} + 2\Phi_y\Phi_{xy} + 2\Phi_z\Phi_{xz}\right] \qquad (4)$$

where $M$ is the Mach Number and $\beta^2 \equiv M^2 - 1$.

Received March 17, 1953.

* Aerodynamicist, Airflow Branch, Exterior Ballistic Laboratory.

† Mathematician, Airflow Branch, Exterior Ballistic Laboratory.

Similarly, the pressure coefficient is found to be

$$C_p = -2\left(\Phi_x + \frac{pz}{V}\Phi_y - \frac{py}{V}\Phi_z\right) - \Phi_y^2 - \Phi_z^2 + \beta^2\Phi_x^2 \quad (5)$$

## Method of Iteration

We shall assume that Eq. (4) can be solved by an iteration procedure. The solution to the first-order partial differential equation is taken as the first approximation to the solution of Eq. (4). The first-order equation, obtained by neglecting the second order terms in Eq. (4), is

$$-\beta^2\phi_{xx} + \phi_{yy} + \phi_{zz} = 0 \quad (6)$$

We assume that the second approximation can be found by substituting the first-order solution into the right side of Eq. (4) and solving the resulting nonhomogeneous equation, which from Eqs. (4) and (6) is

$$-\beta^2\psi_{xx} + \psi_{yy} + \psi_{zz} = -(2pM^2/V)(y\phi_{xz} - z\phi_{xy}) + 2M^2[(N-1)\beta^2\phi_x\phi_{xx} + \phi_y\phi_{xy} + \phi_z\phi_{xz}] \quad (7)$$

where

$$N \equiv (\gamma + 1)M^2/(2\beta^2)$$

The solution of Eq. (7) will be referred to as the second-order solution.

## Examination of Potential Form

It is helpful to investigate the type of solution obtained from Eq. (7). The first-order solution will be of the form

$$\phi = \alpha g_1(x, y, z) + pg_2(x, y, z) + \epsilon g_3(x, y, z)$$

where $\alpha$ is the angle of attack of the airfoil, $\epsilon$ is a thickness parameter, and $\alpha$, $p$, and $\epsilon$ are small compared to unity. It follows from the preceding expression and Eq. (7) that the second-order solution will be of the form

$$\psi = \alpha^2 h_1(x, y, z) + p^2 h_2(x, y, z) + \epsilon^2 h_3(x, y, z) + \alpha p h_4(x, y, z) + \alpha\epsilon h_5(x, y, z) + p\epsilon h_6(x, y, z) \quad (8)$$

The terms $\alpha^2 h_1(x, y, z)$, $\epsilon^2 h_3(x, y, z)$, and $\alpha\epsilon h_5(x, y, z)$ are independent of the rate of roll and do not contribute to the lifting pressure due to rolling motion of the airfoil.* Since the present paper is concerned only with the lifting pressure due to rolling, all terms of the form $\alpha^2 h_1$, $\epsilon^2 h_3$, and $\alpha\epsilon h_5$ can be neglected in the following analysis.

The following argument shows that $p^2 h_2(x, y, z)$ and $\alpha p h_4(x, y, z)$ do not contribute to the lifting pressure: The thickness parameter, $\epsilon$, is not present; therefore the airfoil can be considered a flat plate insofar as these terms are concerned. If the potential on the upper surface of a flat plate is expressed as

$$\Phi(\alpha, p) = \alpha g_1 + pg_2 + \alpha^2 h_1 + p^2 h_2 + \alpha p h_4$$

the potential on the lower surface is

$$\Phi(-\alpha, -p) = -\alpha g_1 - pg_2 + \alpha^2 h_1 + p^2 h_2 + \alpha p h_4$$

The potential difference is

$$\Delta\Phi = 2\alpha g_1 + 2pg_2$$

Since the lifting pressure can be found directly from $\Delta\Phi$ it follows that $p^2 h_2$ and $\alpha p h_4$ do not contribute to the lifting pressure.

The remaining term in Eq. (8) will be found by evaluating the right-hand side of Eq. (7), neglecting all expressions multiplied by $\alpha^2$, $\alpha\epsilon$, $p^2$, $\epsilon^2$, and $\alpha p$.

## Boundary Conditions

Physical considerations require that the flow be tangent to the surface and that all velocity perturbations vanish upstream of the airfoil. These boundary conditions are expressible mathematically as $\phi(x, y, z) = 0$ upstream of the airfoil and $q \cdot \nabla s = 0$, where $s(x, y, z) = 0$ is the equation of the surface of the body and $q$ is the velocity vector.

The equation of the surface of the body may also be expressed as

$$z = \epsilon f(x, y)$$

where $\epsilon$ is small compared with unity and $f(x, y)$; thus,

$$\nabla s = -i\epsilon(\partial f/\partial x) - j\epsilon(\partial f/\partial y) + k$$

Since the velocity, $q$, can be written as

$$q = i(V + V\phi_x + V\psi_x) + j(V\phi_y + V\psi_y + pz) + k(V\phi_z + V\psi_z + py)$$

it follows that the boundary condition on the body surface is

$$-(V + V\phi_x + V\psi_x)\sigma_x - (V\phi_y + V\psi_y + pz)\sigma_y + V\phi_z + V\psi_z + py = 0$$

where $\sigma_x = \epsilon(\partial f/\partial x)$ and $\sigma_y = \epsilon(\partial f/\partial y)$.

The coordinate axes will be chosen so that the airfoil lies approximately in the $z = 0$ plane. The boundary conditions for the first-order solution are $\phi(x, y, z) = 0$ upstream of the airfoil and

$$\phi_z|_{z=0} = (-py/V) + \sigma_x \quad (9)$$

Similarly, the boundary conditions for the second-order solution are $\psi = 0$ upstream of the airfoil and

$$\psi_z|_{z=0} = \sigma_x\phi_x|_{z=0} + \sigma_y\phi_y|_{z=0} - \epsilon f(x, y)\phi_{zz}|_{z=0} \quad (10)$$

For the airfoils considered here, the first-order velocity components are discontinuous across the Mach sheet from the leading edge. To evaluate the effect of the discontinuities on the second-order solution, we shall assume that the leading-edge Mach sheet has a

* These terms are associated with steady supersonic flow.

small but finite thickness within which the first-order velocity components will be made continuous. Thus the discontinuities through the Mach sheet are replaced by continuous functions. This process is illustrated in Fig. 1 for $\phi_z$ for an airfoil with leading edge perpendicular to the free stream. The effect of the discontinuities on the second-order solution will be found by obtaining the second-order solution within the Mach sheet and then letting the thickness approach zero.*

The procedure just outlined will be illustrated by considering the case of an infinite rolling rectangular airfoil having a constant initial slope, $\epsilon$, along its leading edge. Only the Mach sheet above the airfoil will be considered, since the Mach sheets above and below are of the same form. The discontinuities through the leading-edge Mach sheet depend only on the initial slope of the airfoil; therefore the discontinuities in the first-order velocity components through the Mach sheet above the airfoil will be the same as those for a flat rolling airfoil at an angle of attack of minus $\epsilon$.

The first-order potential function associated with the flow over the upper surface of an infinite rolling rectangular wing with a constant slope $\epsilon$ is

$$\phi = [(py/V) - \epsilon]\,(x - \beta z)/\beta \tag{11}$$

where the airfoil lies approximately in the $z = 0$ plane.†

The discontinuities in the first-order velocity components through the leading-edge Mach sheet above the airfoil are, from Eq. (11),

$$\begin{aligned} \Delta\phi_x &= [(py/V) - \epsilon]/\beta \\ \Delta\phi_y &= 0 \\ \Delta\phi_z &= [(-py/V) + \epsilon] \end{aligned}$$

It will be assumed that the Mach sheet has a small thickness (see Fig. 1b). The velocity components within the sheet will be defined as

$$\left.\begin{aligned} \phi_x &= [(py/V) - \epsilon]\,(x - \beta z)/(l\beta) \\ \phi_y &= 0 \\ \phi_z &= -[(py/V) - \epsilon]\,(x - \beta z)/l \end{aligned}\right\} \tag{12}$$

where $l$ is the thickness of the Mach sheet in the $x$ direction. Note that within the Mach sheet

$$-\beta^2\phi_{xx} + \phi_{yy} + \phi_{zz} = 0$$

and that the velocity components are continuous functions in the neighborhood of it.

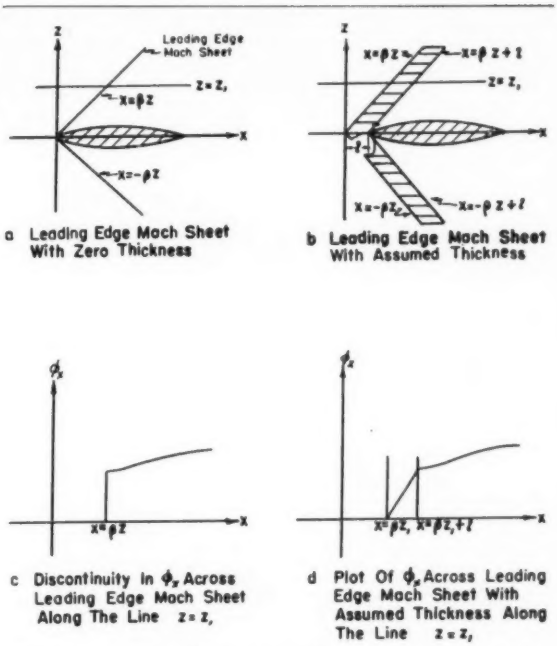
Leading Edge Mach Sheet
x=βz
z=z,
x=-βz
a Leading Edge Mach Sheet With Zero Thickness
x=βz
x=βz+l
z=z,
x=-βz+l
b Leading Edge Mach Sheet With Assumed Thickness
x=βz
c Discontinuity in φx Across Leading Edge Mach Sheet Along The Line z=z,
x=βz, x=βz+l
d Plot Of φx Across Leading Edge Mach Sheet With Assumed Thickness Along The Line z=z,

FIG. 1. An illustration of removing the discontinuity in $\phi_x$ across the leading edge Mach sheet by assuming the Mach sheet to have thickness.

From Eqs. (7) and (12) the differential equation within the Mach sheet is

$$-\beta^2\psi_{xx} + \psi_{yy} + \psi_{zz} = -\frac{2M^2p\epsilon y}{lV}\left[1 + \frac{2N(x - \beta z)}{l}\right] \tag{13}$$

It is well known [6, 7] that the solution of the nonhomogeneous equation

$$-\beta^2\psi_{xx} + \psi_{yy} + \psi_{zz} = F(x, y, z)$$

is given by

$$\psi(x, y, z) = -\frac{1}{2\pi}\int\int\int_v \frac{F(\xi, \eta, \zeta)}{R}\,d\xi\,d\eta\,d\zeta + \frac{1}{2\pi}\int^f\int_s \left(\frac{1}{R}\nabla\phi - \phi\nabla\frac{1}{R}\right)\cdot n_n\,da \tag{14}$$

where

$$R = \sqrt{(x - \xi)^2 - \beta^2(y - \eta)^2 - \beta^2(z - \zeta)^2}$$

$$\bar{n}_n = -i\beta^2\nu_1 + j\nu_2 + k\nu_3$$

$(\xi, \eta, \zeta)$ are auxiliary cartesian coordinates, $(\nu_1, \nu_2, \nu_3)$ are the direction cosines of the outward normal to the element of area $da$, $s$ is an arbitrary surface that cuts the forward Mach cone from the point $(x, y, z)$, $v$ is the volume inclosed in the forward Mach cone from the point $(x, y, z)$ and the surface $s$, and the symbol $\int^f\int$ denotes the finite part of an integral as defined by Hadamard in reference 7.

For planar problems the surface integral in Eq. (14) can be reduced to (reference 6, p. 22)

* An alternate approach would be to attach a small surface to the leading edge of the airfoil which would cause the first-order velocity components to be continuous. The effect of the discontinuities would then be evaluated by a limiting process in which the width of the small attached surface would approach zero.

† Eq. (11) can be found by the integration of a source distribution (see references 5 and 6); however, for simple problems such as this, a heuristic method generally yields the result with a minimum of effort.

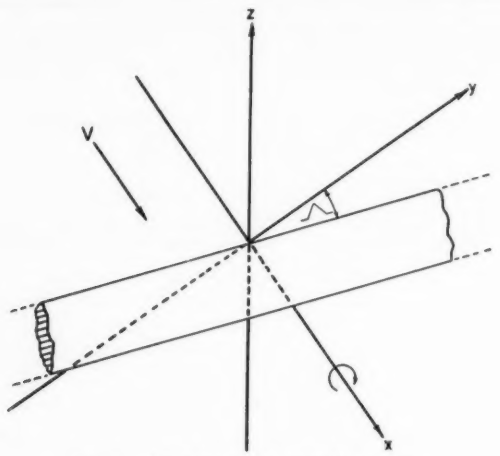


FIG. 2. Coordinates for sweptback wing.

$$\frac{1}{2\pi}\int^{f}\int\left(\frac{1}{R}\nabla\phi - \phi\nabla\frac{1}{R}\right)\cdot\bar{n}_n\,da = -\frac{1}{\pi}\int\int\frac{\phi_z(\xi,\,\eta,\,0)}{R}\,da$$

It follows that the potential function within the Mach sheet is

$$\psi(x,\,y,\,z) = \frac{M^2p\epsilon}{\pi V}\int\int\int_v\frac{\eta}{R}\left[1 + \frac{2N(\xi - \beta\zeta)}{l}\right]\times d\xi\,d\eta\,d\zeta + \frac{1}{\pi l}\int\int_{s_1}\frac{1}{R}\left(\frac{p\eta}{V} - \epsilon\right)\xi\,d\xi\,d\eta \quad (15)$$

where $s_1$ is the area of the $z = 0$ plane which is enclosed within the Mach sheet and the forward Mach cone from the point $(x, y, z)$.

To evaluate the second-order solution on the downstream side of the Mach sheet, we take $(x, y, z)$ to be an arbitrary point on the surface $x = \beta z + l$. Since the thickness of the Mach sheet is small, it follows that for given values of $\xi$ and $\zeta$ the variation of the integrands of the volume and surface integrals is made up almost completely of the variation of $1/R$. This allows the substitution of $y = \eta$ in the integrands except in $R$, and this in turn allows integration in the $\eta$ direction. Then the potential at a point $(\beta z + l, y, z)$ can be expressed as

$$\psi(\beta z + l,\,y,\,z) = \frac{M^2p\epsilon y}{l\beta}\int_0^z d\zeta\int_{\beta\zeta}^{\beta\zeta+l}\times\left[1 + \frac{2N}{l}(\xi - \beta\zeta)\right]d\xi + \frac{1}{\beta l}\left(\frac{py}{V} - \epsilon\right)\int_0^l\xi\,d\xi$$

Performing the remaining integrations and taking the limit as $l$ approaches zero yields

$$\Delta\psi\big|_{x=\beta z} = M^2(N + 1)p\epsilon yx/V\beta^2 \quad (16)$$

The value of the discontinuity in the second-order potential is given by Eq. (16) for that part of it which contributes to the lifting pressure due to the flow over a rolling airfoil with a nonsweptback leading edge of constant initial slope. Similarly, when the leading edge is swept back, the second-order discontinuity is found to be

$$\Delta\psi\big|_{mx-y-\lambda z=0} = \frac{M^2mp\epsilon}{2V\lambda^2}\left(\frac{\beta^2m^2N}{\lambda^2} + 1\right)(2\lambda y - z)z \quad (17)$$

where $m$ is the cotangent of the sweepback angle $\Lambda$ (see Fig. 2) and $\lambda = \sqrt{\beta^2m^2 - 1}$.

## SOLUTION OF DIFFERENTIAL EQUATION

Having determined the differential equation and its boundary conditions, we proceed to its solution.

The coordinate axes are chosen as indicated in Fig. 2. The equation of the upper surface is represented by

$$z = \epsilon f[(mx - y)/m] \quad (18)$$

The first-order solution is

$$\phi = \frac{p}{2V\lambda^3}(mx - y - \lambda z)\,[-mx + (2\beta^2m^2 - 1)y - \lambda z] - \frac{m}{\lambda}f\left(\frac{mx - y - \lambda z}{m}\right) \quad (19)$$

The second-order potential function must satisfy the nonhomogeneous equation (neglecting terms multiplied by $p^2$ and $\epsilon^2$)

$$-\beta^2\psi_{xx} + \psi_{yy} + \psi_{zz} = \frac{2M^2p\epsilon}{V}\left[-\left(\frac{N\beta^4m^4}{\lambda^4} + 1\right)yf'' + \frac{z}{\lambda}f'' + \frac{\beta^2m^3N}{\lambda^4}f' + \frac{N\beta^2m^3}{\lambda^4}xf''\right] \quad (20)$$

where the primes denote derivatives with respect to $[(mx - y - \lambda z)/m]$. The particular integral of Eq. (20) was chosen to be

$$\theta_1 = \frac{M^2p\epsilon}{V}\left[\frac{m}{\lambda}\left(\frac{N\beta^4m^4}{\lambda^4} + 1\right)zyf' - \frac{m}{\lambda^2}z^2f' - \frac{m^2}{\lambda^3}\left(\frac{N\beta^2m^2}{\lambda^2} + 1\right)zf - \frac{N\beta^2m^4}{\lambda^5}xzf'\right] \quad (21)$$

By inspection the complementary function, $\theta_2$, of Eq. (20) satisfying the boundary conditions [Eqs. (10) and (17)] and

$$-\beta^2(\theta_2)_{xx} + (\theta_2)_{yy} + (\theta_2)_{zz} = 0$$

is found to be

$$\theta_2 = \frac{p\epsilon}{V}\left\{\frac{M^2m}{4\lambda^4}\left(\frac{N\beta^2m^2}{\lambda^2} + 1\right)[(mx - y)^2 + \lambda^2z^2]f'(0) + \frac{m}{\lambda^3}\left(-\frac{M^2N\beta^4m^4}{\lambda^2} + 3\beta^2 + 1 - \frac{\beta^4m^4 + 1}{m^2}\right)\times\right.$$
$$\left[-\frac{m}{\lambda}\left(\frac{z}{\lambda} + y\right)f - \frac{m^2}{\lambda^3}\int_0^{(mx-y-\lambda z)/m} f(u)\,du\right] + \frac{M^2m^2}{\lambda^3}\left(\frac{N\beta^2m^2}{\lambda^2} - 1\right)\left[\left(\frac{\beta^2m^2}{\lambda^2}z - \frac{mx}{\lambda}\right)f + \right.$$
$$\left.\left.\frac{\beta^2m^3}{\lambda^3}\int_0^{(mx-y-\lambda z)/m} f(u)\,du\right] - \frac{m}{\lambda^4}\left(\frac{M^2N\beta^2m^4}{\lambda^2} + m^2 + 1\right)\int_0^{(mx-y-\lambda z)/m} f(u)\,du\right\} \quad (22)$$

The part of the potential function contributing to the lifting pressure is

$$\psi = \theta_1 + \theta_2 \quad (23)$$

From Eqs. (5), (19), and (23) the lifting pressure for symmetrical airfoils is

$$\Delta C_p = \frac{4pm}{V\lambda^3}(mx - \beta^2m^2y) - \frac{4p\epsilon M^2m^2}{V\lambda^4}\left[\frac{1}{2}\left(\frac{N\beta^2m^2}{\lambda^2} + 1\right)(mx - y)f'(0) + \left(\frac{N\beta^4m^4}{\lambda^2} - 1\right)yf' - \right.$$
$$\left.\left(\frac{N\beta^2m^2}{\lambda^2} - 1\right)mxf' - m\left(\frac{2N\beta^2m^2}{\lambda^2} + 1\right)f\right] \quad (24)$$

For unswept wings, $m = \infty$ and Eq. (24) reduces to

$$\Delta C_p = -(4py/V\beta)\,[1 + (\epsilon/\beta)M^2Nf'(x)] \quad (25)$$

Eq. (25) indicates that for the unswept wing the second-order effect is a function only of the local slope of the airfoil surface.

Eqs. (24) and (25) are linear in $\epsilon$. This leads one to inquire whether the effect of thickness is linear with regard to different types of thickness distributions for the same plan form. Suppose the equation of the surface is expressed as

$$z = \epsilon_1 f_1(x, y) + \epsilon_2 f_2(x, y)$$

The first-order solution is of the form

$$\phi = \alpha g_1(x, y, z) + pg_2(x, y, z) + \epsilon_1 g_3(x, y, z) + \epsilon_2 g_4(x, y, z)$$

The second-order solution will be of the form

$$\psi = \alpha^2 h_1(x, y, z) + p^2 h_2(x, y, z) + \epsilon_1^2 h_3(x, y, z) + \epsilon_2^2 h_7(x, y, z) +$$
$$\alpha p h_4(x, y, z) + \alpha\epsilon_1 h_5(x, y, z) + \alpha\epsilon_2 h_8(x, y, z) + p\epsilon_1 h_6(x, y, z) + p\epsilon_2 h_9(x, y, z) + \epsilon_1\epsilon_2 h_{10}(x, y, z)$$

By the same arguments as were used in the section on the form of the second-order potential function, it can be shown that only the terms $p\epsilon_1 h_6$ and $p\epsilon_2 h_9$ contribute to the lifting pressure due to rolling. It follows that the effects of thickness on the lifting pressure can be added linearly up to the second order. The linearity of thickness effects on the lifting pressure is also true for angle of attack, steady pitching, and other types of motions.

## The Damping in Roll

The damping in roll coefficient, $C_{l_p}$, can be written as

$$C_{l_p} = \lim_{p\to 0}\frac{1}{(pb/2V)Sb}\int\int_{\text{wing area}} y\Delta C_p\,dx\,dy \quad (26)$$

where $b$ is the wing span and $S$ is the wing area. Substituting Eq. (24) into Eq. (26) yields

$$C_{l_p} = -\frac{2m}{3\lambda}\left[1 + \frac{\epsilon M^2N\beta^2m^3}{\lambda^3 d}f(d)\right] \quad (27)$$

Eq. (27) indicates that the effect of thickness on the $C_{l_p}$ of an infinite swept wing with an arbitrary symmetrical thickness distribution varies directly as the thickness of the trailing edge.

Fig. 3 presents the variation of the $C_{l_p}$ with Mach Number for a 10 per cent infinite wedge for various sweepback angles. This figure indicates that the effect of thickness on the $C_{l_p}$ increases slightly with the sweepback angle.

## Concluding Remarks

It is possible to estimate fairly accurately the effect of thickness on the $C_{l_p}$ of many airfoils not considered

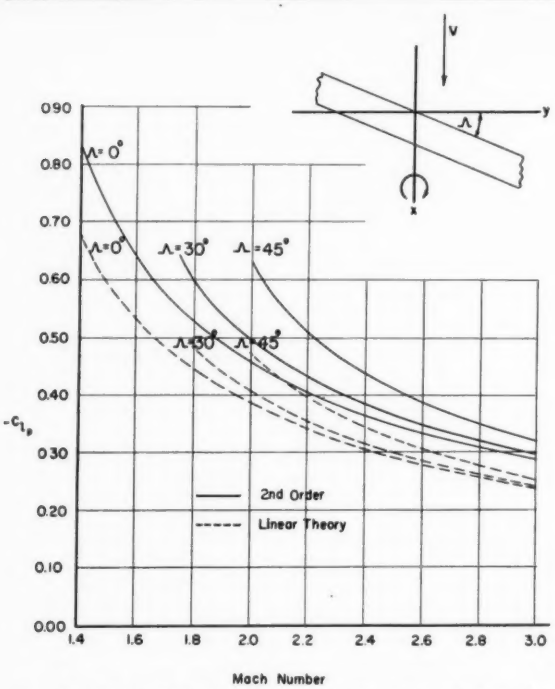


FIG. 3. The variation of the damping in roll coefficient, $C_{lp}$, with Mach number for 10 per cent thick infinite wedges for various sweepback angles.

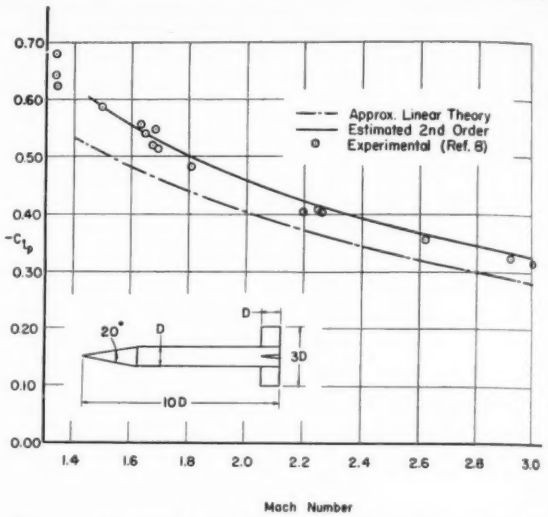


FIG. 4. A comparison of the estimated second-order damping in roll coefficient, $C_{lp}$, with experimental values for an 8 per cent thick wedge.

in the analysis. As an illustration consider the $C_{lp}$ of a rectangular airfoil with a wedge cross section such as considered in reference 8. An estimate of the effect of thickness can be made by increasing the $C_{lp}$ of the linearized theory by the same percentage as the thickness increases the $C_{lp}$ for an infinite wing. Fig. 4 presents the values of the $C_{lp}$ estimated in this manner as compared to the experimental values presented in reference 8. This figure indicates that the agreement between theory and experiment has been improved considerably.

Since the theory in this paper is closely associated with the Busemann second-order theory, it seems likely that the present results have limitations similar to those of the Busemann theory (which are treated in reference 9).

## REFERENCES

[1] Busemann, A., *Aerodynamischer Auftrieb bei Überschallgeschwindigkeit*, Atti die convegni 5, R. Acad. d'Italia, pp. 328–360, 1936. (Also printed in Luftfahrtforschung, Bd. 12, Nr. 6, Oct. 3, pp. 210–220, 1935; available in British Air Ministry Trans. No. 2844.)

[2] Van Dyke, M. D., *A Study of Second-Order Supersonic Flow Theory*, NACA TN No. 2200, 1951.

[3] Van Dyke, M. D., *First- and Second-Order Theory of Supersonic Flow Past Bodies of Revolution*, Journal of the Aeronautical Sciences, Vol. 18, No. 3, pp. 161–179, March, 1951.

[4] Rott, Nikolaus, *Das Feld einer raschbewegten Schallquelle;* Mitteilung No. 9, Inst. Aerod. Tech. H.S. Zürich, Gebr. Leeman & Co., Zürich, 1945.

[5] Puckett, Allen E., *Supersonic Wave Drag of Thin Airfoils*, Journal of the Aeronautical Sciences, Vol. 13, No. 9, pp. 475–484, September, 1946.

[6] Martin, John C., *A Vector Study of Linearized Supersonic Flow Applications to Nonplanar Problems*, NACA TN No. 2641, 1952.

[7] Hadamard, Jacques, *Lectures on Cauchy's Problem in Linear Partial Differential Equations;* Yale University Press, New Haven, 1923.

[8] Nicolaides, J. D., and Bolz, R. E., *On the Pure Rolling Motion of Winged and/or Finned Missiles in Varying Supersonic Flight*, Journal of the Aeronautical Sciences, Vol. 20, No. 3, pp. 160–168, March, 1953.

[9] Hilton, W. F., *High-Speed Aerodynamics*, pp. 237–240; Longmans, Green and Company, New York, 1951.

# A Method of Estimating the Compressive Strength of Optimum Sheet-Stiffener Panels for Arbitrary Material Properties, Skin Thickness, and Stiffener Shapes

W. R. MICKS*
*The RAND Corporation*

SUMMARY

Developed in this paper is a simple analytical method of synthesizing allowable stress curves for optimum sheet-stiffener compression panels. This method may be used with any structural material and any stiffener shape. The only material properties required in the analysis may be determined from a compression stress-strain diagram for the material being used.

Also included in the analysis are the effects of varying the relative amount of panel material allocated to the skin.

Analytical results are compared with the results of tests conducted by the NACA.

SYMBOLS

$A_z$ = area of one stringer
$A_s$ = area of skin between stringer centerlines
$b$ = stiffener spacing
$b_z$ = distance between points of attachment, measured across the stiffener cross section (see Fig. 9)
$b_s$ = distance between points of attachment, measured between stiffener cross sections (see Fig. 9)
$\rho_z$ = radius of gyration of the stiffener cross section
$\rho_T$ = radius of gyration of the sheet-stiffener combination
$t_s$ = skin thickness
$\bar{t}$ = average panel thickness (average cross-sectional area per unit width)
$(t/b)$ = thickness-width ratio for a flat plate element, in general
$x_z$ = distance from the centroid of one stiffener to the skin centerline
$k_t = t_s/\bar{t}$
$k_x = x_z/\rho_z$ shape factor measuring stiffener depth
$k_\rho = I_z/A_z{}^2 = \rho_z{}^2/A_z$ shape factor measuring bending efficiency of the stiffener cross section
$k_b$ = shape factor measuring stiffener width
$k_s = (\rho_z{}^2/A_z)(t_0/b_0)$ shape factor measuring bending efficiency of the basic stiffener shape
$k_z = \rho_T/\bar{t}$ shape factor measuring bending efficiency of the sheet-stiffener combination

## INTRODUCTION

MUCH WORK HAS BEEN DONE on design and strength testing of sheet-stiffener compression panels. Several comprehensive testing programs have been carried out to determine optimum panel configurations and to develop design charts for panels made of various types of material and having various shapes of stiffeners.[1] A separate series of tests was conducted for each different material and/or stiffener shape.

However, since new structural materials are developed from time to time, there is need for a method of estimating the strength properties of sheet-stiffener panels made of a new material, without resorting to a complete new testing program. The recent introduction of elevated temperatures into the design conditions for aircraft structures has greatly increased this need, since one of the primary effects of elevated temperature on the design of structural elements is to change the physical properties of the material.

Strength properties of compression panels are best presented and compared on a plot of allowable compressive stress, $f$, versus the structural index, $q/L_0$, for wide columns,[1, 2] where $q$ is the load per inch width and $L_0$ is the effective pin-ended column length. Shown in Fig. 1 is a plot of $f$ vs. $q/L_0$ for aluminum-alloy panels having various stiffener shapes. (This figure is reproduced from reference 2.) These curves represent the highest stresses attained in tests using the material and stiffener shape indicated on the figure. Such curves have been called "optimum" curves.

However, one important thing that such plots of the "optimum" stress have not indicated is how much of the material is in the stiffeners and how much is in the skin. This information is necessary in making a preliminary estimate of the torsional stiffness of a wing using sheet-stiffener panels. Some of the configurations corresponding to the curves of Fig. 1 tend to have a relatively small amount of material in the skin and therefore are not likely to be used in the design of a wing panel for a wing required to have high torsional stiffness. The basic parameter that indicates the relative amount of material allocated to the skin is $t_s/\bar{t}$, the ratio of skin thickness to average panel thickness.

In the actual design of a high-speed wing, a minimum allowable skin thickness is usually specified on the basis of aeroelastic effects. Therefore, any optimization of the sheet-stringer panel design should contain $t_s/\bar{t}$ as an

Received February 27, 1953.
* Head of Aircraft Structures Group.

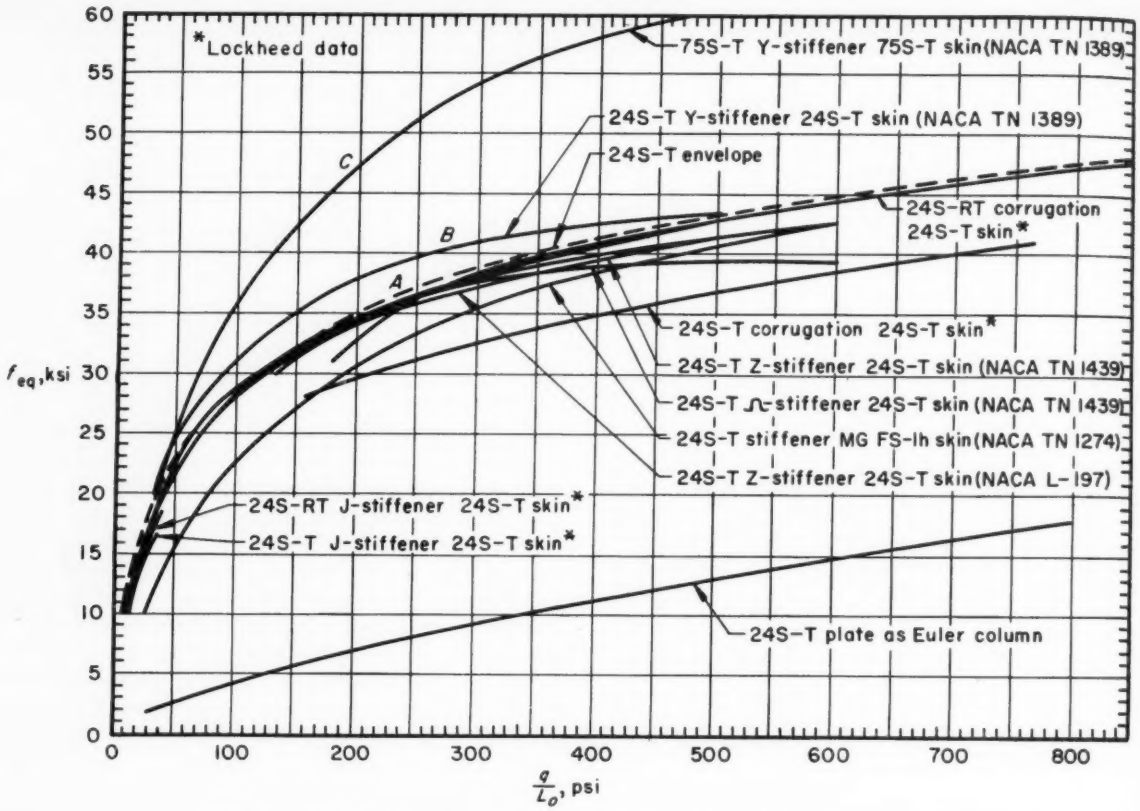


**Fig. 1—Maximum stress obtained in tests of sheet-stiffener compression panels**

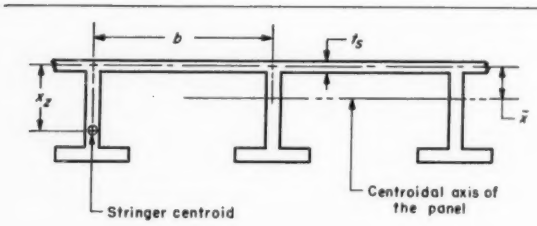


**Fig. 2—Idealized sheet-stiffener panel**

independent variable.* For this reason, a method is needed for determining the maximum allowable stress for any specified value of $t_s/l$.

The third variable that should be accounted for is the stiffener shape. It is desirable to have a method for estimating the effects of different stiffener shapes on the strength properties of sheet-stiffener panels, without conducting a complete testing program for each different shape.

The present paper develops a simple method for estimating the strength properties of optimum-designed sheet-stiffener panels (1) made of any material, (2) containing any specified fraction of the panel material in the skin, and (3) having any shape of stiffeners. The estimated strength properties from this method are compared with those obtained from tests on a plot of the $f$ vs. $q/L_0$.

The only material properties required for the analysis can be determined from a compression stress-strain diagram for the material being used.

## Cross-Sectional Shape Factor for Wide Columns

For wide columns the tangent-modulus column-buckling equation may be written in the form[2]

$$f = \pi^{2/3} E_t^{1/3} k_3^{2/3} (q/L_0)^{2/3} \qquad (1)$$

where

$q$ = load per inch width

* In an analysis of compression panels having stiffeners of uniform thickness, Zahorski[3] used the ratio of skin thickness to stiffener thickness as a parameter in expressing the relationship between the relative amount of skin and stiffener material. In the case of formed stiffeners this parameter has a definite meaning. However, for extruded stiffeners composed of elements having different thicknesses, this particular ratio is no longer applicable. It is then desirable to use the parameter $t_s/l$, which represents a slightly higher level of abstraction.

$L_0$ = effective pin-ended column length
$E_t$ = tangent modulus
$k_3$ = $\rho_T/\bar{t}$
$\rho_T$ = radius of gyration of the wide-column cross section
$\bar{t}$ = average thickness

The overall shape factor $k_3$ gives a measure of the bending efficiency of the wide-column cross section. This factor will be affected by stiffener shape and spacing, skin thickness, and other factors that determine the overall panel cross-sectional shape.

For a fixed value of structural index $q/L_0$, a measure of loading intensity,[2] an increase in the value of $k_3$ will increase the long-column buckling stress [see Eq. (1)]. However, as $k_3$ is increased, perhaps by making the stiffeners thinner and deeper, the local buckling stress is decreased. The theory of optimum design assumes that the highest allowable stress for the column will occur when the long-column stress equals the local-buckling stress. It is therefore necessary to develop an expression for $k_3$ in terms of design parameters that will be known.

As will be shown later, $k_3$ is a function of stress, material properties, and panel geometry. Substituting this function for $k_3$ in Eq. (1) will be equivalent to equating the long-column buckling stress to the local buckling stress, while also specifying a given set of boundary conditions that depend on material properties, stiffener shape, and relative skin thickness.

After the expression for $k_3$ is determined, Eq. (1) will be used to plot curves of $f$ vs. $q/L_0$ for the optimum compression panel that represents the specified boundary conditions.

## Derivation of the Expression for Shape Factor $k_3$

The shape factor $k_3$ has been defined as $k_3 = \rho_T/\bar{t}$. The following derivation gives the development of an equation that expresses $\rho_T/\bar{t}$ in terms of stiffener shape factors, the skin-thickness parameter $t_s/\bar{t}$, and the stress.

Shown in Fig. 2 is an idealized sheet-stiffener panel with dimensional notation used. The area of one stringer can be expressed

$$A_z = (\bar{t} - t_s)b \tag{2}$$

Let $k_t = t_s/\bar{t}$ and substitute for $\bar{t}$, giving stringer area as

$$A_z = t_s b(1 - k_t)/k_t \tag{3}$$

The area of skin between stringers is

$$A_s = t_s b \tag{4}$$

The distance of the panel centroid from the centerline of the skin is given by

$$\bar{x} = A_z x_z/(A_s + A_z) \tag{5}$$

Substituting for $A_z$ and $A_s$,

$$\bar{x} = x_z(1 - k_t) \tag{6}$$

The total moment of inertia $I_T$ of one bay of the panel about its centroid is

$$I_T = I_{z_0} + I_{s_0} + A_z(x_z - \bar{x})^2 + A_s\bar{x}^2 \tag{7}$$

where

$I_{z_0}$ = moment of inertia of the stringer about its centroidal axis
$I_{s_0}$ = moment of inertia of the skin element about its centroidal axis

Substitute Eqs. (3), (4), and (6) into Eq. (7) and write the moment of inertia as

$$I_T = I_{z_0} + I_{s_0} + t_s b(1 - k_t)x_z^2 k_t + t_s b x_z^2(1 - k_t)^2 \tag{8}$$

The moment of inertia of the sheet element about its centroidal axis is

$$I_{s_0} = bt_s^3/12 \tag{9}$$

The moment of inertia of the stringer about its centroidal axis may be written in the form

$$I_{z_0} = k_\rho A_z^2 \tag{10}$$

where $k_\rho = I_{z_0}/A_z^2$, which is the shape factor indicating the efficiency of the cross-sectional shape in bending. This factor $k_\rho$ is identical with the shape factor $k_1$ developed in reference 2.

Substituting Eq. (3) for $A_z$ into Eq. (10),

$$I_{z_0} = k_\rho t_s^2 b^2(1 - k_t)^2/k_t^2 \tag{11}$$

Eqs. (9) and (11) are substituted into Eq. (8) to give

$$I_T = \frac{k_\rho t_s^2 b^2(1 - k_t)^2}{k_t^2} + \frac{bt_s^3}{12} + bt_s x_z^2(1 - k_t) \tag{12}$$

The radius of gyration for the panel is

$$\rho_T = \left[\frac{I_T}{A_T}\right]^{1/2} \tag{13}$$

Since $A_T = t_s b/k_t$ and $\bar{t} = t_s/k_t$, the expression for $k_3(= \rho_T/\bar{t})$ is written as

$$k_3 = I_T^{1/2} k_t^{3/2}/t_s^{3/2} b^{1/2} \tag{14}$$

Eq. (12) is now substituted into Eq. (14) to give the expression for $k_3$,

$$k_3 = \left[\frac{k_t k_\rho b(1 - k_t)^2}{t_s} + \frac{k_t^3}{12} + \frac{x_z^2 k_t^3(1 - k_t)}{t_s^2}\right]^{1/3} \tag{15}$$

In order to express $x_z$ in nondimensional form, it is necessary to introduce a shape factor for the stiffener. Let

$$k_z = x_z/\rho_z \tag{16}$$

where $\rho_z$ = radius of gyration of the stiffener The radius of gyration of a stiffener is given by

$$\rho_z = (I_{z_0}/A_z)^{1/2} \tag{17}$$

Substituting Eqs. (11) and (3) for $I_{z_0}$ and $A_z$, respectively, into Eq. (17)

**Fig. 3—Examples of cross-sections having equal values of the shape factors $k_x$ and $k_s$**

$$\rho_z = [k_\rho t_s b(1 - k_t)/k_t]^{1/2} \tag{18}$$

The expression for $x_z$ is now obtained from Eq. (16) by substituting Eq. (18) for $\rho_z$ and solving for $x_z$.

$$x_z = k_x[k_\rho t_s b(1 - k_t)/k_t]^{1/2} \tag{19}$$

This expression for $x_z$ is now put into Eq. (15), and simplified, giving

$$k_3 = \left[\frac{k_\rho k_t(1 - k_t)^2(1 + k_x{}^2 k_t)}{t_s/b} + \frac{k_t{}^3}{12}\right]^{1/2} \tag{20}$$

where $k_\rho = \rho_z{}^2/A_z$ or $I_{z_0}/A_z{}^2$.

The next step here is to determine the relationship between $k_3$ and the local buckling stress.

Since the buckling stress of a flat-plate element is a function of the thickness-width ratio $(t/b)$ for that element, it is possible to relate $k_3$ to buckling stress through the factor $t_s/b$ of Eq. (20). However, all other factors in Eq. (20) should first be made independent of thickness-width ratio.

It can be shown that the shape factor $k_x$ is practically independent of the ratio $t/b$ of the stiffener elements if the following conditions are fulfilled while the size or thickness is being changed:

(1) The skin thickness is small relative to the depth of the stiffener.

(2) The stiffener cross section is composed of relatively thin-walled elements—i.e., the wall thicknesses are small relative to the overall dimensions of the stiffener.

(3) The ratio between values of thickness-width ratio $(t/b)$ for all of the stiffener elements is held constant while the actual value of $(t/b)$ is being changed. (This is also a necessary condition for having all stiffener elements buckle at the same stress.)

These three conditions are usually fulfilled in aircraft sheet-stiffener design over most of the range of variables. In cases where this is not true a correction factor may be derived for any particular type of configuration.

The nondimensional shape factor, $k_\rho = (\rho_z{}^2/A_z)$, is not independent of the $(t/b)$ ratio of the stiffener elements. Therefore, a new shape factor was developed for thin-walled sections which includes the bending-efficiency factor $\rho_z{}^2/A_z$ but does not vary with wall thickness. This factor, denoted by $k_s$, is defined as

$$k_s = (\rho_z{}^2/A_z)(t_0/b_0) \tag{21}$$

or

$$k_s = k_\rho(t_0/b_0) \tag{22}$$

where $t_0/b_0$ is the thickness-width ratio for a specified element of the stiffener cross section (the choice of this element is discussed later).

This factor is independent of the ratio $t/b$ of the stiffener elements if the three conditions outlined above are fulfilled.

The shape factors $k_x$ and $k_s$ were developed primarily for use with thin-walled cross sections composed of straight-line elements. However, it will be shown later that they can be applied to optimum cross sections containing a combination of straight and curved elements.

Fig. 3 shows three variations of the same basic cross-sectional shape which have the same values of $k_x$ and $k_s$.

One of the basic assumptions made in this analysis is that, for the condition of overall optimum design, all elements of the panel must buckle at the same stress.* Since no element is made overstrength, the buckling stress will equal the ultimate stress. This assumption will apply to the stiffener design, as well as the sheet-stiffener combination.

Solving Eq. (22) for $k_\rho$ and substituting into Eq. (20),

$$k_3 = \left[\frac{k_s k_t(1 - k_t)^2(1 + k_x{}^2 k_t)}{(t_s/b)(t_0/b_0)} + \frac{k_t{}^3}{12}\right]^{1/2} \tag{23}$$

In evaluating $k_s$, it is desirable to use the ratio of $t/b$ determined from a stringer element having the same edge-restraint as that of the sheet between stiffeners.† For this condition and the assumption of optimum design conditions mentioned above,

$$t_0/b_0 = t_s/b \tag{24}$$

If the stringer has no element with the same edge-restraint coefficient as the sheet elements, the use of some other stringer element gives the relation

$$t_0/b_0 = k_r(t_s/b) \tag{25}$$

where

$$k_r = \left(\frac{\text{edge-restraint coefficient of the sheet elements}}{\text{edge-restraint coefficient of the stiffener element used}}\right)^{1/2}$$

The factor $k_3$ can be expressed in terms of $(t/b)^2$ by substituting Eq. (25) into Eq. (23) to give

$$k_3 = \left[\frac{k_s k_t(1 - k_t)^2(1 + k_x{}^2 k_t)}{k_r(t_s/b)^2} + \frac{k_t{}^3}{12}\right]^{1/2} \tag{26}$$

Since the buckling stress of a flat-plate element is a function of $(t/b)^2$, the above expression for $k_3$ may be related to stress through the plate-buckling equation

* The maintenance of buckle-free conditions up to ultimate load was found to be in agreement with optimum design conditions determined by the testing program outlined in reference 4

† A discussion of edge-restraint coefficients existing at the optimum design condition is presented in Appendix (A).

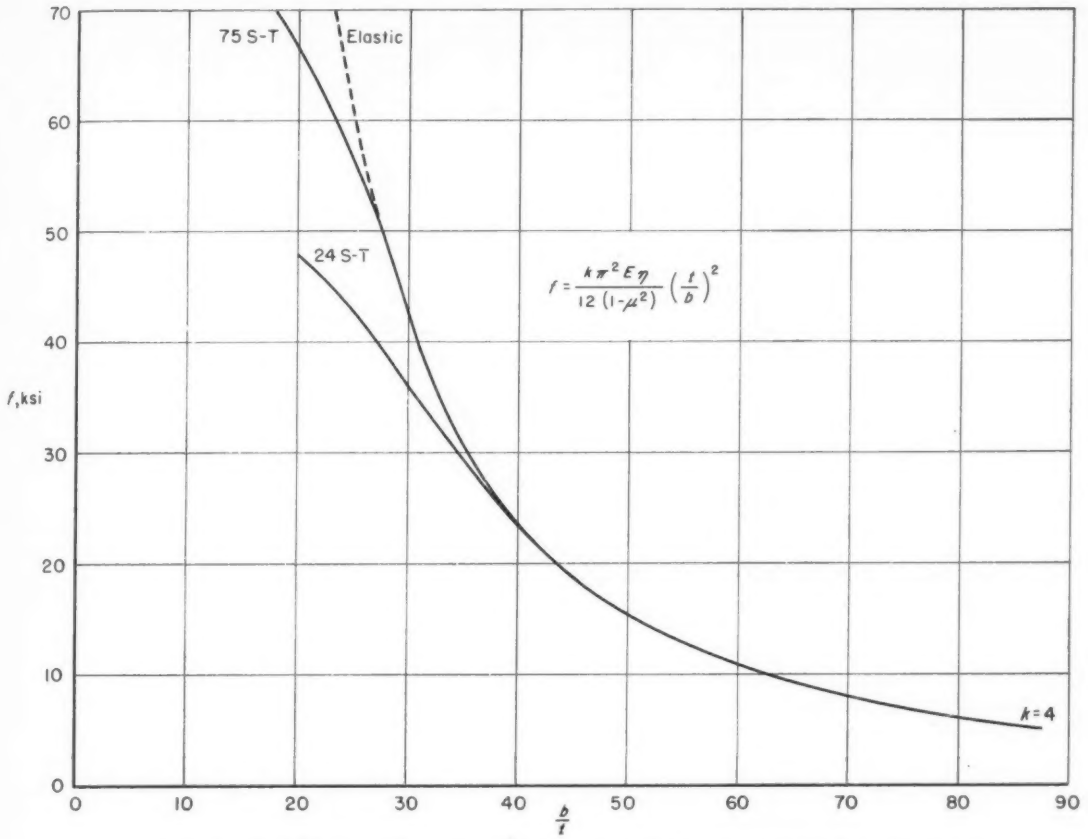


Fig. 4 – Buckling stress vs $\frac{b}{t}$ for a simply-supported flat plate of aluminum alloy

$$f_{cr} = [k\pi^2 E\eta/12(1 - \mu^2)](t/b)^2 \qquad (27)$$

where $\eta$ is the Stowell effective modulus factor (see reference 5).

The factor $k_3$ could be expressed as a function of stress by solving Eq. (27) for $(t/b)^2$ and substituting in Eq. (26) for $(t_s/b)^2$. However, it is more convenient here to use the two equations [Eqs. (26) and (27)] separately, as illustrated in the next section.

For the condition of optimum design, the local buckling stress of the panel elements must equal the long-column buckling stress. Therefore $f_{cr}$ of Eq. (27) must equal $f$ of Eq. (1), and $k_3$ can be determined as a function of $f$ for use in Eq. (1).

Since comparisons of various panel designs will be made on the basis of $f$ vs. $q/L_0$, as shown in Fig. 1, a procedure will be outlined for plotting these curves from the relation given by Eq. (1).

The example curves used to illustrate this procedure are for 24S-T aluminum-alloy panels having Z stiffeners. The shape parameters are based on the Z-section used in references 1 and 4 (flange length = 0.4 web length), and have the values given in Table 1 of this report.

### Procedure Used in Obtaining Final Curves

For the material chosen, a curve is plotted from Eq. (27) giving $f$ vs. $b/t$. Such a curve is shown in Fig. 4 for two types of aluminum alloy. (Constants used in plotting Fig. 4 are $k = 4$, $\mu = 0.3$, and $E = 10.5 \times 10^6$ lbs. per sq.in. For 24S-T material the values for $\eta$ were taken from reference 5. The values of $\eta$ for the 75S-T material were computed from stress-strain test data of reference 6.)

Values of the shape factors $k_x$ and $k_s$ are determined for the basic stiffener shape being investigated. Then $k_3$ can be determined as a function of stress; $k_t$, by use of Eqs. (26) and (27). It is assumed here that the sheet between stiffeners is simply supported at the edges. Therefore, a value of $k_r = 1.00$ was used.

Fig. 5 shows how the local buckling stress varies with $k_3$ for several values of skin-thickness parameter $k_t$.

Fig. 6 shows a plot of $k_3$ vs. $k_t$ for a constant value of stress equal to 40,000 lbs. per sq.in. When $k_t$ equals unity, all of the panel material is in the skin. As $k_t$ is decreased, while holding $f$ constant, material must be taken from the skin and put into the stiffeners.

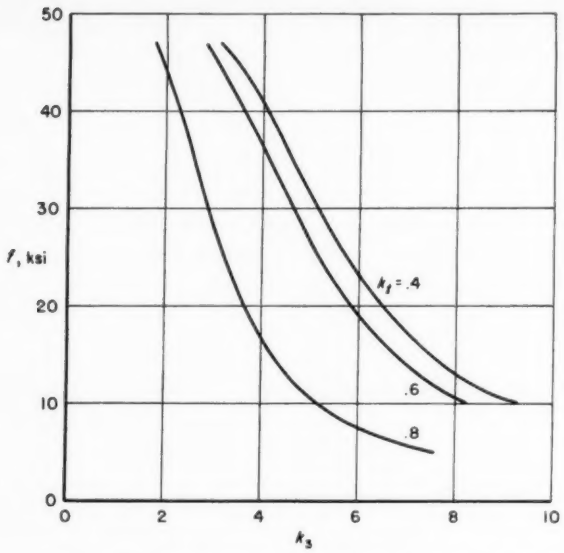


Fig. 5—Stress vs $k_3$ for 24S-T Z-stiffener compression panels of optimum proportions

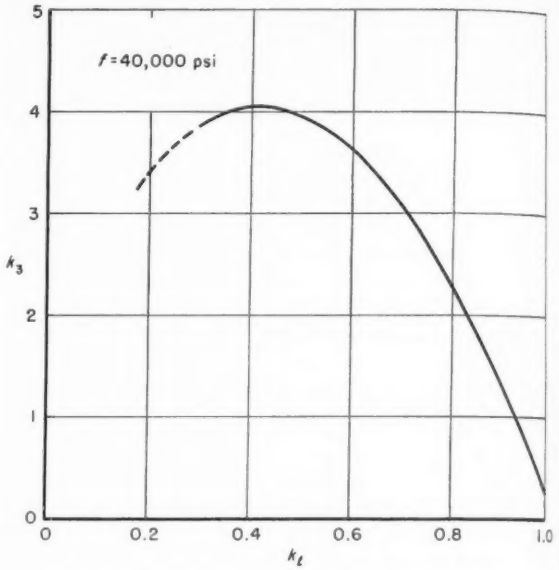


Fig. 6—Variation of $k_3$ with $k_t$ for 24S-T Z-stiffener panels ($f$=40,000 psi)

It is interesting to note that, as the value of $k_t$ is decreased from unity, $k_3$ reaches a maximum value and then drops off again as still more material is transferred from the skin to the stiffeners.

As the value of $k_t$ is decreased toward zero, while holding the stress constant, the stiffener spacing will tend to approach zero. Therefore the actual width of the stiffener would place a lower limit on the value of $k_t$. However, it would be impractical to design a panel for a value of $k_t$ below that which gives the maximum value of $k_3$.

Although the end point of the curve at $k_t = 1.0$ is established, a portion of the curve for relatively large values of $k_t$ (say, $k_t > 0.8$) may tend to be somewhat too high, since there is doubt that the resulting stiffeners in this range will have sufficient stiffness to stabilize the sheet and produce the simply supported edge conditions. This would, in turn, make the curves of $f$ vs. $q/L_0$ too high for these same values of $k_t$. This effect could be accounted for by a more elaborate version of the analysis made here. However, a few check tests would still have to be made in order to verify the results. It is unlikely, however, that any designs would be made at either extreme of the range of $k_t$.

The value of $k_t$ giving maximum allowable stress will vary somewhat with the stiffener shape used (see example curves for Y-stiffeners). For the material being used, the relation between tangent modulus and stress may be shown by a curve such as Fig. 7, which is reproduced from reference 3.

Solving Eq. (1) for $q/L_0$ and using $E_t = \tau E$ gives the expression

$$q/L_0 = f^{3/2}/\pi E^{1/2}\tau^{1/2}k_3 \qquad (28)$$

For any value of $f$ chosen, we can determine corresponding values of $k_3$ and $\tau$ from Figs. 5 and 7, respectively. Substitution of these values into Eq. (28) gives a corresponding value of $q/L_0$. Then plotting $f$ vs. $q/L_0$ results in curves as shown in Fig. 8. The highest curve shown is that corresponding to the maximum value of $k_3$ (see Fig. 6).

## Comparison of Results

The dashed line of Fig. 8 represents the "optimum" curve obtained by tests as described in reference 1. It can be seen that this curve lies fairly close to the highest curve obtained by the present method. Possible sources of difference are:

(*a*) *Difference in material properties:* The curves obtained by the present method are based on "nominal" properties of 24S-T aluminum alloy taken from Figs. 4 and 7. If the tangent-modulus curve of the 24S-T material used in the tests differs from the values used here, particularly in the yield region, the $f$ vs. $q/L_0$ curves will be affected accordingly.

(*b*) *Shape factors:* In deriving the $f$ vs. $q/L_0$ curves by the present method, the shape factors were assumed to be constant over the entire range of loading. This condition was probably not exactly fulfilled in the tests.

(*c*) *Differences in end-restraint conditions:* It is likely that the edge-restraint conditions for elements of the test specimens were somewhat different from the condition assumed here, particularly if some of the panel elements buckled before the maximum load was reached. However, it has been assumed here that, for optimum design, all of the panel elements buckle simultaneously. When this condition is fulfilled, edge-re-

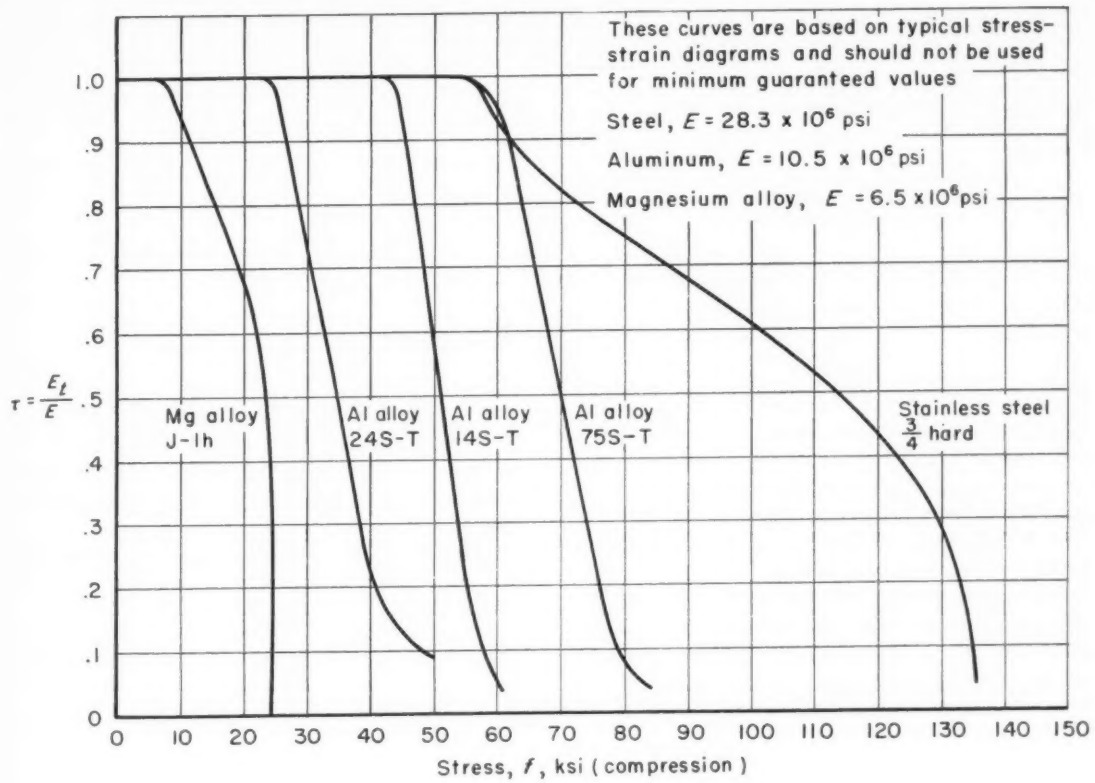
These curves are based on typical stress-strain diagrams and should not be used for minimum guaranteed values
Steel, E = 28.3 x 10^6 psi
Aluminum, E = 10.5 x 10^6 psi
Magnesium alloy, E = 6.5 x 10^6 psi
τ = Et/E
Mg alloy J-1h
Al alloy 24S-T
Al alloy 14S-T
Al alloy 75S-T
Stainless steel 3/4 hard
Stress, f, ksi (compression)

Fig. 7 — Variation of tangent modulus with stress—typical values

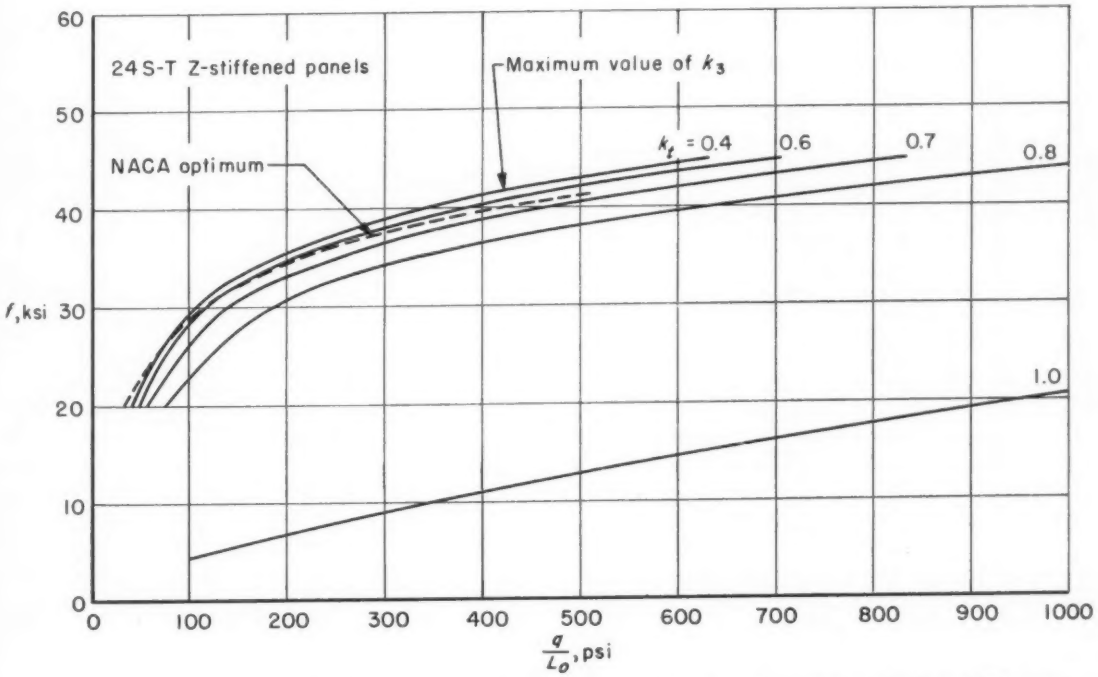


Fig. 8 — Allowable stress vs structural index for 24S-T Z-stiffener compression panels having optimum proportions

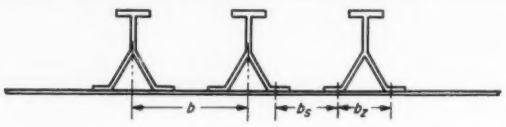


Fig. 9—Additional symbols used for two points of attachment

straint coefficients seem to vary only slightly from the theoretical values for simple edge support [see Appendix (A)].

### Stiffeners Having Two Points of Attachment

The first portion of this paper dealt with the case having the stringer attached at only one point. However, since many stiffener shapes are attached at two points, the analysis is extended to cover this case.

The sketch shown in Fig. 9 gives the nomenclature used for two points of attachment.

It can be seen that if the spacing $b_s$ is not equal to $b_z$, the two elements of sheet will not buckle at the same stress. Because of practical considerations in fabrication, we will deal only with the case where $b_s \geqq b_z$.

The stiffener spacing can be written

$$b = b_z + b_s \tag{29}$$

Substituting Eq. (29) into Eq. (20) gives the expression for $k_3$ as

$$k_3 = \left[\frac{k_\rho k_t(1-k_t)^2(1+k_x^2 k_t)}{t_s/b_s} + \frac{k_\rho k_t(1-k_t^2)(1+k_x^2 k_t)}{t_s/b_z} + \frac{k_t^3}{12}\right]^{1/2} \tag{30}$$

Expressing $t_s/b_z$ in terms of $t_s/b_s$ gives the relationship

$$\frac{b_z}{t_s} = \frac{1}{2}\left(\frac{b_s}{t_s}\right)[R + (R^2+R)^{1/2}] \tag{31}$$

where

$$R = k_s k_0^2(1-k_t)/k_t$$
$$k_b = b_z/\rho_z$$

The factor $k_b$ is a stiffener shape factor that describes the distance between points of attachment. This factor is independent of the ratio $t/b$ for the stiffener elements, subject to the three conditions listed previously.

Substituting Eq. (31) into Eq. (30) and simplifying gives the expression

$$k_3 = \left[\frac{k_\rho k_t(1-k_t)^2(1+k_x^2 k_t)(1/2)[2+R+(R^2+R)^{1/2}]}{t_s/b_s} + \frac{k_t^3}{12}\right]^{1/2} \tag{32}$$

Since it has been specified that the sheet between stiffeners must buckle at the same stress as the stiffener

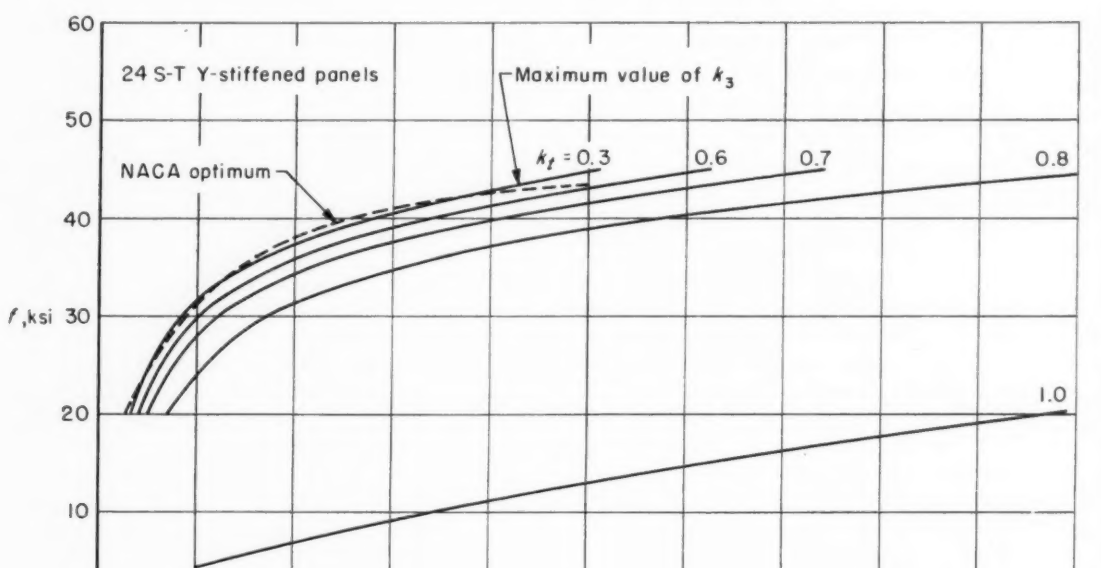


Fig. 10—Allowable stress vs structural index for 24 S-T Y-stiffener compression panels having optimum proportions

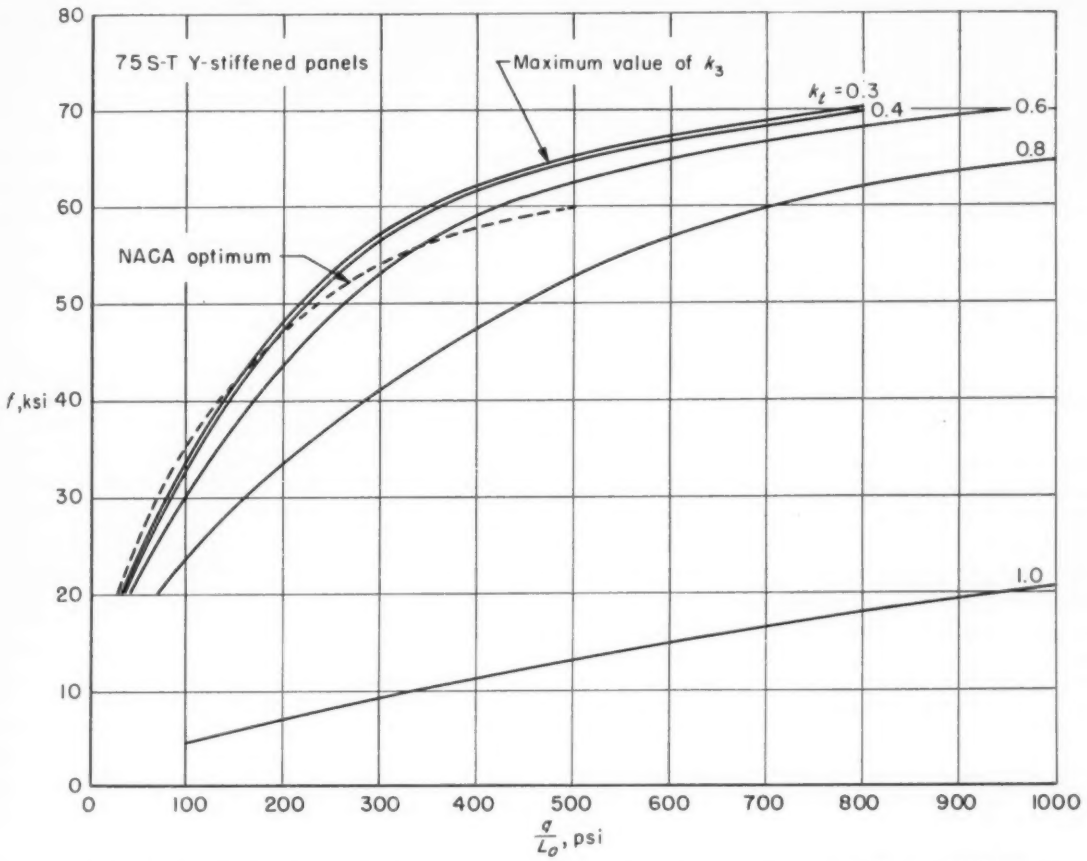


Fig. 11—Allowable stress vs structural index for 75 S-T Y-stiffener compression panels having optimum proportions

elements, Eqs. (22) and (25) are substituted into Eq. (32) to give

$$k_3 = \left[\frac{k_s k_t (1-k_t)^2 (1+k_z^2 k_t)(1/2)[2+R+(R^2+R)^{1/2}]}{k_r (t_s/b_s)^2} + \frac{k_t^3}{12}\right]^{1/2} \quad (33)$$

This expression is used in the same way as before in obtaining the final curves of $f$ vs. $q/L_0$.

Shown in Fig. 10 are the final curves obtained by using Eq. (33) and Fig. 4, together with the shape factors for the Y-stiffener as listed in Table 1. The "optimum" test curve was taken from reference 1.

The ratio of sheet width $b_z$ under the stiffener (see Fig. 9) to sheet width $b_s$ between stiffeners can be obtained by solving Eq. (31) for $b_z/b_s$.

$$b_z/b_s = (1/2)[R + (R^2+R)^{1/2}] \quad (34)$$

For any specified value of $t_s/l$, the parameter $k_3$ will have its greatest value when $b_z/b_s$ equals unity. For any value of $b_z/b_s$ less than unity, the sheet element under the stiffener will not be stressed to its buckling load, thus introducing a source of inefficiency. The condition where $b_z$ is greater than $b_s$ has not been considered here because of practical considerations in design and fabrication.

TABLE 1
Stiffener Shape Factors

| | $k_s$ | $k_r$ | $k_b$ |
|---|---|---|---|
| Straight-Y | 0.0935 | 1.33 | 1.48 |
| Curved-Y | 0.109 | 1.34 | 1.48 |
| Z | 0.089 | 1.36 | ... |

For the Y-stiffener panel, the highest curve of $f$ vs. $q/L_0$ is obtained when $t_s/l = 0.3$.

In the case of the 75S-T Y-stiffener panel, the sheet material and the extruded stiffeners have somewhat different material properties. No attempt has been made here to account for this difference in plotting the curves of Fig. 11 for 75S-T Y-stiffener panels. The relationship between $f$ and $b/t$ given in Fig. 4 for "nominal" 75S-T material was used in the computations.

**Fig. 12— Y-stiffener sections designed by the NACA**

### Effect of Improving the Efficiency of the Stiffener Cross Section

Following the test program conducted by the NACA on Y-stiffeners having straight webs, some work was done on a more efficient cross section having curved webs,[7] which is shown in Fig. 12(b).

In using the present method with a stiffener section having a combination of straight and curved elements, it is necessary only to use the thickness-width ratio of the straight element in evaluating $k_s$ and assume that, if the stiffener is efficiently designed, the curved portion will buckle at the same stress as the straight portion.

Comparison of the values of $k_s$ in Table 1 show the curved web is somewhat more efficient than the straight webs. Therefore the curve of $f$ vs. $q/L_0$ for the curved-web Y-stiffener will lie above that of the straight-web Y-stiffener. Fig. 13, comparing the highest allowable stress curves for these two stiffener shapes, illustrates the effect of improving the stiffener efficiency by the amount shown in Table 1. The dashed lines represent curves derived by the NACA from test results on these two sections.[7] It can be seen that the amount of improvement obtained from the curved web is about the same for the analytical curves as for the curves based on tests, although the absolute values of stress do not agree exactly.

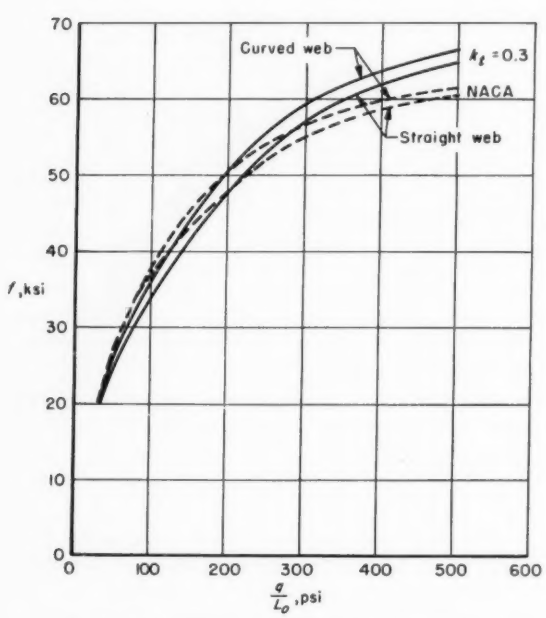


**Fig. 13— Comparison of allowable stress for 75 S-T sheet-stiffener compression panels having straight-web and curved-web Y-stiffeners**

### Conclusions

The present paper outlines a simple method for synthesizing allowable stress curves for sheet-stiffener compression panels of optimum design. As shown in Figs. 8, 10, and 11, these curves closely approximate corresponding curves that have been obtained from tests.

The basic method outlined here can be used to evaluate quickly, simply, and inexpensively the merits of any new structural material considered for use in sheet-stiffener wing panels. The only material properties required are those that can be derived from a compression stress-strain diagram for the material.

The synthesized curves are more general than the "optimum" curves based on tests, because they can be made to show the effect of varying the relative amount of skin material. This leads to a method of evaluating structural weight penalties associated with increased skin thickness.

It appears that with the aid of a few carefully designed tests the present method could replace much of the testing work ordinarily done in the investigation of the strength properties of sheet-stiffener panels. This is particularly true when design curves have already been determined for a given material and stiffener shape and it is desired to evaluate the effect of changing the material or the shape of the stiffener.

The stiffener shape factors developed for this analysis may be of value in the design of improved stiffener sections, since they furnish a simple criterion by which the efficiency of new shapes can be quickly and easily checked.

### Appendix (A)—Edge-Restraint Coefficients for Optimum Design Conditions

It may be desirable to include a brief discussion on how optimum design principles apply to the question of edge-restraint of the different flat-plate elements of a panel cross section and to the interaction between adjacent elements at the buckling load. This discussion deals with sheet-stiffener panels composed of flat-plate elements attached along one or both of the unloaded edges.

Reference 8 presents charts showing computed values of edge-restraint coefficient $k$ of the plate-buckling equation [see Eq. (27)] for the individual flat-plate elements

of several thin-walled shapes—namely, the I-section, channel, Z-section, and a rectangular section. These charts illustrate how the effective value of $k$ changes when the proportions of the cross section are changed. The relative values of $t/b$ of the elements are varied from the condition where the outstanding flanges buckle first (and are restrained by the web) to the condition where the web tends to buckle first and is restrained by the flanges. The parameters plotted are $k$ vs. $b_W/b_F$ for constant values of $t_F/t_W$. The subscript $F$ denotes an outstanding flange (supported along one edge) and $W$ denotes the web (supported along two edges).

These charts are of value in determining the conditions of edge-restraint which exist at the optimum design condition, wherein all elements buckle at the same stress. It might be thought that, because the web and flange elements tend to buckle in waves of different length, mutual restraint between adjacent elements might appreciably affect the value of $k$ when the relative size of the webs and flanges is changed (while keeping the relative values of $t/b$ the same). However, it appears that there is little interaction between the webs and the flanges at the optimum design condition.

Fig. 5 of reference 8 gives values of $k$ for the individual elements of a hollow rectangular cross section. For the condition of equal values of $t/b$ for the sides and ends, the effective edge-restraint coefficient $k$ was nearly equal to 4.0 for all of the individual elements over the entire applicable range of variables. This clearly indicates an effective end-restraint of simple support at the optimum design condition with little or no interaction between the ends and the sides, even though they have different wall thicknesses and/or lengths.

To check the value of $k$ for the other shapes, the following method was used: First, values of $k = 4.0$ and $k = 0.525$* were assumed for the webs and flanges, respectively. This defined the relative values of $t/b$ for the flat-plate elements as

$$(t_F/b_F)/(t_W/b_W) = \sqrt{k_W/k_F} = 2.76$$

for optimum proportions. Plotting lines representing this geometry on the charts of Figs. 1 through 4 of reference 8 showed that the effective values of $k_F$ and $k_W$ were practically equal to the assumed values over the entire applicable range of variables, thus indicating that at the optimum design condition the effect of interaction between the individual elements was negligible, at least for purposes of this simplified analysis.

The value of $k$ used for the webs is the theoretical value for simply supported edges,[9] while the value used for the flanges is somewhat higher than the theoretical value.*

Since the sheet is supported along two edges with closely spaced rivets, the condition of simple edge support has been assumed for the sheet in the example calculations. This gives a value of $k_r = 1.00$.

* The value of $k = 0.525$ for outstanding flanges was determined indirectly from Fig. 2 of reference 8. By assuming that $k = 4.0$ for the web and then working backwards, it was possible to determine what the value of $k_F$ should be in order to remain constant while values of the plotted parameters $b_W/b_F$ and $t_W/t_F$ were changed [and while keeping $(t_F/b_F)/(t_W/b_W)$ constant, as explained above]. That such a value existed is considered sufficient justification for the assumptions made in the body of the paper regarding optimum design configurations.

## References


[1] Dow, Norris F., and Hickman, William A., *Design Charts for Flat Compression Panels Having Longitudinal Extruded Y-Section Stiffeners and Comparison with Panels Having Formed Z-Section Stiffeners*, NACA TN No. 1389, August, 1947.

[2] Shanley, F. R., *Principles of Structural Design for Minimum Weight*, Journal of the Aeronautical Sciences, Vol. 16, No. 3, p. 133, March, 1949.

[3] Zahorski, Adam, *Effect of Material Distribution on Strength of Panels*, Journal of the Aeronautical Sciences, Vol. 11, No. 3, p. 247, July, 1944.

[4] Schuette, Evan H., *Charts for the Minimum-Weight Design of 24S-T Aluminum-Alloy Flat Compression Panels with Longitudinal Z-Section Stiffeners*, NACA Report No. 827, 1945.

[5] Stowell, E. Z., *A Unified Theory of Plastic Buckling of Columns and Plates*, NACA Report No. 898, 1948.

[6] Miller, James A., *Stress-Strain and Elongation Graphs for Alclad Aluminum-Alloy 75S-T*, NACA TN No. 1385, November, 1947.

[7] Dow, Norris F., and Hickman, William A., *Comparison of the Structural Efficiency of Panels Having Straight-Web and Curved-Web Y-Section Stiffeners*, NACA T.N. No. 1787, January, 1949.

[8] Kroll, W. D., Fisher, Gordon P., and Heimerl, George J., *Charts for Calculation of the Critical Stress for Local Instability of Columns with I-, Z-, Channel, and Rectangular-Tube Section*, NACA WR L-429, November, 1943.

[9] Timoshenko, S., *Theory of Elastic Stability;* McGraw-Hill Book Company, Inc., New York, 1936.

# Readers' Forum

*BRIEF REPORTS of investigations in the aeronautical sciences and discussions of papers published in the JOURNAL are presented in this special department. Publication will be completed as soon as possible after receipt of the material. The Editorial Committee does not hold itself responsible for the opinions expressed by the correspondents. Contributions should not exceed 800 words in length.*

## On Similarity of Thermal Stresses in Elastic Bodies

Martin Lessen
*Professor of Aeronautical Engineering, The Pennsylvania State College, State College, Pa.*
June 3, 1953

IF THERE EXISTED geometrically similar model and prototype, what criterion would exist for a similitude of thermal stresses in model and prototype? This question can be answered by a consideration of the relevant dimensionless equations.

The dimensional equations for an isotropic thermally conducting elastic solid may be given in Cartesian form as follows:

*Equilibrium*

$$\partial\tau_{ij}/\partial x_j = 0$$

*Stress-Strain*

$$\epsilon_{ij} = [(1+\nu)/E]\,\tau_{ij} - (\nu/E)\,\tau_{kk}\delta_{ij} + \alpha(T - T_0)\delta_{ij}$$

*Energy*

$$\rho(\partial U/\partial t) = K(\partial^2 T/\partial x_m \partial x_m)$$

*State*

$$U - U_0 = \gamma(T - T_0) + \lambda(\epsilon_{kk} - \epsilon_{kk_0})$$

where

| | | |
|---|---|---|
| $\tau_{ij}$ | = | stress tensor |
| $x_j$ | = | space coordinate |
| $\epsilon_{ij}$ | = | strain tensor |
| $\nu$ | = | Poisson's ratio (isothermal) |
| $E$ | = | Young's modulus (isothermal) |
| $\alpha$ | = | thermal coefficient of expansion |
| $T$ | = | temperature |
| $T_0$ | = | reference (original) body temperature |
| $\rho$ | = | density |
| $U$ | = | internal energy per unit mass |
| $t$ | = | time coordinate |
| $K$ | = | thermal conductivity |
| $U_0$ | = | reference internal energy at $T_0$ and $\epsilon_{kk_0}$ |
| $\gamma$ | = | thermodynamic property corresponding to specific heat at constant strain |
| $\lambda$ | = | thermodynamic property defined later |
| $\epsilon_{kk_0}$ | = | reference (original) strain taken as equal to zero |

The equilibrium equation neglects the effect of body forces; it is assumed that the inertia effects are small. The stress-strain equation contains the effects of temperature change. The energy equation is a statement of the first law of thermodynamics in which the work term is eliminated by linearization. The state equation is obtained from the linear terms of a Taylor series expansion about the reference state as follows:

$$U = U(T, \epsilon_{ij})$$

$$U = U_0 + (T - T_0)\left(\frac{\partial U}{\partial T}\right)_{\substack{T = T_0 \\ \epsilon_{ij} = \epsilon_{ij_0}}} + (\epsilon_{ij} - \epsilon_{ij_0})\left(\frac{\partial U}{\partial \epsilon_{ij}}\right)_{\substack{T = T_0 \\ \epsilon_{ij} = \epsilon_{ij_0}}} + \text{higher order terms}$$

Let

$$\partial U/\partial T = \gamma, \qquad \partial U/\partial \epsilon_{ij} = \lambda_{ij}$$

If the material is isotropic, $\lambda_{ij} = \lambda\delta_{ij}$. Therefore, $U - U_0 = \gamma(T - T_0) + \lambda(\epsilon_{kk} - \epsilon_{kk_0})$

The following scaling transformation is then made:

$$\begin{aligned} \tau_{ij} &= E\alpha(T_1 - T_0)\tau_{ij}' \\ \epsilon_{ij} &= \alpha(T_1 - T_0)\epsilon_{ij}' \\ T - T_0 &= (T_1 - T_0)T' \\ x_i &= l x_i' \\ t &= \sigma t' \end{aligned}$$

where $T_1$ = surrounding temperature that the body is exposed to, $l$ = characteristic length scale, and $\sigma$ = characteristic time scale.

If the state equation is substituted in the energy equation, the resulting dimensionless equations (with all primes dropped) follow: *Equilibrium*

$$\partial\tau_{ij}/\partial x_j = 0$$

*Stress-Strain*

$$\epsilon_{ij} = (1+\nu)\tau_{ij} - \nu\tau_{kk}\delta_{ij} + T\delta_{ij}$$

*Energy*

$$\frac{\partial}{\partial t}\left(T + \frac{\lambda\alpha}{\gamma}\,\epsilon_{kk}\right) = \frac{K\sigma}{\rho\gamma l^2}\,\frac{\partial^2 T}{\partial x_m\,\partial x_m}$$

The time scale, $\sigma$, can be adjusted to keep the coefficient $K\sigma/\rho\gamma l^2$ constant. The remaining conditions to be satisfied for similarity are that $\nu$ and $\lambda\alpha/\gamma$ be constant.

For most metals in the elastic range, $\nu$ is almost constant and equal to about 0.3. It can be shown,* using the Maxwell relations, that

$$\frac{\lambda\alpha}{\gamma} = \frac{E_s - E}{E_s}\,\frac{1}{(1-2\nu)}\,\frac{\beta}{\gamma}$$

where $E_s$ = Young's modulus (adiabatic) and $\beta$ = specific heat at constant stress.

For aluminum (and most metals)

$$\lambda\alpha/\gamma = 0(0.01)$$

It, therefore, seems reasonable to neglect the effect of $\lambda\alpha/\gamma$ in the energy equation and to arrive at the conclusion that simi-

* Duke, C. E., *Analysis of Damping in Elastic Solids*, Doctorate Dissertation, Aeronautical Engineering Department, The Pennsylvania State College, December, 1952.

larity of thermal stresses exists for elastic metal bodies of similar geometry.

A conclusion from the foregoing considerations is that, if a model and prototype of the same material are submitted to the same thermal excitation, the corresponding thermal stresses will be the same but the time scale of the thermal stress history will vary as the square of the linear dimension scale.

## Discrete Vortex Systems in the Transition Range of Fully Developed Flow in a Pipe

J. R. Weske and A. H. Plantholt
*The Johns Hopkins University and Consolidated Gas Electric Light and Power Company of Baltimore, Respectively*

June 1, 1953

AVAILABLE RESULTS OF STUDIES of the transitions from fully developed laminar to turbulent flow in straight pipes (see, e.g., reference 1, frontispiece) do not give a satisfactory insight into the details of the process by which the original unidirectional (peripheral) vorticity of laminar flow is augmented and transformed to create the omnidirectional vorticity distribution encountered in turbulent flow. Further study of this process, undertaken by the junior author as a subject for an M.S. thesis, was influenced by the study of Theodorsen's paper[2] and by conversations with its author. Observations were made of the motion of discrete vortex systems generated in the fluid which results from interaction of these vortices and the surrounding rotational stream. It was recognized that the "Magnus effect" plays an important role in this interaction. When applied to an elementary vortex filament in rotational flow this effect may be defined by the Kutta-Joukowski theorem as follows for the two-dimensional case (Fig. 1):

$$df = \rho(\xi_F - \xi_0) V_{rel.}\, dA \tag{1}$$

where

$\xi_F$ = vorticity in the elementary cross-sectional area $dA$ of the vortex filament
$\xi_0$ = vorticity of the ambient field at the filament
$V_{rel.}$ = $(V_F - V_0)$, velocity of the vortex filament relative to the ambient fluid
$df$ = force of interaction between vortex filament and ambient fluid, normal to the vorticity and the velocity vector

If $\xi_F > \xi_0$, $df$ is positive.
If $\xi_F < \xi_0$, $df$ is negative.
If $\xi_F = \xi_0$, the force is zero.

The case $\xi_F = 0$, $\xi_0 \neq 0$ which merits special treatment will not be discussed here, since it does not pertain to a discrete vortex system.

In a real fluid, a vortex moving relative to the ambient fluid experiences a drag in addition to the above lift force. Acceleration of the vortex with respect to the ambient fluid tends to reduce the difference $(V_F - V_0) = V_{rel.}$ to zero. This tendency is counteracted if, by displacement of the vortex along a positive velocity gradient, $|V_0|$ is increased. For conditions of a real fluid according to Fig. 1, displacement in the $+y$ direction should produce a larger $V_{rel.}$ than a corresponding displacement in the opposite direction.

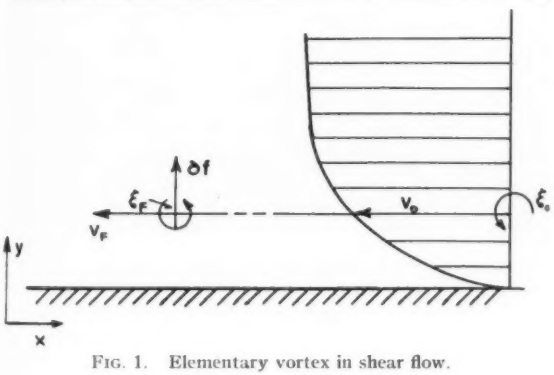


FIG. 1. Elementary vortex in shear flow.

Likewise, in a real fluid, the circulation $d\Gamma = \xi_F dA$ varies with time, and for constant $dA$, the vorticity $\xi_F$ tends to approach the value of the ambient vorticity $\xi_0$. If, for $\xi_F > \xi_0$, the vortex filament is displaced laterally in direction of a negative gradient of vorticity $\xi_0$, which is the case in Fig. 1 for displacement in the $+y$ direction, then $\xi_0$ also decreases with $+y$ and $(\xi_F - \xi_0)$ may remain positive over a longer period. The rate of decay of vorticity of a discrete vortex filament relative to the rate of its displacement along a gradient of vorticity of the ambient fluid clearly is a function of the Reynolds Number of the vortex filament. This relationship, however, will not be defined further here. Decrease of the cross-sectional area $dA$ at constant circulation $d\Gamma$ of the vortex filament through stretching (see below) will also increase the product $(\xi_F - \xi_0)dA$, since the distributed vorticity $\xi_0$ of the ambient fluid is constant with variation of $dA$.

To maintain relative motion between vortex filament and ambient fluid in a real fluid there must be a reaction force, in addition to D'Alembert's inertia force, to counteract the aforesaid lift and drag forces. This reaction is supplied by the component in the $x$-$y$ plane, Fig. 1, of the tension force in the vortex filament. Consequently, the vortex filament must be three-dimensional. For an ideal elementary vortex filament of radius $r$ and of circulation $\Gamma = \xi_F \pi r^2$, Fig. 2, the tension force created by static pressure $T = dA\,(\Delta p_{max.}/2)$ is

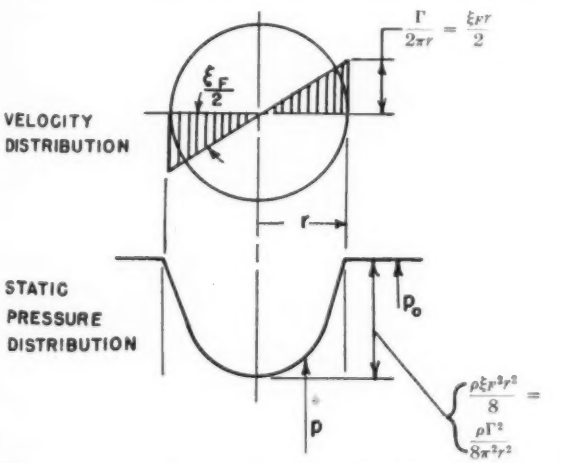


FIG. 2. Pressure and velocity distribution in an ideal elementary vortex filament.

$$T = (\rho/16\pi)\Gamma^2 \tag{2}$$

which, for constant circulation along the filament remains the same irrespective of the amount of stretching imposed upon the filament.

The work of stretching a vortex filament, disregarding fluid friction, equals the increase of the energy of the vortex filament

$$dT \cdot \Delta l = \Delta\,[(\rho I_p/2)\,(\xi_F/2)^2 \cdot l] = (\rho/16\pi)\,\Gamma^2 \Delta l \tag{3}$$

where $I_p = \pi r^4/2$ is the polar moment of inertia, $l$ is the length of the filament, and $\Delta l$ is the elongation through stretching. This equation describes the important process of conversion of energy of mean motion of flow into energy of motion of discrete vortex filaments.

In order to show that the above relationships are pertinent to the process of converting the unidirectional vorticity distribution that exists in laminar flow into the omnidirectional vorticity distribution of turbulent flow, the motion of discrete vortex filaments was observed and recorded experimentally in the following manner.

The experiments were made with water in a straight pipe of $1^5/_8$ in. inside diameter in a section made of a clear plastic tube, 150 diameters downstream of a well-rounded inlet, this length being considered sufficient to produce fully developed flow. Disturbances were minimized by steadying the flow in an equalizing chamber ahead of the inlet. Reynolds Number was varied from 1,600 to 2,300. Below this range vortices decayed quickly, while at higher Reynolds Numbers extraneous disturbances interfered with observations.

The formation of vortex filaments was induced by a trip—namely, a disc placed adjacent to the wall of the tube and normal to the stream. Three trip designs were used:

(a) A low aspect ratio trip, $^1/_4$ by $^1/_4$ in., the outer edge rounded to $^1/_8$ in. radius.

(b) A higher aspect ratio trip, $^1/_2$ by $^3/_{16}$ in., outer edge gently curved.

(c) A "scimitar" trip, $^1/_{16}$ in. uniform width, curved camber $^1/_4$ in., $^5/_8$ in. from wall to wall, such that fluid could pass underneath the arch formed by it.

The vortices were made visible by allowing ink to ooze from the sharp outer edge of the trip at a slow but steady rate or by bonding tellurium powder electroconductively to the upstream surface of the trip and rendering the fluid motion visible through electrochemical action, by the new method developed by Wortmann.[3]

It was found that a succession of horseshoe vortices were formed in the velocity discontinuity surface downstream of the trip. Generally these vortices appeared at a definite frequency that varied with Reynolds Number and perhaps with other factors not as yet identified. These vortices were stretched in downstream direction at a rate slightly less than the speed of the ambient fluid, and at the same time they were displaced across the stream toward the center of the pipe. Fig. 3 shows a series of such vortices photographed in a light flash of 30 microsec. duration, at right angles to the plane of the trip. Only on exceptional occasions did the tips of horseshoe vortices penetrate beyond the centerline of the tube, this line being the limit up to which an excess of velocity of the ambient fluid above the velocity of the vortex filament could be maintained.

Fig. 4, taken of a similar train of vortices from the same trip at 45 deg. with respect to the plane of the trip, shows more clearly the loop shape of the vortex filament. The experimental setup did not lend itself to the observation of the motion of randomly generated vortex filaments. Therefore the present evidence merely indicates that artificially induced vortex filaments, originating from a finite disturbance at Reynolds Numbers in the transition range, by the action of the "Magnus" effect, augmenting existing vorticity, generate vorticity components in both radial and axial directions.

An interesting corollary of these observations is the fact that vortex chains of the horseshoe type in a shear flow no longer coincide with stream surfaces but are actually pervious to flow. It was of interest to ascertain whether penetration of ambient flow into a chain of vortices like that of a von Kármán vortex street takes place.

Fig. 5, taken at $R = 2{,}200$, shows the two rows of vortices of opposite vorticity produced by the "scimitar" trip, of which only the center portion was covered with tellurium. The vortices of the outer row appear to behave like the ones shown in Fig. 3, the vortices of the inner row move at lesser speed downstream and toward the wall and decay more rapidly. There is, however, clear evidence that the two vortex rows diverge in shear flow and that fluid from outside the original discontinuity stream surfaces enters the region between the vortex rows. Both the divergence of vortex loops and penetration of external fluid should contribute to the rapid decay of the wake behind the obstacle.

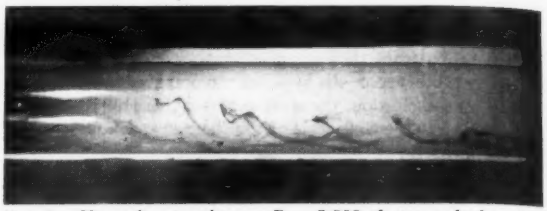

FIG. 3. Horseshoe vortices at $R = 2{,}000$ photographed at right angles to the plane of the trip.

FIG. 4. Horseshoe vortices at $R = 2{,}000$ photographed at 45 deg. to the plane of the trip.

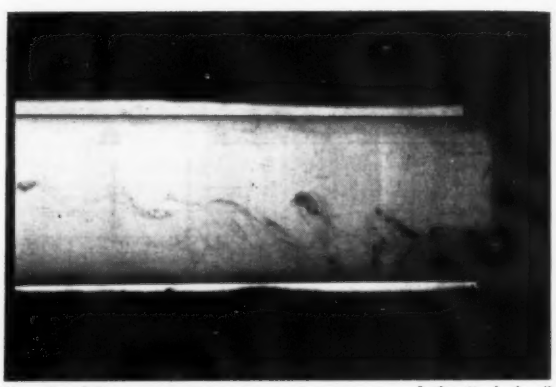

FIG. 5. Divergent vortex street downstream of the "scimitar" trip, at $R = 2{,}200$.


REFERENCES

[1] Rouse, H., *Fluid Mechanics for Hydraulic Engineers;* McGraw-Hill Book Company, Inc., New York, 1933.

[2] Theodorsen, Th., *Mechanism of Turbulence,* Proceedings of the Second Midwestern Conference on Fluid Mechanics, 1952.

[3] Wortmann, F. X., *A Method of Observation and Measurement of the Flow of Water with Tellurium,* Zeitschrift fuer Angewandte Physik, Vol. V, pp. 201-206, 1953.


## Variation of Transition Reynolds Number with Mach Number


A. H. Lange, L. P. Gieseler, and R. E. Lee

*U.S. Naval Ordnance Laboratory, White Oak, Silver Spring, Md.*


June 15, 1953

THE REYNOLDS NUMBER OF TRANSITION of the boundary layer on a slender cone and on a hollow cylinder has been deter-

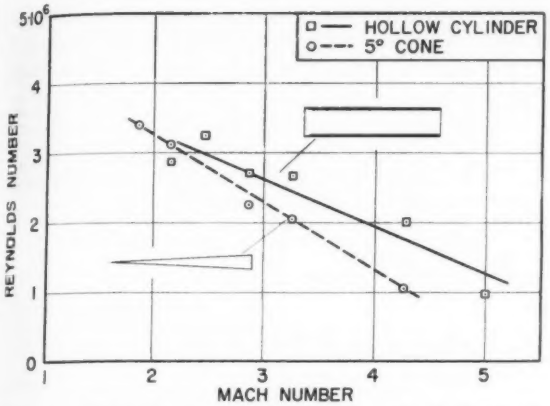


FIG. 1. Boundary-layer transition in the NOL Aeroballistics Wind Tunnel No. 2 at various Mach Numbers.

mined from spark-schlieren photographs at Mach Numbers between 1.86 and 5.00 in the intermittent NOL 40- by 40-cm. Aeroballistics Wind Tunnel No. 2. The cone had a total apex angle of 5 deg., a length of 20 in., and a base diameter of 1.75 in. The hollow cylinder had an outside diameter of 4 in., a length of 19 in., and an internal bevel of 10 deg. Supersonic flow was entering the hollow cylinder (swallowed normal shock). Both models have constant pressure along the surface in an ideal flow. They were nearly at equilibrium temperature, $1 < T_{wall} \div T_{equil.} < 1.07$, during the test. The Reynolds Number was computed from the free-stream density, velocity, and viscosity, the latter being determined at the free-stream temperature. The length used was the distance from the tip of the models to the place where the boundary layer became turbulent.

Results are shown in Fig. 1. Each point represents an average of at least twelve observations. A decrease in Reynolds Number of transition with increasing Mach Number was observed. This trend agrees with stability theory[1] but is opposite to that indicated by Gazley[2] in Fig. 9 of his article. Further results and additional experimental details are given in NAVORD Reports 2752[3] and 2823,[4] which have been published recently.

### REFERENCES

[1] Van Driest, E. R., *Calculation of the Stability of the Laminar Boundary Layer in a Compressible Fluid on a Flat Plate with Heat Transfer*, Journal of the Aeronautical Sciences, Vol. 19, No. 12, pp. 801–812, December, 1952.

[2] Gazley, C., Jr., *Boundary-Layer Stability and Transition in Subsonic and Supersonic Flow*, Journal of the Aeronautical Sciences, Vol. 20, No. 1, pp. 19–28, January, 1953.

[3] Lange, A. H., and Gieseler, L. P., *Measurement of Boundary-Layer Transition on a Standard Model to Determine the Relative Disturbance Level in Two NOL Supersonic Wind Tunnels*, NAVORD Report 2752, Naval Ordnance Laboratory, White Oak, Silver Spring, Md., February, 1953.

[4] Lee, R. E., *Measurements of Pressure Distribution and Boundary-Layer Transition on a Hollow-Cylinder Model*, NAVORD Report 2823, Naval Ordnance Laboratory, White Oak, Silver Spring, Md., April, 1953.

## Boundary Layers with Variable Heat Capacity on Nonisothermal Surfaces

Martin Bloom
*Assistant Professor of Aeronautical Engineering, Polytechnic Institute of Brooklyn, Brooklyn, N.Y.*
July 22, 1952

THE ANALYSIS OF CHAPMAN AND RUBESIN[1] for laminar boundary-layer flow over a nonisothermal flat surface can be modified in a simple way to take into account the temperature dependence of $c_p$ (see reference 1 for notation). The energy Eq. 6[1] for constant $Pr$ can be written as follows:

$$\rho u \frac{\partial i}{\partial x} + \rho v \frac{\partial i}{\partial y} = \frac{1}{(Pr)} \frac{\partial}{\partial y}\left(\mu \frac{\partial i}{\partial y}\right) + \mu \left(\frac{\partial u}{\partial y}\right)^2 \qquad (1)$$

where

$$i = \int_0^T c_p \, dt$$

the enthalpy function.

The transformed form of this equation, analogous to Eq. 20,[1] is

$$\frac{\partial^2 i^*}{\partial \eta^2} + (Pr) f \frac{\partial i^*}{\partial \eta} - 2(Pr) f' x^* \frac{\partial i^*}{\partial x^*} = -\frac{(Pr)}{4} \frac{u_\infty^2}{i_\infty} (f'')^2 \qquad (2)$$

where

$$i^* = i/i_\infty .$$

The solution of Eq. (2) and the boundary conditions satisfied by the solution are given as follows:

$$i^*(x^*, \eta) = 1 + (u_\infty^2/2i_\infty) r(\eta) + \sum_{n=0}^{\infty} a_n x^{*n} Y_n(\eta) \qquad (3)$$

$$i_w^* = 1 + (u_\infty^2/2i_\infty) r(0) + \sum_{n=0}^{\infty} a_n x^{*n} \qquad (4)$$

$$i^*(x^*, \infty) = 1 \qquad (5)$$

The functions $r$ and $Y_n$ are given in Figs. 4 and 5.[1] The transformation of Eq. (41)[1] remains unchanged—viz.,

$$(y/2)(u_\infty/\nu_\infty x C)^{1/2} = \int_0^\eta T^* \, d\eta \qquad (6)$$

However, the integral on the right-hand side of Eq. (6) must be evaluated by means of tables or formulas relating $i$ and $T$. Eq. (42)[1] is not valid when $c_p$ depends upon $T$.

The rate of heat transfer is given as follows:

$$q = -k_w \left(\frac{\partial T}{\partial y}\right)_w = -\frac{k_\infty i_\infty}{2 c_{p_\infty}} \left(\frac{\mu_w T_\infty}{\mu_\infty T_w}\right) \left(\frac{u_\infty}{\nu_\infty x C}\right)^{1/2} \times \sum_{n=0}^{\infty} a_n x^* Y_n'(0) \qquad (7)$$

where coefficients $a_n$ are determined by the prescribed variation of $i_w^*$ in Eq. (4). Eq. (7) is almost identical to Eq. (50).[1] For low values of $T_\infty$, it is seen that

$$i_\infty = c_{p\infty} T_\infty$$
$$u_\infty^2/i_\infty = (\gamma_\infty - 1) M_\infty^2$$

and Eq. (7) is identical in form to Eq. (50),[1] although the $a_n$'s are defined differently. Eq. (57)[1] for the shear remains unchanged.

### REFERENCE

[1] Chapman, D. R., and Rubesin, M. W., *Temperature and Velocity Profiles in the Compressible Laminar Boundary Layer with Arbitrary Distribution of Surface Temperature*, Journal of the Aeronautical Sciences, Vol. 16, No. 9, pp. 547–565, September, 1949.

## Concluding Discussion on the Hydraulic Analogy

E. V. Laitone
*Associate Professor, University of California at Berkeley*
June 25, 1953

IN COMMENTING ON MY PAPER,[1] Bruman[2] is correct in stating that the surface wave group velocity has no relation with the

strong hydraulic jump. However, he is completely wrong, and has entirely missed the main point of the paper, when he says that "experiments with the hydraulic analogy are usually designed to represent shock waves by hydraulic jumps." In the first place, practically all the analogy experiments are more concerned with the potential or isentropic flow which is related *only* to the group velocity. As a matter of fact, even the papers he refers to, by Orlin[3] and Preiswerk,[4] are chiefly on potential flow with no hydraulic jumps present. The Orlin[3] paper deals with the analogy of subsonic flow about a circular cylinder; the Preiswerk[4] paper gives the isentropic supersonic expansion in a Laval nozzle. Preiswerk[4] states (Part II, page 49) that water depths above 1 in. gave increasing errors as compared to theory because the vertical acceleration was no longer negligible for the larger water depths. (This corresponds to the group velocity varying with wave length as I pointed out in reference 1.) The agreement shown in Fig. 78 of Preiswerk's[4] paper would have been much better if he could have used $^1/_4$-in. depths. However, since the water was flowing, the boundary-layer growth on the tank bottom made this ideal situation impossible.

Fig. 14 of Orlin's[3] paper clearly shows the deleterious effect of water depths greater than $^1/_4$-in. The deeper water depths show a strong detached shock wave at supposedly subsonic speeds. This is not a capillarity effect, since it disappears for shallow water. It is the effect of a varying group velocity. Part of the flow pattern corresponds to supersonic flow, even though most of the flow field corresponds to subsonic flow.

The supersonic flow pattern is smaller and rides over the top of the subsonic flow pattern and destroys the analogy. It is produced by the deeper water having a much lower group velocity than given by $\sqrt{gh}$ for the shorter wave lengths (see reference 1); consequently, the shorter wave lengths all produce a common supersonic flow pattern. Again, the agreement would be best with $^1/_4$-in. water depth, but the boundary layer below the flowing water caused a more serious error. In all cases the experimental data are not in good agreement with wind-tunnel tests over the front portion of a cylinder because the water depths were greater than $^1/_4$ in.

Another point that still seems to need further emphasis is that the group velocity, not the wave velocity, provides the only analogy to the speed of sound, since it is the actual rate of propagation of energy and disturbance (see reference 1). For example, the Mach or characteristic lines in supersonic flow are the envelopes of the infinitesimal disturbances traveling at the local speed of sound, which is not a constant but depends on the local temperature. These same "characteristic lines" or envelopes are formed in free-water surface flow by the group velocity that must vary with the local water depth as $\sqrt{gh}$ but should not vary with wave length in order to maintain any analogy. The only possibility of maintaining a nearly constant group velocity for the entire spectrum of wave lengths produced is to use as large a model as possible and try to keep all the water depths between the limits of 0.10 to 0.25 in. for standard surface tension. This even requires that, if strong compression regions are present, even though isentropic, the free-stream water depth must be less than $^1/_4$ in. so it will not rise above this value in the strong compression region. If the above conditions are satisfied, then all potential disturbances, except the negligible so-called capillary ripples, are propagated at the local group velocity of $\sqrt{gh}$, and the flow corresponds to the potential flow of a perfect gas with a specific heat ratio of 2. Weak hydraulic jumps may be present, since they have a negligible increase in entropy and therefore do not invalidate the analogy. Strong hydraulic jumps cannot be present, since they do not correspond to a shock wave in a perfect gas (see Preiswerk,[4] Part II, page 3). The energy equation cannot even be used in this case, since there is a loss of total head corresponding to a change in stagnation enthalpy. However, certain comparisons can be made with strong hydraulic jumps if there are no regions corresponding to isentropic expansion or compression. These are mainly one-dimensional problems.

### References


[1] Laitone, E. V., *A Study of Transonic Gas Dynamics by the Hydraulic Analogy*, Journal of the Aeronautical Sciences, Vol. 19, No. 4, pp. 265–272, April, 1952.

[2] Bruman, J. R., *Additional Comments on "A Study of Transonic Gas Dynamics by the Hydraulic Analogy,"* Readers' Forum, Journal of the Aeronautical Sciences, Vol. 20, No. 5, pp. 359–360, May, 1953.

[3] Orlin, W. J., and others, *Application of the Analogy Between Water Flow with Free Surface and Two-Dimensional Compressible Gas Flow*, NACA Report No. 875, August, 1946.

[4] Preiswerk, E., *Application of the Methods of Gas Dynamics to Water Flow with Free Surface*, NACA TM Nos. 934 and 935, 1940.


## Open-Nose Body of Revolution of Minimum Drag at Small Supersonic Speeds*


Elliot T. Benedikt

*Consolidated Vultee Aircraft Corporation, San Diego, Calif.*


June 11, 1953

### Abstract


The drag coefficient of an open-nose body of revolution is approximated by means of a formula, valid at small supersonic speeds, due to Lighthill. The variational conditions that the equation of the profile of the body must satisfy in order to minimize the drag are converted into a singular integral equation of the Hilbert type. This equation is solved by means of a new procedure of G. Tricomi. The extremizing profile thus obtained is shown to correspond to an actual minimum for the drag.


### Symbols

$C_D$ = drag coefficient

$x$ (or $y$); $R$ = cylindrical coordinates (see Fig. 1)

$R_0$ = $R(0)$

$l$ = length of profile

$\xi$ = $x/l$

$R_1$ = $R(l)$

$S$ = $S(x)$ = cross-sectional area of body

$S_0$ = $S(0)$

$S_1$ = $S(l)$

$*\int_a^b f(x)\,dx = \lim_{\rho \to 0} \left\{ \int_a^{c-\rho} f(x)\,dx + \int_{c+\rho}^b f(x)\,dx \right\}$ = principal value of integral of function with singularity at $c$

$M$ = Mach Number

$\alpha$ = $\sqrt{M^2 - 1}$

$\epsilon$ = $\epsilon(x)$ = arbitrary function [variation of $S(x)$]

$a, b, C, c_0, c_1, c_2, c$ = constants of integration

### Introduction

A MERIDIONAL CROSS SECTION of the open-nose body of revolution considered here is shown in Fig. 1. The body will

* This paper is based on work carried out in January, 1951, for the Fort Worth Division of Consolidated Vultee Aircraft Corporation.

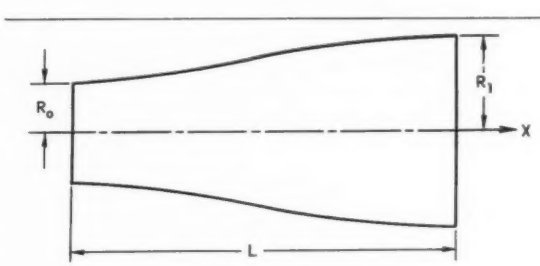


FIG. 1. Cross section of body of revolution.

be assumed to extend from $x = 0$ to $x = \infty$, and to be cylindrical with radius $R_1$ from the cross section $x = l$ on. The tangent planes at the orifice and at the point $x = l$ will be assumed to be parallel to the axis of symmetry of the body. The flow will be further assumed to be uniform in the region $0 \leq R \leq R_0$. The last condition implies that the flow, and consequently the drag, will be the same as the one that obtains with a body extending from $x = -\infty$ to $x = \infty$ being cylindrical with radius $R_0$ from $x = -\infty$ to $x = 0$ and having, from the last point on, the shape described above. Making use of an approximate form given by Lighthill[1] valid for slender bodies of revolution having a discontinuous profile and moving at small supersonic speed, the external drag coefficient can be expressed in our case by the formula (applicable as long as the change in diameter of the body is sufficiently small),

$$C_D = (1/2\pi)\left\{\int_0^l \int_0^l \log \frac{1}{|x-y|}\, S''(x)S''(y)\,dx\,dy - 2S'(0)\int_0^l S''(x)\log\frac{1}{x}\,dx + [S'(0)]^2 \log(2/\alpha R_0)\right\} \tag{1}$$

The function $S(x)$ corresponding to the profile of equation

$$R(x) = \sqrt{S(x)/\pi} \tag{2}$$

and minimizing the above expression will now be sought.

## Formulation of the Variational Problem in Integral Form

Consider a variation $\Delta C_D$ in $C_D$ caused by a bounded variation $\epsilon(x)$ of $S(x)$ satisfying the boundary conditions

$$\epsilon(x) = \epsilon'(0) = \epsilon(l) = \epsilon'(l) = 0 \tag{3}$$

We shall have

$$2\pi\Delta C_D = \int_0^l \int_0^l \log\frac{1}{|x-y|}\,[S''(x)+\epsilon''(x)][S''(y)+\epsilon''(y)]dx\,dy - 2S'(0)\int_0^l [S''(x)+\epsilon''(x)]\log\frac{1}{x}\,dx + [S'(0)]^2\log(2/\alpha R_0) - 2\pi C_D$$

$$\simeq \int_0^l \int_0^l \log\frac{1}{|x-y|}\,[\epsilon''(x)S''(y)+\epsilon''(y)S''(x)]dx\,dy - 2S'(0)\int_0^l \epsilon''(x)\log\frac{1}{x}\,dx + \int_0^l\int_0^l \log\frac{1}{|x-y|}\,\epsilon''(x)\epsilon''(y)dx\,dy$$

or, because of the symmetry of the first integral,

$$2\pi\Delta C_D = 2\int_0^l\int_0^l \epsilon''(x)S''(y)\log\frac{1}{|x-y|}\,dx\,dy - 2S'(0)\int_0^l \epsilon''(x)\log\frac{1}{x}\,dx + \int_0^l\int_0^l \log\frac{1}{|x-y|}\,\epsilon''(x)\epsilon''(y)\,dx\,dy$$

This expression can be transformed by repeated integration by parts, and taking into account conditions (3) into

$$\pi\Delta C_D = \int_0^l \epsilon(x)\left\{\left[\frac{d^2}{dx^2}\int_0^l S''(y)\log\frac{1}{|x-y|}\,dy\right] - \frac{S'(0)}{x^2}\right\}dx + 3\int_0^l\int_0^l \epsilon(x)\epsilon(y)\frac{1}{(x-y)^4}\,dx\,dy \tag{4}$$

The first integral converges since, because of the second of conditions (3),

$$\epsilon(x) = 0(x^2) \tag{5}$$

for $x \to 0$. If $\epsilon$ is small ($|\epsilon|^2 \simeq 0$), expression (3) becomes the first variation

$$\pi\delta C_D = \int_0^l \epsilon(x)\left\{\left[\frac{d^2}{dx^2}\int_0^l S''(y)\log\frac{1}{|x-y|}\,dy\right] - \frac{S'(0)}{x^2}\right\}dx$$

of $C_D$. Its vanishing is a necessary condition for the value of $C_D$ to be a minimum. Due to the arbitrariness [apart from conditions (3) (4)] of the function $\epsilon(x)$, the above requirements will be satisfied only if

$$\frac{d^2}{dx^2}\int_0^l S''(y)\log\frac{1}{|x-y|}\,dy - \frac{S'(0)}{x^2} = 0$$

Integrating twice, we obtain the singular integral equation

$$\int_0^l S''(y)\log\frac{1}{|x-y|}\,dy = -S'(0)\log x + ax + b \tag{6}$$

which the function $S''(x)$ must satisfy in order to minimize $C_D$. It is convenient to further modify the integral equation by an integration by parts. We obtain, thus,

$$\int_0^l S''(y)\log\frac{1}{|x-y|}\,dy = \lim_{\rho\to 0}\left\{\left[S'(y)\log\frac{1}{|x-y|}\right]_0^{x-\rho} + \left[S'(y)\log\frac{1}{|x-y|}\right]_{x+\rho}^{0}\right\} - \int_0^l \frac{S'(y)}{x-y}\,dy$$

Imposing upon $S(x)$ the not too restrictive condition

$$\lim_{\rho \to 0} [S'(x + \rho) - S'(x - \rho)] \log \rho = 0$$

and because of the assumption

$$S'(0) = S'(l) = 0 \tag{7}$$

we have

$$\int_0^l S''(y) \log \frac{1}{|x - y|}\, dy = \int_0^{*l} \frac{S'(y)}{y - x}\, dx$$

Replacing this result into (6) we obtain the integral equation

$$\int_0^{*l} \frac{S'(y)}{y - x}\, dy = ax + b \tag{8}$$

for $S'$.

## Inversion of the Integral Equation

The solution of the integral equation (8), if it exists, can be expressed by means of an inversion formula established recently by Tricomi[2] in the form,

$$S'(x) = \frac{1}{\pi \sqrt{x(l - x)}} \left[ C - \frac{1}{\pi} \int_0^{*l} \frac{\sqrt{y(l - y)}}{y - x} (ay + b) dy \right] \tag{9}$$

By means of the substitutions

$$y = (l/2)(1 - \cos \theta)$$
$$x = (l/2)(1 - \cos \varphi)$$

the integral

$$I = \frac{1}{\pi} \int_0^{*l} \frac{\sqrt{y(l - y)}}{y - x} (ay + b)$$

appearing in Eq. (9) can be written in the form

$$I = \frac{1}{\pi} \int_0^{*\pi} \frac{\sin^2 \theta}{\cos \theta - \cos \varphi} [A \cos \theta - B]\, d\theta$$

Using the identities,

$$\sin^2 \theta = (1 - \cos 2\theta)/2$$
$$\sin^2 \theta \cos \theta = (\cos \theta - \cos 3\theta)/4$$

and

$$\int_0^{*\pi} \frac{\cos n\theta}{\cos \theta - \cos \varphi}\, d\theta = \pi \frac{\sin n\varphi}{\sin \varphi}$$

$I$ becomes a quadratic form in $\cos \varphi$ and consequently in $x$. Replacing this result into Eq. (9), we obtain

$$S'(x) = \frac{c_0 + c_1 x + c_2 x^2}{\sqrt{x(\rho - x)}} \tag{10}$$

Because of Eq. (7), we must have $c_0 = 0$, $c_1/l = -c_2 = c$. Replacing this determination of the constants of integration into Eq. (10) and integrating once more, we get

$$S(x) = S_0 + c \int_0^x \sqrt{y(l - y)}\, dy =$$

$$S_0 + (c/4)[(2x - l) \sqrt{x(l - x)} - l^2 \sin^{-1} \sqrt{x/l}] \tag{11}$$

From the boundary condition $S(l) = S_1$, we obtain the determination

$$c/4 = 2(S_1 - S_0)/l^2 \pi = 2(R_1^2 - R_0^2)/l^2 \tag{11'}$$

for the remaining integration constant.

## The Profile of Minimum Drag

The expression

$$S(x) = S_0 + (2/\pi)(S_1 - S_0)[\sin^{-1} \sqrt{\xi} + (2\xi - 1) \sqrt{\xi(1 - \xi)}] \tag{12}$$

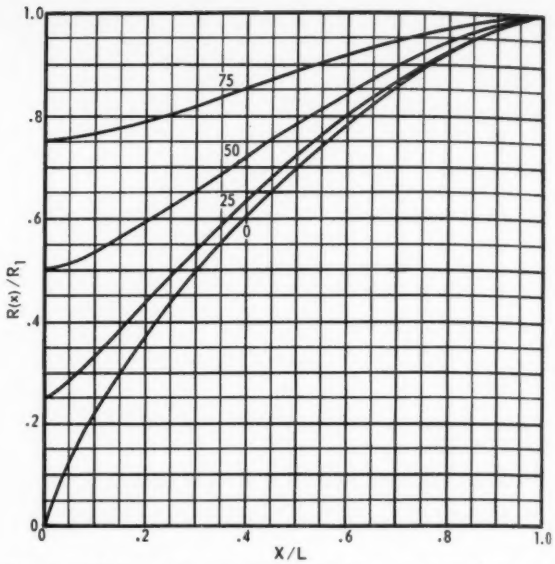


FIG. 2. Minimum drag profiles for $R_0/R_1 = 0$, 0.25, 0.50, and 0.75.

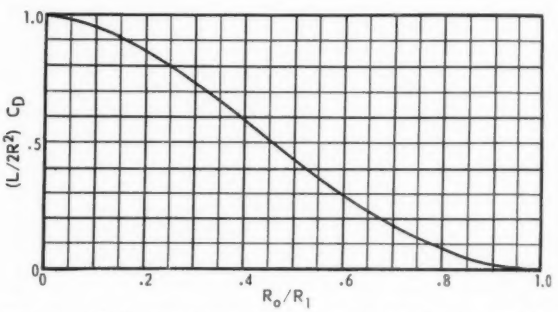


FIG. 3. Minimum drag coefficient as a function of $R_0/R_1$.

obtained replacing Eq. (11') into Eq. (11) represents the cross-sectional area of a surface of external drag. This result has to be further qualified by an analysis of the second variation which, as shown by Eq. (4), is

$$(\pi/3)\delta^2 C_D = \int_0^l \int_0^l \frac{\epsilon(x)\epsilon(y)}{(x - y)^4}\, dx\, dy$$

Because of the assumed boundedness of the function $\epsilon(x)$, the largest contribution to this integral will arise for values in the neighborhood of $x = y$. The numerator of the integrand can then be replaced by $\epsilon^2(x)$, from which it follows that $\delta^2 C_D = \infty > 0$. The cross-sectional area defined by Eq. (12) will therefore minimize the drag of the body of revolution considered here within the range of validity of formula (1). Because of Eq. (2), the profile corresponding to this cross section will be given by

$$R(x) = R_0 \{1 + (2/\pi)[(R_1/R_0)^2 - 1]$$
$$[\sin^{-1} \sqrt{\xi} + (2\xi - 1) \sqrt{\xi(1 - \xi)}]\}^{1/2}$$

Graphical representations of this function are shown for various values of the ratio $R_1/R_0$ in Fig. 2. The dependence of the minimum drag upon the ratio between the rear-end and front-end base diameters of the profile is represented graphically in Fig. 3.

## References


[1] Lighthill, M. J., *Supersonic Flow Past Bodies of Revolution*, R. & M. No. 2003, Aeronautical Research Council, London, 1945.

[2] Tricomi, F. G., *On the Finite Hilbert Transformation*, Quart. J. Math., Oxford Ser. (2) 2, pp. 199–211, 1951. (The author had the privilege of using Dr. Tricomi's manuscript before its publication.)

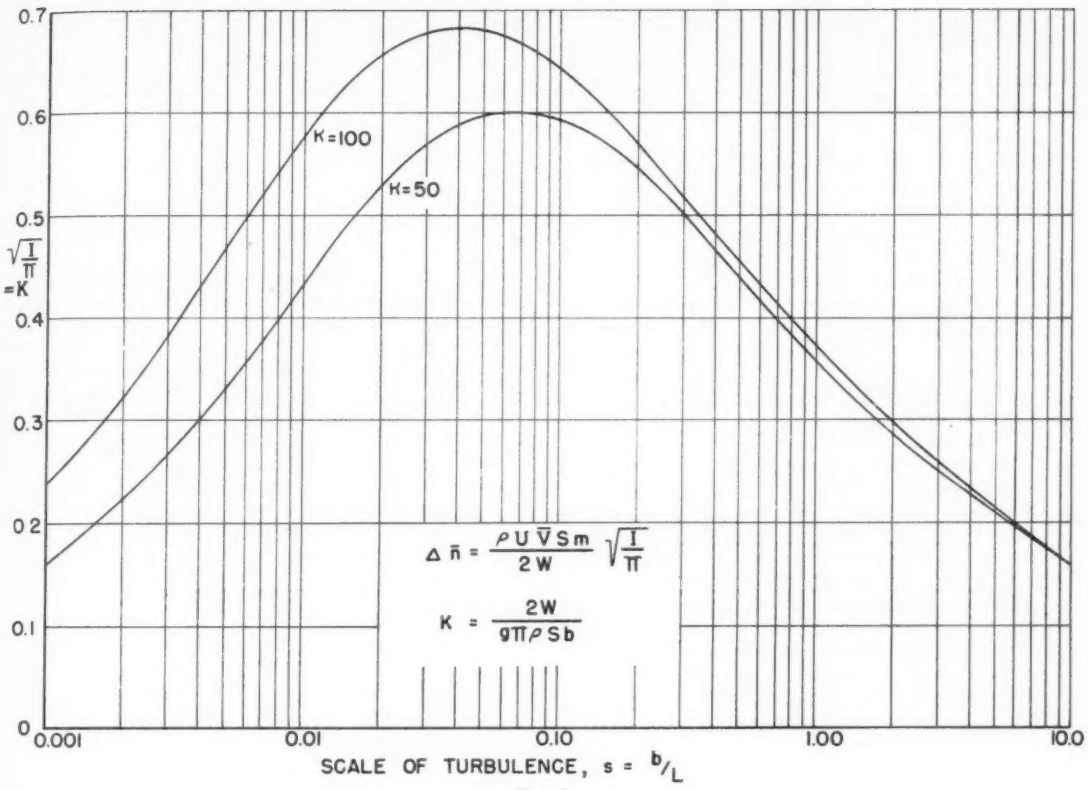


FIG. 1.

## An Expression for the Gust Alleviation Factor

M. L. Williams
*Assistant Professor of Aeronautics, California Institute of Technology, Pasadena, Calif.*
June 22, 1953

IN A RECENT PAPER,[1] Fung has investigated the application of statistical analysis to structures loaded dynamically. As one example of the procedure, he has worked out the root mean square vertical acceleration of a rigid two-dimensional wing in turbulent flow as

$$\overline{\ddot{z}^2} = \overline{w^2}\,[4U^2/\pi b^2(1+\kappa)^2]I(a,s)$$

where

$\overline{\ddot{z}^2}$ = mean square vertical acceleration, ft. per sec. per sec.
$\overline{w^2}$ = mean square turbulent vertical velocity, ft. per sec.
$U$ = flight speed, ft. per sec.
$b$ = semichord, ft.
$\kappa$ = mass density ratio for the airplane ($=2W/\pi\rho Sbg$)
$W/S$ = wing loading, lbs. per sq.ft.
$a$ = $2/[s(1+\kappa)]$
$s$ = $b/L$
$L$ = characteristic length of turbulence, ft.
$\rho$ = air density, slugs per cu.ft.
$g$ = gravity acceleration, ft. per sec. per sec.
$I(a, s)$ = function given graphically (Fig. 5) and also analytically [Eqs. (56)–(60)] in the reference

By making use of the approximation that $\kappa >> 1$ in most practical cases, the relation can be manipulated into the form

$$\frac{(W/g)\sqrt{\overline{\ddot{z}^2}}}{W} = \frac{(2\pi)\rho\sqrt{\overline{w^2}}\,US}{2W}\sqrt{\frac{I(a,s)}{\pi}}$$

which, upon defining $(W/g)\,(\overline{\ddot{z}^2})^{1/2}/W$ as the mean acceleration, $\Delta\bar{n}$, $(\overline{w^2})^{1/2}$ by $\bar{V}$, a mean vertical velocity, and replacing $2\pi$ by $m$, the lift curve slope, there results the form

$$\Delta\bar{n} = \frac{\rho U \bar{V} S m}{2W}\sqrt{\frac{I(a,s)}{\pi}}$$

which is similar to the usual gust formula if $(I/\pi)^{1/2}$ is equated to $K$, the gust alleviation factor. Fig. 1 shows a graph of $(I/\pi)^{1/2}$ against the chord to turbulence ratio with the mass ratio as a parameter. It may be noted that in American literature it has been customary to use $K = K\,(W/S)$, although other countries have used the mass ratio dependence. The two differ essentially by the length of the chord, but it is thought that the mass ratio is the more definitive parameter.

Until experimental evidence for the scale of atmospheric turbulence is complete—i.e., the proper number of chord lengths to use for $L$, the scale or characteristic length of the gust, in obtaining $s$ and thus $K$—it is suggested that one use the maximum values which vary as a function of the mass ratio; secondly, reference to the figure gives a good idea as to the sensitivity of the incremental load factor as affected by the mass ratio and turbulence scale.

It is believed therefore that the Fung expression may be used as a basis for separating the gust velocity ($\bar{V}$), which is a function of the atmosphere, from the gust alleviation factor ($K$), which characterizes the airplane, thus permitting a quantitative prediction of the gust load factor. Improvements will be effected by considering (1) the probability distribution of $\Delta\bar{n}$, (2) a nonrigid wing, (3) finite span effects, and (4) a more precise representation of the gust power spectrum.

### REFERENCE

[1] Fung, Y. C., *Statistical Aspects of Dynamic Loads*, Journal of the Aeronautical Sciences, Vol. 20, No. 5, p. 317, May, 1953.

# On an Integral Equation in the Supersonic Oscillating Wing Theory†

T. Y. Li and H. J. Stewart

*Guggenheim Aeronautical Laboratory, California Institute of Technology, Pasadena, Calif.*

June 15, 1953

IN REFERENCE 1, A SOURCE-SUPERPOSITION METHOD of solution of a periodically oscillating wing at supersonic speed was proposed by the writers. Using this method, the problem of a rectangular wing with supersonic periodic motions was treated.[2, 3] Miles,[4] by a Fourier transform method, Stewartson,[5] by the Laplace transform method, and recently Goodman,[6] by a method proposed by Gardner,[7] have also treated this rectangular oscillating wing problem. While our solutions of the rectangular wing yield numerical results in close agreement with the results of Miles, et al., over a wide range of frequencies and Mach Numbers, it has been discovered that they are not identical. In solving the basic integral equation [Eq. (25), reference 1] which appears in our method of approach, we have made an implicit assumption that the magnitude of the upwash velocity in the region outside the wing tip is, in a certain sense, independent of the oscillatory motion. This assumption imposes severe limitations on the solutions such that they are, as will be shown later, valid in general only for terms of zero and first order in frequency. As the general method of approach outlined in reference 1 can be used in treating problems of a class of wings of general plan forms, it seems worth while to make some attempt to improve the accuracy of our method. In the present note, the basic integral equation is re-examined. A procedure has been found whereby it is possible to improve the accuracy of the method to yield solutions valid to terms of any order in frequency.

† Since the completion of the present note, two interesting papers[10, 11] have appeared which deal with problems related to the present subject by different approaches.

The basic integral equation under consideration is

$$\int_0^{u_D} \frac{du}{\sqrt{u_D - u}} \int_{v_1}^{v_2} \frac{\Lambda_B - \Lambda_T}{2\sqrt{v_D - v}} F(u, v, \nu, u_D, v_D)\, dv = \int_0^{u_D} \frac{du}{\sqrt{u_D - u}} \int_{v_2}^{v_D} \frac{\Lambda_D}{\sqrt{v_D - v}} F(u, v, \nu, u_D, v_D)\, dv \quad (1)$$

where

$$F = \exp\left\{-\frac{i\nu}{\beta a}\left[(u_D - u) + (v_D - v)\right]\right\} \times \cos\left[\frac{2\nu}{\beta a M}\sqrt{(u_D - u)(v_D - v)}\right] \quad (2)$$

where $\beta^2 = M^2 - 1$, $M$ represents the free-stream Mach Number, $a$ represents the speed of sound in the free stream, and $\nu$ represents the frequency of the periodic motions of the wing. The quantities $v_1$, $v_2$, which represent the leading edges of the wing (Fig. 1), are given functions of $u$; $\Lambda_B$ and $\Lambda_T$, which represent the effective slopes of the stream lines on the bottom and the top sides of the wing, are given functions of the characteristic coordinates $(u, v)$; $u_D$ and $v_D$ define a point on the diaphragm region outside the wing tip; and $\Lambda_D$ represents the unknown upwash function in the diaphragm region. This integral equation for $\Lambda_D$ was solved by the simple procedure in reference 1 under the assumption that $\Lambda_D$ is a function of $(u, v)$ only. In general, $\Lambda_D$ is an unknown function of $(u, v, \nu, M)$, since the physical parameters $\nu$ and $M$ enter the kernel of the integral equation $F$ as in Eq. (2). Suppose $\Lambda_D$ is expanded in an infinite series in $\nu$, thus,

$$\Lambda_D = \sum_{n=0}^{\infty} (i\nu/\beta a)^n \Lambda_n \quad (3)‡$$

where $n$ are integers. Substituting Eq. (3) into Eq. (1) and equating like power terms in $\nu$ yields a system of integral equations with $\Lambda_n(u, v)$ as the unknowns. Thus,

‡ Terms involving fractional powers and logarithms of $\nu$ do not enter the solution because of the nature of Eq. (1).

$$\frac{1}{n!}\int_0^{u_D} \frac{du}{\sqrt{u_D - u}} \int_{v_1}^{v_2} \frac{\Lambda_B - \Lambda_T}{2\sqrt{v_D - v}} \left\{\left[(u_D - u) + (v_D - v) - \frac{2}{M}\sqrt{(u_D - u)(v_D - v)}\right]^n + \left[(u_D - u) + (v_D - v) + \frac{2}{M}\sqrt{(u_D - u)(v_D - v)}\right]^n\right\} dv = \sum_{m=0}^{n} \frac{(-)^m}{(n-m)!} \int_0^{u_D} \frac{du}{\sqrt{u_D - u}} \int_{v_2}^{v_D} \frac{\Lambda_m}{\sqrt{v_D - v}} \times \left\{\left[(u_D - u) + (v_D - v) - \frac{2}{M}\sqrt{(u_D - u)(v_D - v)}\right]^{n-m} + \left[(u_D - u) + (v_D - v) + \frac{2}{M}\sqrt{(u_D - u)(v_D - v)}\right]^{n-m}\right\} dv \quad (4)$$

From Eq. (4), the following equations defining $\Lambda_0$, $\Lambda_1$, $\Lambda_2$, and $\Lambda_3$, respectively, can be derived:

$$\int_{v_1}^{v_2} \frac{\Lambda_B - \Lambda_T}{2\sqrt{v_D - v}}\, dv = \int_{v_2}^{v_D} \frac{\Lambda_0}{\sqrt{v_D - v}}\, dv \quad (5)$$

$$\int_{v_1}^{v_2} \frac{\Lambda_B - \Lambda_T}{2}\sqrt{v_D - v}\, dv - \int_{v_2}^{v_D} \Lambda_0 \sqrt{v_D - v}\, dv = -\int_{v_2}^{v_D} \frac{\Lambda_1}{\sqrt{v_D - v}}\, dv \quad (6)$$

$$\int_{v_1}^{v_2} \frac{\Lambda_B - \Lambda_T}{2}(v_D - v)^{3/2}\, dv - \int_{v_2}^{v_D} \Lambda_0 (v_D - v)^{3/2}\, dv + 2\int_{v_2}^{v_D} \Lambda_1 \sqrt{v_D - v}\, dv - \frac{2}{M^2}\int_0^{b} du_1 \int_{v_2(u_1)}^{v_D} \frac{\Lambda_1}{\sqrt{v_D - v}}\, dv = 2\int_{v_2}^{v_D} \frac{\Lambda_2}{\sqrt{v_D - v}}\, dv \quad (7)$$

$$-\frac{1}{6}\int_{v_1}^{v_2} \frac{\Lambda_B - \Lambda_T}{2}(v_D - v)^{5/2}\, dv + \frac{1}{6}\int_{v_2}^{v_D} \Lambda_0 (v_D - v)^{5/2}\, dv - \frac{1}{2}\int_{v_2}^{v_D} \Lambda_1 (v_D - v)^{3/2}\, dv + \int_{v_2}^{v_D} \Lambda_2 (v_D - v)^{1/2}\, dv - \frac{2}{M^2}\int_0^{u} du_1 \int_{v_2(u_1)}^{v_D} \frac{\Lambda_2}{\sqrt{v_D - v}}\, dv + \frac{1}{M^2}\int_0^{u} du_1 \int_{v_2(u_1)}^{v_D} \Lambda_1 (v_D - v)^{1/2}\, dv + \frac{1}{M^2}\left(1 - \frac{2}{M^2}\right)\int_0^{u} du_2 \int_0^{u_2} du_1 \times \int_{v_2(u_1)}^{v_D} \frac{\Lambda_1}{\sqrt{v_D - v}}\, dv = \int_{v_2}^{v_D} \frac{\Lambda_3}{\sqrt{v_D - v}}\, dv \quad (8)$$

Similar equations define the $\Lambda_n$'s for $n = 4, 5, \ldots$ The scheme of solution of this set of integral equations is: (1) Solve Eq. (5) for $\Lambda_0$; (2) substitute $\Lambda_0$ thus found into Eq. (6) and solve for $\Lambda_1$; (3) substitute $\Lambda_0$, $\Lambda_1$ thus found into Eq. (7), and solve for $\Lambda_2$; etc. It is clear that we can carry out this scheme indefinitely to obtain $\Lambda_n$ for arbitrary $n$. It is further noticed that the $\Lambda_n$'s are all defined by integral equations of the Abelian type whose solutions are well known.[8] For a flat plate wing, $(1/2)(\Lambda_B - \Lambda_T) = \alpha$, we obtain the following results for $\Lambda_0$, $\Lambda_1$, and $\Lambda_2$:

$$\Lambda_0 = \frac{2\alpha}{\pi}\left[\sqrt{\frac{v_2(u) - v_1(u)}{v - v_2(u)}} - \tan^{-1}\sqrt{\frac{v_2(u) - v_1(u)}{v - v_3(u)}}\right] \tag{9}\dagger$$

$$\Lambda_1 = -(2\alpha/3\pi)\left\{[v_3(u) - v_1(u)]^{3/2}/\sqrt{v - v_2(u)}\right\} \tag{10}$$

$$\Lambda_2 = \frac{\alpha}{2\pi\sqrt{v - v_2(u)}}\left\{-\left[v_2(u) - v_1(u)\right]^{3/2}\left[v_1(u) - \frac{2}{3}v_2(u)\right] - \frac{3}{5}\left[v_2(u) - v_1(u)\right]^{5/2} + \frac{4}{3M^2}\int_0^u \left[v_2(u) - v_1(u)\right]^{3/2} du + \frac{1}{3}\left[v_2(u) - v_1(u)\right]^{3/2}\left[2v - v_2(u)\right]\right\} \tag{11}$$

At the subsonic leading edge $v = v_2(u)$, $\Lambda_0$, $\Lambda_1$, and $\Lambda_2$ become infinite; thus, they possess the correct singularity property.

The contribution of the diaphragm to the velocity potential at a point $(u_w, v_w, \pm 0)$ on the top or bottom surface of the wing is given as[1]

$$\Phi_{wD}(u_w, v_w, \pm 0, t) = \mp \frac{a}{\pi}\exp(i\nu t)\int_0^{u'} \frac{du}{\sqrt{u_w - u}}\int_{v_2(u)}^{v_w} \frac{\Lambda_D}{\sqrt{v_w - v}} F(u, v, \nu, u_w, v_w)\, dv \tag{12}$$

where $u'$ is defined by $v_2(u') = v_w$ (Fig. 1). Expanding $\Phi_{wD}$ in power series in $\nu$ yields

$$\Phi_{wD} = \mp \frac{a}{2\pi}\exp(i\nu t)\sum_{n=0}^{\infty}\left(-\frac{i\nu}{\beta a}\right)^n \sum_{m=0}^{n}\frac{(-)^m}{(n-m)!}\int_0^{u'}\frac{du}{\sqrt{u_w - u}}\int_{v_2}^{v_w}\frac{\Lambda_m}{\sqrt{v_w - v}}\times \left\{\left[(u_w - u) + (v_w - v) - \frac{2}{M}\sqrt{(u_w - u)(v_w - v)}\right]^{n-m} + \left[(u_w - u) + (v_w - v) + \frac{2}{M}\sqrt{(u_w - u)(v_w - v)}\right]^{n-m}\right\} dv \tag{13}$$

We can rewrite our integral equations defining the $\Lambda_n$'s, for instance, Eqs. (5)–(8), with $v_D$ replaced by $v_w$, and these equations remain valid. Using these results, we can eliminate the $\Lambda_n$'s in Eq. (13). The result can be written as

$$\Phi_{wD} = \mp \frac{a}{\pi}\exp(i\nu t)\left\{\int_0^{u'}\frac{du}{\sqrt{u_w - u}}\int_{v_1}^{v_2}\frac{\Lambda_B - \Lambda_T}{2\sqrt{v_w - v}}F(u, v, \nu, u_w, v_w)\, dv + \sum_{n=0}^{\infty}\left(-\frac{i\nu}{\beta a}\right)^n \Delta\Phi_n\right\} \tag{14}$$

On the basis of the assumption $\Lambda_D = \Lambda_D(u, v)$ we previously obtained the result that $\Delta\Phi_n = 0$ for all $n$ [Eq. (33), reference 1]. The corrected computations show, however, that $\Delta\Phi_n = 0$ is true only for $n = 0$ and $n = 1$ and that $\Delta\Phi_n \not\equiv 0$ for $n = 2, 3, \ldots$. This result substantiates our statement in the opening paragraph that our results in references 1–3 are valid in general for terms of zero and first order in frequency. For higher order of accuracy, we have to introduce the correction potentials $\Delta\Phi_n$, which can be evaluated by our present method; for instance,

$$\Delta\Phi_2 = \frac{2}{M^2}\sqrt{u_w - u'}\int_0^{u'} du\int_{v_2(u)}^{v_w}\frac{\Lambda_1}{\sqrt{v_w - v}}\, dv \tag{15}$$

$$\Delta\Phi_3 = \frac{2}{M^2}\sqrt{u_w - u'}\left[-2\int_0^{u'} du\int_{v_2(u)}^{v_w}\frac{\Lambda_2}{\sqrt{v_w - v}}\, dv + \int_0^{u'} du\int_{v_2(u)}^{v_w}\Lambda_1\sqrt{v_w - v}\, dv + \left(1 - \frac{2}{M^2}\right)\int_0^{u'} du\int_0^{u} du_1\int_{v_2(u_1)}^{v_w}\frac{\Lambda_1}{\sqrt{v_w - v}}\, dv + (u_w - u')\int_0^{u'} du\int_{v_2(u)}^{v_w}\frac{\Lambda_1}{\sqrt{v_w - v}}\, dv\right] \tag{16}$$

† First obtained by Evvard and Turner in reference 9.

---

As an example of the application of the present method, we can deduce some correction terms for the lift coefficient expression given in reference 2 for a rectangular wing with vertical oscillations. For this simple geometrical configuration, $\Delta\Phi_2$ and $\Delta\Phi_3$ can be simply evaluated from Eqs. (15) and (16). Thus, the lift coefficient in the mixed supersonic region, $C_{L_1}$, as given in Eq. (32) of reference 2, has to be subjected to the following corrections:

$$\Delta_2 = \text{correction in } \nu^2 \text{ term} = -\frac{\alpha}{12}\frac{k_c^2}{\beta M^2}\exp(i\nu t) \tag{17}$$

$$\Delta_3 = \text{correction in } \nu^3 \text{ term} = i\alpha\left(\frac{1}{20} + \frac{1}{60M^2}\right)\frac{k_c^3}{\beta M^2}\exp(i\nu t) \tag{18}$$

where $k_c = M\nu x_c/\beta^2 a$ is the reduced frequency, $x_c$ being the wing chord. From reference 2, [Eqs. (68) and (76)], the wing-tip correction term is

$$L_3(k_c) = \beta \text{A.R.}\left(\frac{C_{L_W} - C_{L_0}}{C_{L_0}^*}\right) = \frac{C_{L_1} + 2C_{M_0}}{C_{L_0}^*} \tag{19}$$

where A.R. denotes the aspect ratio, and $C_{L_0}$ and $C_{M_0}$ denote the lift and moment coefficients in the purely supersonic region and

$$C_{L_0}^* = (4\alpha/\beta)\exp(i\nu t)$$

The expansion of $L_3(k_c)$ in reference 2 as a power series of $k_c$, up to the $k_c^3$-term, is

$$L_3(k_c) = -\frac{1}{2} + \frac{i}{6}\left(1 + \frac{1}{M^2}\right)k_c + \frac{1}{24}\left(1 + \frac{7}{2M^2}\right)k_c^2 - \frac{i}{120}\left(1 + \frac{15}{2M^2} + \frac{3}{2M^4}\right)k_c^3 + \ldots \tag{20}$$

With the correction terms from Eqs. (18) and (17),

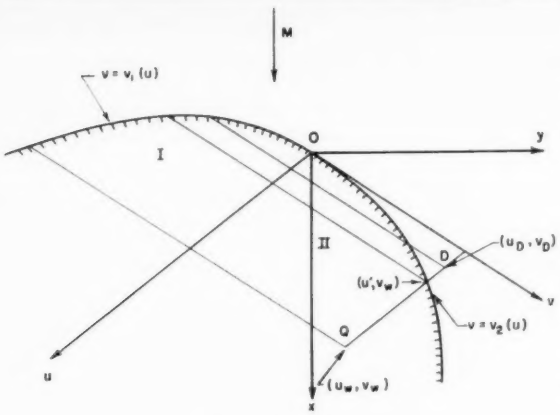


FIG. 1 — GEOMETRY OF WING

$$L_3(k_c) = -\frac{1}{2} + \frac{i}{6}\left(1 + \frac{1}{M^2}\right) k_c + \frac{1}{24}\left(1 + \frac{3}{M^2}\right) k_c^2 - \frac{i}{120}\left(1 + \frac{6}{M^2} + \frac{1}{M^4}\right) k_c^3 + \ldots \quad (21)$$

which is identical with the corresponding series from Miles' result.[4] Therefore, by the present method, the previous results[2, 3] can be improved to an arbitrary degree of exactness. It is apparent that the present method does not yield solutions in a closed form, so the particular problems of the rectangular wing are best treated by the methods of Miles and Stewartson. More complex plan forms can be treated by the present method or by that of Goodman.

### References


[1] Stewart, H. J., and Li, Ting-Yi, *Source-Superposition Method of Solution of a Periodically Oscillating Wing at Supersonic Speeds*, Q. Appl. Math., vol. 9, p. 31, 1951.

[2] Stewart, H. J., and Li, Ting-Yi, *Periodic Motions of a Rectangular Wing Moving at Supersonic Speed*, Journal of the Aeronautical Sciences, vol. 17, p. 529, 1950.

[3] Li, Ting-Yi, *Purely Rolling Oscillations of a Rectangular Wing in Supersonic Flow*, Journal of the Aeronautical Sciences, vol. 18, p. 191, 1951.

[4] Miles, J. W., *The Oscillating Rectangular Airfoil at Supersonic Speeds*, Q. Appl. Math., vol. 9, p. 47, 1951.

[5] Stewartson, K., *On the Linearized Potential Theory of Unsteady Supersonic Motion*, Q. J. Mech. & Appl. Math., vol. 3, p. 182, 1950.

[6] Goodman, T. R., *The Quarter-Infinite Wing Oscillating at Supersonic Speeds*, Cornell Aero. Lab. Rep. No. 36, 1951.

[7] Gardner, C. S., *Time-Dependent Linearized Supersonic Flow Past Planar Wings*, Communications on Pure & Appl. Math., vol. 3, 1950.

[8] Bocher, M., *An Introduction to the Study of Integral Equations;* Cambridge Univ. Press, 1909.

[9] Evvard, J. C., and Turner, L. R., *Theoretical Lift Distribution and Upwash Velocities for Thin Wings at Supersonic Speeds*, NACA TN No. 1484, 1947.

[10] Stewartson, K., *On the Linearized Potential Theory of Unsteady Supersonic Motion (Part 2)*, Q. J. Mech. & Appl. Math., vol. 5, p. 137, 1952.

[11] Miles, J. W., *A General Solution for the Rectangular Airfoil in Supersonic Flow*, Q. Appl. Math., vol. 11, p. 1, 1953.


## Application of the Compensation Theorem to the Modification of Redundant Structures


R. H. MacNeal

*Assistant Professor of Electrical Engineering, Analysis Laboratory, California Institute of Technology, Pasadena, Calif.*



June 15, 1953


THE DETERMINATION OF THE STRESSES in a highly redundant structure inevitably requires a large number of numerical calculations, and in the design of such a structure these calculations must be repeated many times to determine the optimum combination of structural components. Some of these combinations may be identical except for modifications at a few points in the structure, so that it would be advantageous to evaluate the effect of these modifications without the necessity of repeatedly solving the entire system of equations. In a recent article[1] attention has been drawn to a simple method, originally due to Best,[2] which in some instances greatly decreases the amount of numerical work required. The purpose of this article is to generalize the method and to express it in a mathematical language that may be applied to any problem requiring the solution of a system of linear equations.

In the method it is assumed that a solution has been obtained for one combination of structural components and that a structural modification gives rise to changes in only a few of the coefficients of the unknown quantities. The equations of the modified structure are then manipulated so as to restore the coefficients to their original values leaving the effect of the structural modification in the constant terms. An elementary application of this idea has been employed in electrical engineering for many years where it has been called the "Compensation Theorem";[3] electrical engineers, however, have not taken full advantage of its possibilities because they are seldom interested in accurate, detailed solutions of large networks.

Any method of analyzing redundant structures eventually reduces to the solution of a system of simultaneous linear algebraic equations, and these equations will be taken as the starting point of the method.

The system of $n$ equations for the modified structure, written in matrix form are

$$[A]\,[F] = [U] \quad (1)$$

and for the original unmodified structure

$$[A^0]\,[F^0] = [U] \quad (2)$$

The $n$-rowed column matrices $[F]$ and $[F^0]$ are the unknown quantities in the modified and unmodified structures, respectively, and the $n$-rowed column matrix $[U]$ is the matrix of constant terms, assumed to be the same for both the modified and unmodified structures.

$$[F] = \begin{bmatrix} F_1 \\ F_2 \\ \cdot \\ \cdot \\ \cdot \\ F_n \end{bmatrix}, \qquad [F^0] = \begin{bmatrix} F_1{}^0 \\ F_2{}^0 \\ \cdot \\ \cdot \\ \cdot \\ F_n{}^0 \end{bmatrix}, \qquad [U] = \begin{bmatrix} U_1 \\ U_2 \\ \cdot \\ \cdot \\ \cdot \\ U_n \end{bmatrix}$$

The $n$ by $n$ square matrix of coefficients $[A]$ is assumed to be the same as the matrix $[A^0]$, except for differences occurring in the first $m$ rows and the first $m$ columns. It is therefore convenient to partition $[A]$ and $[A^0]$ into four submatrices, respectively, of which three are pairwise identical,

$$[A] = \left[\begin{array}{c|c} A_{mm} & A_{mn} \\ \hline A_{nm} & A_{nn} \end{array}\right], \qquad [A^0] = \left[\begin{array}{c|c} A_{mm}{}^0 & A_{mn} \\ \hline A_{nm} & A_{nn} \end{array}\right] \quad (3)$$

where

$$[A_{mm}] = \begin{bmatrix} A_{11} \ldots A_{1,\,m} \\ \cdot \quad\quad \cdot \\ \cdot \quad\quad \cdot \\ \cdot \quad\quad \cdot \\ A_{m,\,1} \ldots A_{mm} \end{bmatrix}, \qquad [A_{mm}{}^0] = \begin{bmatrix} A_{11}{}^0 \ldots A_{1,\,m}{}^0 \\ \cdot \quad\quad\quad \cdot \\ \cdot \quad\quad\quad \cdot \\ \cdot \quad\quad\quad \cdot \\ A_{m,\,1}{}^0 \ldots A_{m,\,m}{}^0 \end{bmatrix}$$

$$[A_{mn}] = \begin{bmatrix} A_{1,\,m+1} \ldots A_{1,\,n} \\ \cdot \quad\quad\quad \cdot \\ \cdot \quad\quad\quad \cdot \\ \cdot \quad\quad\quad \cdot \\ A_{m,\,m+1} \ldots A_{m,\,n} \end{bmatrix}, \qquad \ldots \text{etc.} \ldots$$

The matrices $[F]$ and $[A]$ will be written as the sum of the unmodified matrices plus correction terms.

$$[F] = [F^0] + [\delta F] \quad (4)$$

$$[A] = [A^0] + [\delta A_{mm}] \tag{5}$$

where $[\delta F]$ has $n$ nonzero rows and $[\delta A_{mm}]$ has $m$ nonzero rows and columns. It should be emphasized that the elements of $[\delta A_{mm}]$ are not necessarily small and may be of the same order as the elements of $[A]$. With the aid of Eq. (5), Eq. (1) can now be rewritten as

$$[A^0]\,[F] = -[\delta A_{mm}]\,[F] + [U] \tag{6}$$

The vector $-[\delta A_{mm}]\,[F]$ is regarded as an inhomogeneous, or "constant," term in this equation, and it will be given a new symbol,

$$[\delta U_m] = -[\delta A_{mm}]\,[F] \tag{7}$$

The significance of the method rests upon the fact that the determination of $[\delta U_m]$ requires the solution of only $m$, rather than $n$, simultaneous equations. Since $[\delta A_{mm}]$ has only $m$ nonzero rows and columns, it is evident that only the first $m$ components of $[\delta U_m]$ are nonzero. Eq. (6) can be rewritten as

$$[A^0]\,[F^0] + [A^0]\,[\delta F] = [\delta U_m] + [U] \tag{8}$$

Hence, using Eq. (2)

$$[A^0]\,[\delta F] = [\delta U_m] \tag{9}$$

Eq. (9) can be used to evaluate the increments in the unknowns once $[\delta U_m]$ is calculated. An equation in which $[\delta U_m]$ is the only unknown may be obtained by expanding $[F]$ in Eq. (7) into $[F^0] + [\delta F]$ and evaluating $[\delta F]$ from Eq. (9),

$$[\delta U_m] = -[\delta A_{mm}]\,\{[F^0] + [\delta F]\} = -[\delta A_{mm}]\,[F^0] - [\delta A_{mm}]\,[A^0]^{-1}\,[\delta U_m] \tag{10}$$

Only the first $m$ rows and columns of the inverse matrix $[A^0]^{-1}$ are required, since $[\delta U_m]$ has only $m$ nonzero values. Let $[B_{mm}]$ be the matrix of the first $m$ rows and columns of $[A^0]^{-1}$ and let $[I_m]$ be the identity matrix of the first $m$ rows and columns. Then,

$$\{[I_m] + [\delta A_{mm}]\,[B_{mm}]\}\,[\delta U_m] = -[\delta A_{mm}]\cdot[F^0] \tag{11}$$

The solution of the original problem, Eq. (1), thus requires the determination of the influence numbers of the first $m$ rows and columns of the unmodified structure, $[B_{mm}]$, and the solutions of Eqs. (11) and (9). The inversion of Eq. (9) requires all the rows of $[A^0]^{-1}$ but only the first $m$ columns. It is evident that little will be gained by the method if $m$ is not a great deal smaller than $n$ and that methods of solving the unmodified structure which easily yield the influence numbers are desirable.[4] If a program involving many structural modifications is to be undertaken, it is evidently desirable to write the equations in such a way that the modifications appear in as few of the coefficients as possible.

Some interesting observations can be made concerning the case where there is only a single structural modification, which may be assumed to occur in the first row and the first column. In this case Eq. (11) becomes a scalar equation for which the solution can be immediately written as

$$\delta U_1 = -\delta A_{11} F_1^0/(1 + \delta A_{11} B_{11}) \tag{12}$$

The increments in the unknowns are from Eq. (9),

$$\delta F_k = -B_{k1}\,\delta A_{11} F_1^0/(1 + \delta A_{11}\cdot B_{11}) \tag{13}$$

From this equation we observe that

$$\delta F_k/\delta F_1 = B_{k1}/B_{11} \tag{14}$$

In other words the ratio of the changes in any two unknowns is independent of the size of the structural modification.

If we write $R = B_{11}\cdot\delta A_{11}$ and let $k = 1$ in Eq. (13), then

$$\delta F_1/F_1^0 = -R/(1 + R) \tag{15}$$

If $\delta A_{11}$ is extremely small ($R \ll 1$) then there is a direct proportionality between the per unit change in $F_1$ and $\delta A_{11}$. Eq. (15) states that this proportionality is to be altered by the factor $1/(1 + R)$ where $R$ is the product of the change in the coefficient and the corresponding element of the inverse matrix. Hence, once $B_{11}$ is determined, the effect of a coefficient change of any size is determined by a simple curve. From Eq. (13) it is evident that the only way in which the external loads enter into the problem of determining the effect of a single structural modification is through the quantity $F_1^0$. Hence, results for one loading condition can be immediately extended to all other loading conditions if the solutions for the unmodified structure under the other loading conditions are known.

The above results can sometimes be used in experimental or analog computer investigations to reduce the number of cases to be studied. For example, the effect of variations in the rigidity of a structural element can be determined for all values of its stiffness and all loading conditions by making measurements for the standard value of the rigidity under all loading conditions and for one other value under one loading condition. The nonstandard value should preferably represent a large change. Then, from Eqs. (14) and (15),

$$B_{11} = \frac{R}{\delta A_{11}} = -\frac{\delta F_1}{F_1^0 + \delta F_1}\cdot\left(\frac{1}{\delta A_{11}}\right) \tag{16}$$

$$B_{k1} = B_{11}\cdot(\delta F_k/\delta F_1) \tag{17}$$

Eq. (13) then gives $\delta F_k$ for any values of $\delta A_{11}$ and $F_1^0$. For example, if the structural element is a member of length $l$ and area $A_0$ carrying axial forces only and $F_1$ is the force in that member, then the coefficient of $F_1^0$ is

$$A_{11}^0 = (l/EA_0) + C \tag{18}$$

where $C$ may be regarded as the flexibility of the path by which $F_1^0$ traverses the remainder of the structure. If the structural modification consists of changing the area of the member to a new value, $A_1$, then

$$\delta A_{11} = (l/E)\left[\left(\frac{1}{A_1}\right) - \left(\frac{1}{A_0}\right)\right] \tag{19}$$

From the generality of the method the other unknowns, $\delta F_k$, may be axial forces, moments, displacements, etc. The only restriction is the trivial one that the quantity $F_1$ must be statically indeterminate.

### References


[1] Michielsen, H. F., and Dijk, A., *Structural Modifications in Redundant Structures*, Journal of the Aeronautical Sciences, Vol. 20, No. 4, p. 286, April, 1953.

[2] Best, G. C., *The Stress Area Method of Designing Beams*, Journal of the Aeronautical Sciences, Vol. 12, No. 3, p. 298, July, 1945.

[3] Shea, T. E., *Transmission Networks and Wave Filters*, pp. 56–58; Van Nostrand Co., Inc., New York, 1929.

[4] Crout, P. D., *A Short Method for Evaluating Determinants and Solving Systems of Linear Equations with Real or Complex Coefficients*, AIEE Transactions, Vol. 60, pp. 1235–1240, 1941.


## Generalization of the Energy Equation Solution for Some Rotationally Symmetrical Laminar Flows


Dragutin Stojanović
*Asistent Mašinskog Fakulteta, Beograd, FNR Jugoslavija*

June 15, 1953

THE EXACT SOLUTION of the energy equation for a rotating plate[1] may be extended without any limitation of generality to all rotationally symmetrical flows for which the exact or approximate solution of the Navier-Stokes equations may be represented in the same form as that of the von Kármán solution for the flow over a rotating plate—i.e., in the form,

$$u = r\omega F(\zeta)$$
$$v = r\omega G(\zeta)$$
$$w = \sqrt{\nu\omega}\, H(\zeta)$$

For some of these flows, tables have been computed of the functions $F$, $G$, and $H$ so that they may be used to obtain function tables for the solution of the energy equation. Thus it is possible to tabulate the functions $S$ and $Q$[1] also for the following flows:

(1) Rotational flow over solid ground.[2]

(2) Flow over a rotating plate exposed to axial airflow,[3] where various heat-transfer effects of the parameter ratio of the inflow velocity and the angular velocity of the flow may be considered


REFERENCES

[1] Millsaps, K., and Pohlhausen, K., *Heat Transfer by Laminar Flow from a Rotating Plate*, Journal of the Aeronautical Sciences, Vol. 19, No. 2, p. 120, February, 1952.

[2] Bödewadt, U. T., *Die Drehströmung über festem Grunde*, ZAMM, Vol 20, p. 241, 1940.

[3] Schlichting, H., and Truckenbrodt, E., *Die Strömung an einer angeblasenen rotierenden Scheibe*, ZAMM, Vol. 32, p. 97, 1952.


## A Method for Stabilizing the Longer Period Oscillation of a Model Flying in a Closed Wind Tunnel with Freedoms in Pitch and Heave


Eugene Larrabee

*Assistant Professor of Aeronautical Engineering, Massachusetts Institute of Technology, Cambridge, Mass.*


June 16, 1953

WHEN A RIGID AIRPLANE MODEL flying in a closed wind tunnel is given freedom in pitch and heave, it possesses two oscillatory modes. The shorter period mode corresponds to the usual short-period longitudinal oscillation in free flight and is commonly heavily damped. The longer mode is caused by tunnel wall interference and is commonly divergent.[1] This unstable motion is called "galloping," and its existence seriously limits wind-tunnel testing of models provided with these degrees of freedom.

Recently, a means of stabilizing this mode has been developed by students at Massachusetts Institute of Technology working under the direction of the writer. The device in question is shown in Fig. 1. It consists of an auxiliary airfoil attached to the model mount in such a way that a nose-up attitude of the model causes a vertically downward load to be applied to the mount. Since the auxiliary airfoil is pivoted about its aerodynamic center, no moment is applied to the model by the device.

This device has been built and tested and preliminary results are presented in an M.I.T. Bachelor's Thesis by Messrs. Gionfriddo and Stewart.[2] The auxiliary airfoil used had 15 per cent of the wing area of the airplane model, had an aspect ratio of 8, and was geared to the model so that a 1-deg. nose-up change of attitude of the model caused a 1-deg. nose-down change of attitude of the auxiliary wing.

The stabilizing device operates in the following manner: Suppose that the model, initially in equilibrium with no vertical velocity, falls with a constant vertical velocity, $w$. If the model now rotates through an angle $-\theta$, equal to the ratio of the vertical velocity to the tunnel velocity, it is seen that the model without stabilizing device preserves its equilibrium angle of attack and therefore its condition of equilibrium. In the absence of tunnel wall effect, the model without stabilizing device is seen to be indifferent not only to vertical position but also to vertical velocity. In the presence of tunnel wall interference the model experiences a *nose-up* change of trim as it approaches the *floor* and a *nose-down* change of trim as it approaches the *ceiling*. This tendency, coupled with the indifference to a certain combination of vertical velocity and pitch attitude, together with inertia effects, gives rise to the unstable galloping motion. With the stabilizing device, however, the nose-down attitude associated with a vertical velocity gives rise to a nose-up attitude of the auxiliary wing, which produces a lift force opposing the vertical velocity—i.e., a damping force—and this effect in combination with the effect of tunnel wall interference causes the longer period oscillation of the model to be a damped oscillation.

MODEL WITH FREEDOMS IN PITCH AND HEAVE AS FITTED WITH AUXILIARY DAMPING WING

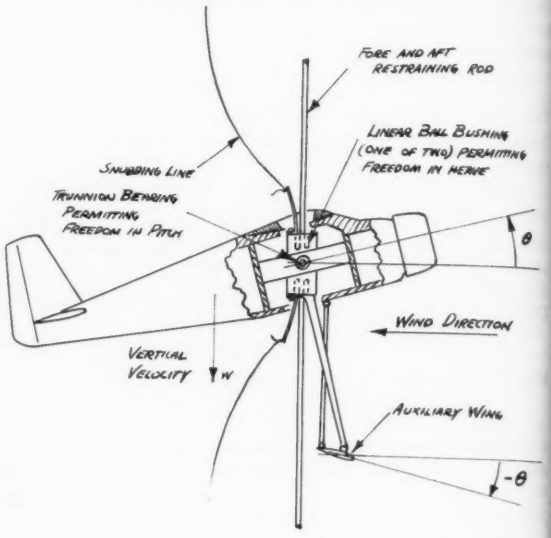


FIGURE 1

The model flown in the tests reported in references 2 and 3 was a conventional high-wing monoplane of reasonable proportions. Without the auxiliary wing its longer period oscillation had a negative damping ratio of about 10 per cent critical, and with the auxiliary wing, a positive damping ratio of about 30 per cent critical. With the auxiliary wing in use, the model would center itself in the tunnel at its trim speed, and its behavior was docile in every way.

The auxiliary wing also affects the shorter period oscillation, of course, but here its effect is essentially the same as a reduction of the lift curve slope of the model by a factor proportional to the ratio of auxiliary wing lift curve slope to model lift curve slope and the auxiliary wing gearing ratio, since the angle of attack is nearly in phase with the angle of pitch attitude in this mode. This change theoretically reduces the damping of the shorter mode from about 60 to 59 per cent critical damping for the model tested and causes a slight increase in the period of the motion.

Since the stabilizing device described appears to permit testing of models with simultaneous freedoms in heave and pitch with little distortion of the short-period longitudinal mode, work is in hand to investigate its dynamics in detail, and publication of the results of this investigation is intended at an early date.


REFERENCES

[1] Harshman, J. D., *Dynamic Wind Tunnel Tests—B-47*, Boeing Airplane Company, unpublished memorandum.

[2] Gionfriddo, M. P., and Stewart, J. H., *An Investigation of a Method for Wind Tunnel Testing of Models with Vertical and Pitch Freedoms*, Massachusetts Institute of Technology, S.B. Thesis, 1953.

[3] O'Niel, W. F., *An Investigation of Test Methods for a Wind Tunnel Model Having Vertical Freedom and Pitch Freedom*, Massachusetts Institute of Technology, S.B. Thesis, 1952.